UNIVERSITY OF BELGRADE

FACULTY OF PHYSICS

Jelena Vukalović

Elastic Electron Scattering from Anesthetic Molecules — Sevoflurane, Isoflurane, Desflurane and Halothane — in the Intermediate Energy Range

Doctoral Dissertation

Belgrade, 2026

УНИВЕРЗИТЕТ У БЕОГРАДУ

ФИЗИЧКИ ФАКУЛТЕТ

Јелена Вукаловић

Еластично расејање електрона средњих енергија на молекулима анестетика — севофлурану, изофлурану, десфлурану и халотану

Докторска дисертација

Београд, 2026

Supervision and Dissertation Committee

Supervisor: Dr Jelena Maljković, Research Assistant Professor, Institute of Physics Belgrade, University of Belgrade

Committee members:

- Dr Goran Poparić, Full Professor, Faculty of Physics, University of Belgrade
- Dr Vladimir Milosavljević, Full Professor, Faculty of Physics, University of Belgrade
- Dr Nenad Simonović, Research Professor, Institute of Physics Belgrade, University of Belgrade

Defense date:

Abstract

Title: Elastic Electron Scattering from Anesthetic Molecules — Sevoflurane, Isoflurane, Desflurane and Halothane — in the Intermediate Energy Range

Abstract:

This doctoral dissertation presents an experimental investigation of elastic electron scattering from the volatile anesthetic molecules halothane, isoflurane, sevoflurane, and desflurane in the intermediate electron energy range. Differential cross sections (DCSs) were measured using the crossed electron–molecular beam technique for a range of incident electron energies and scattering angles. Based on the obtained experimental data, integral cross sections (ICSs) and momentum transfer cross sections (MTCSs) were derived in order to provide a more complete description of the scattering processes.

The measured cross sections exhibit pronounced forward scattering characteristic of highly polarizable halogenated molecules, reflecting the important role of long-range interactions and molecular dipole effects. Systematic differences in the scattering behavior were analyzed in relation to molecular structure, degree of fluorination, and the presence of heavier halogen atoms such as chlorine and bromine.

The experimental results were compared with available theoretical calculations, primarily those based on the Independent Atom Model with screening-corrected additivity rules and interference effects (IAM-SCAR+I). Overall very good agreement between experiment and theory was observed, confirming the applicability of these theoretical approaches for complex polyatomic systems in the investigated energy range.

Particular attention was devoted to desflurane, for which experimental elastic electron scattering data were not previously available in the literature. The present work therefore provides the first set of experimental DCS, ICS, and MTCS data for this molecule.

The obtained results contribute to the broader understanding of electron–molecule interactions in biologically and environmentally relevant systems and provide valuable benchmark data for future theoretical and experimental investigations in atomic and molecular collision physics, atmospheric chemistry, and medical physics.

Key words: elastic electron scattering, differential cross sections, integral cross sections, momentum transfer cross sections, anesthetic molecules, halothane, isoflurane, sevoflurane, desflurane, electron–molecule collisions

Scientific field: Physics
Scientific subfield: Atomic and Molecular Physics

Сажетак

Наслов докторске дисертације: Еластично расејање електрона средњих енергија на молекулима анестетика — севофлурану, изофлурану, десфлурану и халотану

Сажетак:

Ова докторска дисертација представља експериментално истраживање еластичног расејања електрона на молекулима испарљивих анестетика халотана, изофлурана, севофлурана и десфлурана у области средњих енергија електрона. Диференцијални попречни пресеци (DCS) измерени су применом методе укрштених електронско-молекулских млазева за различите енергије упадних електрона и углове расејања. На основу добијених експерименталних резултата одређени су интегрални попречни пресеци (ICS) и попречни пресеци преноса импулса (MTCS), чиме је омогућен потпунији опис процеса расејања.

Измерени попречни пресеци показују изражено предње расејање карактеристично за високо поларизабилне халогенизоване молекуле, што указује на значај дугодометних интеракција и ефеката молекулског диполног момента. Систематске разлике у понашању попречних пресека анализиране су у зависности од молекулске структуре, степена флуоринације и присуства тежих халогених атома као што су хлор и бром.

Експериментални резултати упоређени су са доступним теоријским прорачунима, пре свега са резултатима добијеним применом модела независних атома са *screening-corrected additivity rules* и интерференционим ефектима (IAM-SCAR+I). Уочено је веома добро слагање између експерименталних и теоријских резултата, што потврђује применљивост ових теоријских приступа за опис сложених полиатомских система у испитиваној енергетској области.

Посебна пажња посвећена је молекулу десфлурана, за који у литератури до сада нису постојали експериментални подаци о еластичном расејању електрона. Овај рад стога представља први скуп експерименталних DCS, ICS и MTCS података за овај молекул.

Добијени резултати доприносе ширем разумевању интеракција електрона са биолошки и еколошки релевантним молекулима и представљају значајне референтне податке за будућа теоријска и експериментална истраживања у области атомске и молекулске физике, атмосферске хемије и медицинске физике.

Кључне речи: еластично расејање електрона, диференцијални попречни пресеци, интегрални попречни пресеци, попречни пресеци преноса импулса, молекули анестетика, халотан, изофлуран, севофлуран, десфлуран, електронско--молекулски судари

Научна област: Физика
Ужа научна област: Физика атома и молекула

Contents

Contents

1 Introduction **1**
- 1.1 Historical Development of Anesthetic Agents . . . 2
- 1.2 Classification of Anesthetic Agents . . . 3
- 1.3 Structure and Properties of Volatile Anesthetics . . . 3
- 1.4 Environmental Impact of Volatile Anesthetics . . . 4
  - 1.4.1 Global Warming Potential (GWP) . . . 5
  - 1.4.2 Ozone Depletion Potential (ODP) . . . 6
  - 1.4.3 Atmospheric Lifetime and Degradation Mechanisms . . . 7
  - 1.4.4 Radiative Properties and Infrared Absorption . . . 8
  - 1.4.5 Electron-Induced Processes in the Atmosphere . . . 8
- 1.5 Review of Previous Experimental and Theoretical Investigations of the Studied Anesthetic Molecules . . . 9
  - 1.5.1 Halothane . . . 10
  - 1.5.2 Isoflurane . . . 11
  - 1.5.3 Sevoflurane . . . 13
  - 1.5.4 Desflurane . . . 14
- 1.6 Scope and Objectives of the Present Work . . . 16
- 1.7 Structure of the Thesis . . . 17

2 Theoretical Background **18**
- 2.1 Types of collision . . . 18
- 2.2 Cross section . . . 21
  - 2.2.1 Differential cross-section . . . 22
- 2.3 General Characteristics of Potential Scattering . . . 23
- 2.4 The Partial Wave Method . . . 24
  - 2.4.1 Optical Theorem . . . 26
- 2.5 Molecular Scattering - The Independent Atom Model . . . 27
  - 2.5.1 The Atomic Scattering Amplitudes . . . 27
  - 2.5.2 IAM Approach with Interference . . . 28
  - 2.5.3 IAM-SCAR Method . . . 29
  - 2.5.4 Screening Corrections to the Interference Contributions . . . 32
  - 2.5.5 Polar Molecules . . . 33

3 Experimental Setup and Methodology **35**
- 3.1 Fundamentals of the Electron Spectrometers . . . 35
  - 3.1.1 Spectra . . . 36
- 3.2 General Description of the UGRA Apparatus . . . 38
  - 3.2.1 Vacuum Chamber . . . 40
  - 3.2.2 Electron Gun . . . 41

3.2.3 Analyzer System . . . 42
3.2.4 Electron Detection System . . . 44
3.3 Types of Measurements and Methods . . . 45
3.3.1 Measurement of Relative Differential Cross Sections for Elastic Electron Scattering . . . 46
3.3.2 Measurement of Absolute Differential Cross Sections for Elastic Electron Scattering . . . 48
3.3.3 Integral and Momentum Transfer Cross Sections . . . 52
3.3.4 Evaluation of Measurement Uncertainties . . . 52

4 Results and Discussion **54**
4.1 Halothane . . . 54
4.1.1 Differential Cross Sections . . . 56
4.1.2 Integral and Momentum Transfer Cross Sections . . . 57
4.2 Isoflurane . . . 60
4.2.1 Differential Cross Sections . . . 61
4.2.2 Integral and Momentum Transfer Cross Sections . . . 63
4.3 Sevoflurane . . . 66
4.3.1 Differential Cross Sections . . . 67
4.3.2 Integral and Momentum Transfer Cross Sections . . . 69
4.4 Desflurane . . . 73
4.4.1 Differential Cross Sections . . . 74
4.4.2 Integral and Momentum Transfer Cross Sections . . . 76

5 Final Remarks and Future Research Directions **79**
5.1 Conclusions . . . 79
5.2 Future Research Directions . . . 80

Bibliography **82**

Chapter 1

Introduction

The interaction of electrons with complex molecular systems represents one of the central topics of contemporary atomic and molecular physics. Electron–molecule collisions govern a wide range of microscopic processes occurring in plasmas, planetary and terrestrial atmospheres, radiation chemistry, biological media, and technologically important environments. In particular, elastic electron scattering from polyatomic molecules provides fundamental information on the spatial distribution of molecular charge, polarization effects, and interaction potentials, while also serving as an essential input for modelling electron transport and energy deposition processes.

Among complex molecular targets, volatile halogenated anesthetics occupy a particularly important position due to their simultaneous relevance in medicine, environmental science, and molecular collision physics. Molecules such as halothane, isoflurane, sevoflurane, and desflurane are widely used in modern inhalation anesthesia because of their favorable pharmacological properties, chemical stability, and controllable anesthetic action. At the same time, their high degree of halogenation, strong molecular polarity, and large number of electrons make them challenging and scientifically attractive systems for experimental and theoretical investigations of electron scattering phenomena.

In recent decades, increasing attention has also been devoted to the environmental impact of volatile anesthetics. Owing to their relatively long atmospheric lifetimes and strong infrared absorption characteristics, several of these compounds contribute to greenhouse warming and atmospheric chemical processes. In addition, electron-induced fragmentation and dissociation mechanisms may play a role in their atmospheric degradation pathways. Consequently, detailed investigations of electron interactions with anesthetic molecules are important not only from the standpoint of fundamental collision physics, but also for understanding broader environmental and atmospheric effects associated with these compounds.

Despite numerous studies devoted to their spectroscopy, electronic structure, and photochemical behavior, experimental data for electron scattering cross sections of volatile anesthetics remain relatively limited, particularly for intermediate electron energies and larger polyatomic systems. Reliable differential, integral, and momentum-transfer cross sections are nevertheless essential for testing theoretical models and for improving the understanding of electron-driven processes in biologically and environmentally relevant media.

The present dissertation is devoted to the experimental investigation of elastic electron scattering from several representative volatile anesthetic molecules in the gas phase. Special emphasis is placed on the determination and analysis of differential cross sections, their comparison with theoretical predictions, and the identification of trends related to molecular structure, halogen substitution, and degree of fluorination. Through this study, the thesis aims to contribute to the broader understanding of electron–molecule interactions in complex halogenated systems and to provide new experimental data of relevance for molecular physics, atmospheric

chemistry, and related interdisciplinary fields.

1.1 Historical Development of Anesthetic Agents

The history of surgical anesthesia is a narrative of continuous evolution, driven by the search for an "ideal" agent—one that provides rapid induction and emergence, predictable potency, and a high safety profile with minimal side effects [1]. The modern era began in the mid-19th century, although the analgesic properties of certain gases were known earlier. A transformative shift occurred in the 1950s with the introduction of halogenated hydrocarbons, which eliminated the hazard of explosions associated with diethyl ether and cyclopropane [2, 3].

- **Nitrous Oxide (N_2O):** Often referred to as "laughing gas," nitrous oxide is the oldest inhalation agent still in clinical use. Its anesthetic properties were first synthesized by Joseph Priestley in 1772 and later demonstrated for dental extraction by Horace Wells in 1844 [3]. While it lacks sufficient potency to be used as a sole anesthetic agent (due to its high MAC value), it remains a staple in modern practice as an adjunct to volatile anesthetics [1].

- **Halothane ($C_2HBrClF_3$):** Introduced clinically in 1956, halothane was the first successful fluorinated hydrocarbon. It revolutionized anesthesia by being non-flammable and relatively easy to administer [4]. However, its significant metabolism (20%) led to concerns over hepatotoxicity, which eventually paved the way for the development of more stable fluorinated ethers [1].

- **Enflurane ($C_3H_2ClF_5O$):** Developed by Ross Terrell in 1963 and introduced into clinical practice in the early 1970s, enflurane represented an important step toward the use of halogenated methyl ethyl ethers. Although it offered better stability than halothane, it was later largely replaced by its isomer, isoflurane, due to enflurane's potential to induce seizure-like EEG activity at high concentrations [3].

- **Isoflurane ($C_3H_2ClF_5O$):** An isomer of enflurane, isoflurane was synthesized in 1965. Its clinical introduction was delayed until the early 1980s due to early concerns regarding potential toxicity [3]. Isoflurane became a global mainstay because of its remarkable metabolic stability (only 0.2 % metabolism) and reduced risk of cardiac arrhythmias compared to halothane [1].

- **Sevoflurane ($C_4H_3F_7O$):** Synthesized by Bernard Regan in 1968, sevoflurane underwent a prolonged development period due to its degradation in carbon dioxide absorbents [5]. It was first introduced for clinical use in Japan in 1990 before reaching the U.S. and Europe. Due to its extremely low blood-gas solubility and non-pungent odor, it has become the gold standard for pediatric inhalation induction [3].

- **Desflurane ($C_3H_2F_6O$):** Introduced in the 1990s, desflurane is characterized by its extremely low solubility, allowing for the most rapid recovery among halogenated agents. Its unique physical properties, such as a high vapor pressure, require the use of specialized heated vaporizers [1].

The transition from early gases like N_2O and flammable ethers to modern fluorinated agents reflects a sophisticated refinement in molecular engineering. In the context of this dissertation, understanding the historical shift toward these specific halogenated molecules is essential, as their unique electron-molecule interaction cross-sections are fundamental to both their biological function and their role as atmospheric greenhouse gases [1, 6].

1.2 Classification of Anesthetic Agents

Anesthetic agents are broadly classified based on their route of administration and their chemical structure. This classification is significant for the present study as it narrows the focus down to volatile halogenated agents, whose physical properties are governed by their specific molecular architectures [1, 7].

Classification by Route of Administration

Anesthetics are primarily divided into two main groups:

1. **Intravenous Anesthetics:** Compounds such as propofol, etomidate, and barbiturates, which are administered directly into the bloodstream. These are typically larger, more complex organic molecules.
2. **Inhalation Anesthetics:** Gases or volatile liquids that are delivered through the respiratory system. This group is further divided into:
    - **Non-volatile gases:** Such as Nitrous oxide (N_2O) and Xenon (Xe).
    - **Volatile liquids:** This subgroup includes the halogenated hydrocarbons (e.g., Halothane) and halogenated ethers (e.g., Isoflurane, Sevoflurane, Desflurane), which are the primary focus of this research.

Chemical Classification of Volatile Agents

From a molecular physics perspective, the chemical classification is based on the carbon skeleton and the type of halogen substitution. The molecules investigated in this work belong to two structural classes:

- **Halogenated Alkanes:** Represented by **Halothane**, which is a substituted ethane derivative containing fluorine, chlorine, and bromine atoms.
- **Halogenated Ethers:** Represented by **Isoflurane**, **Desflurane**, and **Sevoflurane**. These molecules contain an ether linkage (C-O-C) and are heavily fluorinated.

This distinction is important for electron scattering studies, as the presence of different halogen atoms and the ether functional group significantly influences the molecular electrostatic potential and, consequently, the differential and total scattering cross-sections [8].

1.3 Structure and Properties of Volatile Anesthetics

The volatile anesthetic agents investigated in this work—Halothane, Isoflurane, Sevoflurane, and Desflurane—are small, halogenated organic molecules. Their chemical behavior and physical stability are primarily determined by the presence of halogen atoms (F, Cl, and Br) which have replaced hydrogen atoms on an alkane or ether backbone. Halothane ($C_2HBrClF_3$) stands out as a halogenated ethane derivative and is the only agent in this group containing a bromine atom. In contrast, Isoflurane, Desflurane, and Sevoflurane are halogenated ethers characterized by the presence of a $C-O-C$ linkage, which contributes to their high chemical stability and reduced metabolic rate compared to older agents [1, 3].

The most prominent feature of these molecules is their high degree of fluorination. Fluorine atoms are exceptionally electronegative, which leads to a strong induction effect and a non-uniform distribution of electronic charge within the molecular frame. This asymmetric charge

distribution results in permanent molecular dipole moments and influences the overall molecular polarizability. While Halothane and Isoflurane contain heavier halogens like bromine or chlorine, which increase the "electron cloud" size and polarizability, Desflurane and Sevoflurane are more heavily fluorinated, leading to different electronic environments [1, 6].

From an experimental standpoint, the volatility of these agents is their most defining characteristic. They are liquids at room temperature but possess relatively low boiling points and high vapor pressures, which allows them to be easily transitioned into the gas phase for study. Their stability in the gas phase and resistance to degradation are essential for ensuring consistent measurements. The transition from the alkane-based Halothane to the modern fluorinated ethers reflects an evolutionary path toward molecules that are not only safer for clinical use but also exhibit distinct physical signatures due to their specific atomic arrangements [3, 6].

1.4 Environmental Impact of Volatile Anesthetics

In addition to their medical importance, volatile halogenated anesthetics have attracted considerable attention due to their environmental impact. After administration, only a relatively small fraction of the inhaled anesthetic is metabolized in the human body, while the remaining amount is exhaled unchanged into the atmosphere. The extent of metabolism differs among anesthetics: approximately 20% of halothane is metabolized, compared to about 0.2% for isoflurane, 2–5% for sevoflurane, and only around 0.02% for desflurane [2]. Consequently, a significant portion of these compounds eventually reaches the atmosphere, where they can participate in various photochemical and electron-induced processes.

The environmental relevance of inhalation anesthetics arises primarily from their long atmospheric lifetimes, strong infrared absorption characteristics, and, in some cases, the presence of chlorine or bromine atoms that contribute to ozone depletion mechanisms. Due to their high chemical stability, many fluorinated anesthetics are resistant to rapid degradation in the lower atmosphere, allowing them to persist long enough to reach higher atmospheric layers. Their accumulation has therefore raised concerns regarding their contribution to anthropogenic climate change and atmospheric chemistry.

Among currently used anesthetics, desflurane is considered to have the largest environmental impact because of its exceptionally high global warming potential (GWP) and long atmospheric lifetime. In contrast, sevoflurane undergoes somewhat larger metabolic degradation and exhibits a substantially lower atmospheric persistence. Isoflurane occupies an intermediate position, while halothane, although now less commonly used clinically, remains important due to the presence of both chlorine and bromine atoms, which are directly linked to ozone depletion chemistry.

The atmospheric behavior of volatile anesthetics has been investigated in several experimental and theoretical studies. Ryan and Nielsen [9] analyzed the environmental consequences of modern inhalation anesthetics and emphasized that desflurane possesses a significantly higher climate impact compared to sevoflurane and isoflurane due to its combination of high radiative efficiency and long atmospheric residence time. Earlier studies by Langbein et al. [10] also demonstrated that inhalation anesthetics act as greenhouse gases with non-negligible radiative forcing effects, particularly in the case of highly fluorinated compounds.

Besides their climatic effects, halogenated anesthetics are also relevant from the perspective of atmospheric degradation mechanisms. In the atmosphere, these molecules may undergo reactions initiated by UV radiation, hydroxyl radicals, low-energy electrons, and other reactive species. Such processes can lead to fragmentation, radical formation, and release of halogen atoms, which may subsequently participate in catalytic ozone destruction cycles. Therefore, understanding the interaction of electrons with anesthetic molecules, including elastic scatter-

ing and electron-induced excitation or dissociation processes, is important not only from the standpoint of fundamental molecular physics but also for improving the understanding of their atmospheric fate.

The following sections summarize the most important environmental parameters of volatile anesthetics, including their global warming potential, ozone depletion potential, atmospheric stability, radiative properties, and electron-induced atmospheric processes.

1.4.1 Global Warming Potential (GWP)

One of the principal parameters used to quantify the climatic impact of greenhouse gases is the global warming potential (GWP). This quantity expresses the cumulative warming effect produced by a given gas relative to carbon dioxide and represents one of the standard measures employed in atmospheric chemistry and climate science [9, 11]. The GWP enables direct comparison between different greenhouse gases by taking into account both their infrared absorption properties and their persistence in the atmosphere. In environmental studies, GWP values are commonly evaluated over time horizons of 20, 100, or 500 years, with the 100-year value, denoted as GWP_{100}, being the most widely adopted reference [9, 11].

The GWP of a gas is formally defined as the ratio between the time-integrated radiative forcing caused by the release of a unit mass of the investigated gas and that produced by the same mass of CO_2 over a selected time interval H [9, 11]:

$$\mathrm{GWP}(H) = \frac{\displaystyle\int_0^H RF_x(t)\,dt}{\displaystyle\int_0^H RF_{\mathrm{CO_2}}(t)\,dt},$$

where $RF_x(t)$ and $RF_{\mathrm{CO_2}}(t)$ represent the radiative forcing generated by the investigated gas and carbon dioxide, respectively.

Radiative forcing represents the perturbation of the Earth's radiative balance caused by the presence of greenhouse gases in the atmosphere [11]. Molecules that efficiently absorb infrared radiation within the atmospheric transparency window contribute more strongly to radiative forcing and therefore exhibit larger GWP values. Volatile anesthetics belong to this category because they contain multiple halogen atoms, particularly fluorine, which give rise to intense infrared absorption bands associated mainly with vibrational modes involving C–F bonds [9,11]. Consequently, these compounds can efficiently absorb terrestrial infrared radiation emitted by the Earth's surface.

Although the atmospheric concentrations of anesthetic gases are significantly lower than those of major greenhouse gases such as CO_2, CH_4, or N_2O, their environmental relevance should not be neglected [9, 10]. Due to their relatively large radiative efficiencies and chemical stability, volatile anesthetics may contribute measurably to anthropogenic greenhouse warming. Their environmental significance is additionally enhanced by the fact that only a small fraction of the administered anesthetic is metabolized in the human body, while the majority is exhaled unchanged and eventually released into the atmosphere through hospital ventilation systems [2, 9].

The environmental impact of inhalation anesthetics has therefore become an increasingly important topic in recent years, particularly in the context of sustainable healthcare and reduction of medical greenhouse gas emissions [9]. Several studies have demonstrated that the choice of anesthetic agent can significantly influence the total environmental footprint of anesthetic procedures. Ryan and Nielsen [9] showed that desflurane exhibits substantially larger greenhouse effects compared to sevoflurane and isoflurane under comparable clinical conditions. Earlier investigations by Langbein et al. [10] similarly identified volatile anesthetics as

greenhouse gases with measurable radiative forcing contributions.

Among commonly used anesthetic agents, desflurane possesses by far the highest GWP values and is therefore considered the most environmentally problematic modern inhalation anesthetic. Reported GWP_{100} values are approximately 2540 for desflurane, around 510 for isoflurane, and about 130 for sevoflurane [9, 10]. Halothane, although less frequently used in modern clinical practice, also exhibits a relatively large global warming potential, estimated to be close to 1900 [10]. These differences arise primarily from variations in molecular structure, infrared absorption efficiency, and atmospheric degradation pathways.

Highly fluorinated molecules generally exhibit enhanced infrared absorption because of the strong polarity of C–F bonds and the large number of vibrational modes active in the infrared spectral region. Sulbaek Andersen et al. [11] investigated the atmospheric chemistry and radiative properties of several halogenated anesthetics and demonstrated that their infrared absorption cross sections contribute significantly to their greenhouse characteristics. Their study emphasized that even compounds present at relatively low atmospheric abundances may possess notable climatic effects if their radiative efficiencies are sufficiently large.

In addition to molecular composition, clinical practice also plays an important role in determining the environmental burden associated with anesthetic gases. High fresh gas flow rates and prolonged administration times can substantially increase anesthetic consumption and therefore atmospheric emissions [9]. As a result, strategies aimed at reducing the ecological footprint of anesthesia have attracted growing attention. These approaches include minimizing fresh gas flows, optimizing anesthetic delivery systems, implementing gas capture and recycling technologies, and favoring anesthetics with lower GWP values whenever clinically appropriate.

Because the environmental behavior of anesthetic gases depends strongly on their molecular properties and interaction mechanisms, detailed studies of their physical and chemical characteristics are of considerable importance. Investigations of electron scattering, molecular excitation, fragmentation, and radiative interactions therefore contribute not only to the understanding of fundamental molecular collision processes but also to the broader understanding of the atmospheric fate and environmental impact of volatile anesthetics.

1.4.2 Ozone Depletion Potential (ODP)

In addition to their contribution to greenhouse warming, halogenated volatile anesthetics may also affect stratospheric ozone chemistry due to the presence of chlorine and, in some cases, bromine atoms. The ozone depletion potential (ODP) is a relative metric used to quantify the ability of a compound to destroy stratospheric ozone compared to a reference substance, typically CFC-11.

Formally, the ODP of a compound x is defined as:

$$\mathrm{ODP}_x = \frac{\displaystyle\int_0^\infty \Delta O_3(x,t)\,dt}{\displaystyle\int_0^\infty \Delta O_3(\mathrm{CCl_3F},t)\,dt},$$

where $\Delta O_3(x,t)$ represents the ozone column perturbation induced by emission of species x [10].

Among volatile anesthetics, halothane exhibits the highest ozone depletion potential due to the presence of both chlorine and bromine atoms, which enables highly efficient catalytic ozone destruction cycles. Reported values indicate an ODP of approximately 1.56 relative to CFC-11 [10], making halothane the most ozone-relevant anesthetic in this class.

Isoflurane and sevoflurane contain chlorine atoms but no bromine. Their ozone depletion potentials are therefore significantly lower. Reported values are approximately ~ 0.02 for

isoflurane and ~ 0.01 for sevoflurane, indicating only a minor contribution to stratospheric ozone destruction compared to halogenated industrial compounds [10].

Desflurane contains only fluorine atoms and does not release reactive chlorine or bromine species in the atmosphere. As a result, its ozone depletion potential is effectively negligible (ODP ≈ 0), and its environmental impact is instead dominated by radiative forcing and its high global warming potential [9, 10].

Overall, the differences in ODP among volatile anesthetics are primarily governed by molecular composition. Bromine-containing compounds exhibit the highest ozone depletion efficiency, chlorine-containing compounds show weak but non-zero effects, while fully fluorinated anesthetics do not contribute to catalytic ozone depletion chemistry.

1.4.3 Atmospheric Lifetime and Degradation Mechanisms

The atmospheric lifetime of volatile halogenated anesthetics is a key parameter governing their environmental impact, as it determines the time scale over which these compounds can participate in radiative forcing and stratospheric chemistry. Atmospheric removal processes are primarily controlled by chemical degradation in the troposphere, rather than physical deposition, due to the relatively inert nature of these molecules under ambient conditions.

The dominant sink for most volatile anesthetics is reaction with hydroxyl radicals (OH), which represent the primary atmospheric oxidizing species. OH-initiated abstraction processes lead to stepwise degradation of the parent molecule and formation of reactive intermediates. Additional contributions may arise from photolysis and electron-induced dissociation processes in the upper atmosphere, where higher-energy radiation and secondary electrons are present [8, 11].

Among the anesthetics considered, halothane exhibits relatively fast atmospheric removal compared to fully fluorinated compounds due to the presence of weaker C–Cl and C–Br bonds. Reported atmospheric (tropospheric) lifetimes vary between approximately 2 years (OH reactivity-based estimate) and about 7 years (combined OH and spectroscopic modelling), reflecting methodological differences in kinetic modelling approaches [10,12]. This relatively short persistence, combined with the presence of bromine, makes halothane particularly relevant for stratospheric ozone chemistry.

Isoflurane shows an atmospheric lifetime of approximately 3–5 years, depending on the adopted OH concentration and kinetic model assumptions [10]. Sevoflurane is somewhat more reactive, with a shorter atmospheric lifetime of approximately 1–2 years, primarily due to its higher susceptibility to OH-initiated degradation pathways [10, 13]. These differences reflect variations in molecular structure and the availability of reactive sites for radical attack.

Desflurane is significantly more stable in the atmosphere than the other anesthetics considered. Reported atmospheric lifetimes range from approximately 9 to 21 years, making it one of the most persistent modern volatile anesthetic agents [9, 13]. This exceptional stability is attributed to the strong C–F bonds and the absence of reactive halogen substitution that would otherwise facilitate faster degradation.

The primary degradation pathway for all compounds remains OH radical chemistry, which initiates hydrogen abstraction or addition processes depending on molecular structure. In halogenated systems, this leads to fragmentation and eventual formation of smaller fluorinated or chlorinated species. In addition, photochemical processes in the upper atmosphere and low-energy electron interactions may contribute to molecular dissociation, particularly through dissociative electron attachment (DEA) channels [8, 14].

Electron-molecule scattering processes are increasingly recognized as relevant in atmospheric chemistry of halogenated anesthetics. Low-energy electrons can induce transient negative ion formation, resulting in bond cleavage and fragmentation. These mechanisms are particularly

efficient for molecules containing C–Cl and C–Br bonds, while fully fluorinated compounds are considerably more resistant to electron-induced dissociation due to the high bond strength of C–F bonds [8].

Overall, the atmospheric lifetime of volatile anesthetics spans more than an order of magnitude across different compounds, ranging from approximately 1–2 years for sevoflurane, 3–5 years for isoflurane, 2–7 years for halothane, and up to 9–21 years for desflurane. These differences arise from variations in molecular structure, bond strengths, and reactivity toward atmospheric oxidants. The increasing fluorination of modern anesthetics enhances atmospheric stability, while simultaneously reducing chemical reactivity, thereby extending their environmental persistence.

1.4.4 Radiative Properties and Infrared Absorption

Volatile halogenated anesthetics exhibit significant radiative efficiency due to their strong absorption of infrared (IR) radiation in the atmospheric transparency window. This property is a direct consequence of their molecular structure, which is dominated by C–F, C–Cl, and in some cases C–Br bonds, leading to multiple vibrational modes active in the mid-infrared region.

The radiative efficiency of these compounds is primarily determined by their ability to absorb outgoing longwave terrestrial radiation, thereby contributing to an enhanced greenhouse effect. Highly fluorinated molecules, in particular, exhibit strong and broad absorption bands associated with C–F stretching and bending vibrations. These absorption features overlap with the so-called "atmospheric window", where Earth's outgoing radiation is only weakly absorbed by major atmospheric constituents such as H_2O, CO_2, and O_3.

Among the anesthetics considered, desflurane shows the highest radiative efficiency due to its extensive fluorination and complex vibrational structure, which results in strong absorption across multiple IR bands. Isoflurane and sevoflurane also exhibit significant infrared activity, although their spectral features are somewhat reduced due to differences in molecular symmetry and bond distribution. Halothane, containing both chlorine and bromine atoms, shows distinct absorption features in the mid-infrared region, contributing to its radiative forcing despite lower fluorination compared to modern agents.

Recent atmospheric studies have demonstrated that even trace concentrations of these compounds can produce measurable radiative forcing due to their high IR absorption cross sections [11]. Sulbaek Andersen et al. further showed that radiative efficiency, combined with atmospheric lifetime, is a key determinant of the overall climate impact of halogenated anesthetics [11].

Overall, the radiative properties of volatile anesthetics are governed by molecular vibrational structure, with fluorination playing a central role in enhancing infrared absorption strength and spectral overlap with the atmospheric window [8].

1.4.5 Electron-Induced Processes in the Atmosphere

In addition to photochemical and radical-driven degradation pathways, electron-induced processes represent an important mechanism in the atmospheric chemistry of halogenated volatile anesthetics. These processes are driven by low-energy electrons, which are abundant in the upper atmosphere due to cosmic ray interactions, photoionization events, and secondary electron cascades.

A key mechanism in this context is dissociative electron attachment (DEA), in which a low-energy electron is temporarily captured by a molecule, forming a transient negative ion state that subsequently dissociates into fragment species. This process can lead to selective

cleavage of weak chemical bonds, particularly C–Cl and C–Br bonds, resulting in the formation of reactive halogen radicals.

The importance of low-energy electron interactions in atmospheric and molecular processes has been extensively discussed by Campbell and Brunger [15], who emphasized the role of transient negative ion formation and electron-driven fragmentation in complex molecular systems. In a more recent atmospheric chemistry study, Campbell and Brunger [16] further highlighted the relevance of electron-induced processes in atmospheric environments, particularly under conditions where secondary electrons are generated through ionization and radiative processes.

Experimental and theoretical studies have shown that halogenated anesthetics exhibit measurable cross sections for electron-molecule scattering and DEA processes, indicating that these compounds can undergo fragmentation under low-energy electron impact conditions [8]. The efficiency of these mechanisms depends strongly on molecular composition, with bromine- and chlorine-containing molecules generally being more susceptible to electron-induced bond cleavage than fully fluorinated compounds.

Halothane is particularly sensitive to electron-induced dissociation due to the presence of both chlorine and bromine atoms, which provide energetically favorable dissociation pathways following electron attachment. Isoflurane and sevoflurane also exhibit electron-induced fragmentation channels associated primarily with C–Cl bond cleavage. In contrast, desflurane, which contains only fluorine substituents, is considerably more resistant to DEA processes due to the high bond strength of the C–F bond and the absence of efficient low-energy dissociative channels.

Electron-driven fragmentation processes may therefore complement conventional atmospheric degradation pathways such as OH-initiated oxidation and photolysis. In particular, low-energy electron attachment can initiate rapid molecular dissociation and formation of reactive radical species, thereby linking microscopic electron scattering phenomena with macroscopic atmospheric chemistry effects [8, 15, 16].

Overall, electron-induced processes provide an important additional perspective for understanding the atmospheric behavior of volatile anesthetics. Their investigation is especially relevant for halogenated systems, where transient negative ion formation and subsequent fragmentation may influence both molecular stability and environmental degradation pathways.

1.5 Review of Previous Experimental and Theoretical Investigations of the Studied Anesthetic Molecules

Volatile halogenated anesthetics have been widely studied due to their relevance in both medical applications and atmospheric chemistry. From a molecular physics perspective, these systems are of interest because of their structural complexity, strong polarization effects, and rich electronic and vibrational structure.

A variety of experimental and theoretical techniques have been used to investigate their properties, including spectroscopic methods, quantum chemical calculations, gas electron diffraction, and electron-scattering experiments. These studies provide information on molecular structure, electronic states, and electron-induced processes such as scattering and fragmentation.

In the following subsections, previous investigations of halothane, isoflurane, sevoflurane, and desflurane are summarized, with emphasis on results relevant to molecular structure, spectroscopy, and collision dynamics.

1.5.1 Halothane

Halothane has been extensively investigated due to its historical importance as one of the first widely used halogenated inhalation anesthetics and its unique chemical composition containing fluorine, chlorine, and bromine atoms. Its molecular structure makes it particularly relevant not only in medical applications but also in studies of atmospheric chemistry, photodissociation dynamics, and electron-driven processes. A summary of the most relevant previous experimental and theoretical studies is provided in Table 1.1.

A significant contribution to the understanding of the electronic structure and excited-state properties of halothane was provided by Ferreira da Silva et al. [17], who combined ab initio calculations of Rydberg and valence transitions with high-resolution vacuum ultraviolet (VUV) photoabsorption measurements in the wavelength range from 115 nm to 300 nm. Their study demonstrated that halothane exhibits rich electronic excitation features in the VUV region. Importantly, they also estimated its photolysis lifetime and concluded that, in the stratosphere, ultraviolet photoabsorption represents the dominant mechanism for the release of chlorine and bromine atoms, which play a critical role in catalytic ozone depletion processes.

Electron-induced fragmentation processes in halothane have also been investigated in detail. Lozano et al. [18] studied negative ion formation through electron transfer from neutral potassium atoms over a wide collision energy range (8–1000 eV) using a crossed-beam experimental setup. Their results showed that the dominant anionic fragments are Br^-, Cl^-, and F^-, with bromine anions representing the most efficient dissociation channel. These findings were supported by electronic structure calculations, confirming the fragmentation pathways and energetics of the system.

Complementary studies by Marotta et al. [19] further examined the ion chemistry of halothane in air plasma at atmospheric pressure. Their results confirmed that Br^- is the predominant negative ion formed, followed by Cl^-, emphasizing the importance of halogen-containing fragments in plasma-driven decomposition processes. These investigations collectively highlight the susceptibility of halothane to electron-induced and ion-driven dissociation mechanisms.

From a structural perspective, Scharf et al. [20] provided a detailed determination of the gas-phase molecular geometry of halothane, contributing to a more precise understanding of its conformational properties. Their study also included theoretical modelling of intermolecular interactions using density functional theory and molecular dynamics simulations, providing effective pair potentials that reproduce available thermodynamic properties and gas-phase behavior of halothane. This work was later complemented by Tang et al. [21], who analyzed both the charge distribution and molecular structure of halothane and sevoflurane, providing insight into the relationship between electronic structure and molecular polarity in halogenated anesthetics. Their results further clarified the electronic charge redistribution within the molecule, offering improved insight into the dipole moment distribution and its relevance for intermolecular interactions and collision processes.

A combined experimental and theoretical study of the vibrational and structural properties of halothane was reported by Czarnik-Matusewicz et al. [22]. Using ab initio calculations together with IR and Raman spectroscopy, the authors analyzed the conformational stability and vibrational modes of the molecule. Their results confirmed the preference for the staggered conformer and showed good agreement between calculated and measured vibrational frequencies after appropriate scaling. The study provides a reliable description of the equilibrium geometry and internal dynamics of halothane, which are important for understanding its dipole distribution and interaction with electrons in scattering processes.

Further insight into the photodissociation dynamics of halothane has been obtained through time-resolved and wavelength-specific studies. Yokoyama et al. [23] investigated photodissociation at 157 nm, while Saha et al. [24] extended these studies to near 234 nm excitation. These works demonstrated that halothane undergoes efficient bond cleavage upon UV excitation, with

Table 1.1: Summary of previous experimental and theoretical studies on halothane relevant to its molecular structure, spectroscopy, electron-induced processes, and scattering dynamics.

Authors	**Type of study**	**Method / Conditions**	**Main results**
Ferreira da Silva et al. [17]	Electronic excitation + photophysics	Ab initio calculations; VUV photoabsorption (115–300 nm)	Rydberg and valence states; UV-induced Cl and Br release; ozone depletion
Lozano et al. [18]	Electron-induced fragmentation (DEA)	Crossed electron–molecular beam (8–1000 eV)	Formation of Br^-, Cl^-, F^-; Br^- dominant channel
Marotta et al. [19]	Plasma ion chemistry	Atmospheric pressure plasma experiments	Formation of Br^- and Cl^- negative ions in plasma conditions
Scharf et al. [20]	Molecular structure + intermolecular interactions	DFT + molecular dynamics (gas/liquid phase)	Equilibrium structure; effective pair potentials; thermodynamic consistency
Tang et al. [21]	Electronic structure	Quantum chemical calculations	Charge distribution and dipole moment relevant for intermolecular interactions
Czarnik-Matusewicz et al. [22]	Vibrational structure	Ab initio (MP2, DFT) + IR/Raman spectroscopy	Staggered conformer stability; vibrational mode assignments
Yokoyama et al. [23]	Photodissociation dynamics	UV photolysis at 157 nm	Efficient bond cleavage and fragmentation pathways
Saha et al. [24]	Photodissociation dynamics	UV excitation ($\sim$234 nm)	Energy-dependent dissociation mechanisms
Maioli et al. [25]	Elastic electron scattering	SMCPP + IAM-SCAR+I + experiment (10–50 eV)	DCS, ICS, MTCS; reasonable agreement between theory and experiment

dissociation pathways strongly dependent on photon energy and molecular electronic structure.

Among the most relevant studies for the present work is the combined theoretical and experimental investigation of elastic electron scattering from halothane reported by Maioli et al. [25]. In this study, differential, integral, and momentum transfer cross sections (DCSs, ICSs, and MTCSs) were calculated using the Schwinger multichannel method with pseudopotentials, as well as the independent atom model incorporating screening-corrected additivity rules and interference effects (IAM-SCAR+I). Experimental DCSs were measured for incident electron energies of 10, 20, 30, and 50 eV over a scattering angle range from 7° to 100°. The comparison between theory and experiment showed overall reasonable agreement, validating the applicability of the employed theoretical frameworks for complex halogenated molecules.

Collectively, these studies demonstrate that halothane is a prototypical system for understanding the interplay between molecular structure, electron-driven processes, and atmospheric relevance in halogenated anesthetic compounds.

1.5.2 Isoflurane

Isoflurane has been extensively studied due to its widespread clinical use as a modern halogenated inhalation anesthetic and its structurally related nature to other fluorinated ethers such as sevoflurane and desflurane. Its molecular complexity and conformational flexibility make it an important system for investigating structure–property relationships, electron-induced processes, and photon–molecule interactions. A summary of the most relevant previous experimental and theoretical studies is provided in Table 1.2.

A detailed investigation of the geometric structure and conformational properties of isoflurane, together with desflurane, was reported by utilizing a combination of Gas Electron Diffraction (GED) and quantum chemical calculations [26]. Both molecules were found to exist as

mixtures of two conformers in the gas phase. The dominant conformer of isoflurane is characterized by a nearly trans configuration of the C–C–O–C skeleton and a trans orientation of the CHF2 group, while the minor conformer adopts a gauche orientation. These results highlight the importance of conformational flexibility in determining the molecular geometry and its associated electronic properties.

Electron-induced fragmentation processes in isoflurane have been investigated through dissociative electron attachment (DEA) experiments performed by Matias et al. [27]. Using a crossed electron–molecular beam setup combined with a two-sector field mass spectrometer, anion efficiency curves for the resulting negative fragments were measured over an electron energy range of approximately 0–17 eV. The dominant anionic channels were observed in the 2–3 eV and 9 eV regions, while the Cl^- fragment exhibited a pronounced resonance at around 0.6 eV. Complementary quantum chemical calculations were used to determine thermochemical thresholds for anion formation, providing important insight into the underlying dissociation mechanisms.

Negative ion formation in isoflurane has also been investigated using ion mobility spectrometry–mass spectrometry (IMS–MS) by González-Méndez et al. [28]. The study showed that previously reported Cl^- signals are not due to dissociative electron attachment, but rather to chlorine-containing impurities in earlier experiments. It was further demonstrated that isoflurane exhibits high vertical attachment energies, which suppress efficient DEA processes, and that observed weak ion–molecule complexes are predominantly clustering products rather than direct fragmentation channels.

Further insight into the electronic structure of isoflurane was provided by Lange et al. [29], who investigated the lowest-lying electronic excited states of isoflurane and sevoflurane in the photon energy range of 5.0–10.8 eV. Synchrotron-based photoabsorption spectroscopy was combined with quantum chemical calculations to assign low-lying singlet valence and Rydberg states, as well as to identify contributions from triplet states. These results provide a detailed description of the excitation landscape relevant for photon–molecule interactions.

A recent study by Kopyra et al. [30] further investigated electron-impact induced fragmentation of isoflurane, providing detailed insight into its dissociation dynamics under electron collision conditions. The work combines experimental measurements and theoretical modelling to analyze the formation of fragment ions as a function of incident electron energy. The results demonstrate that electron-induced processes play a significant role in the fragmentation pathways of isoflurane, complementing previous DEA studies and further highlighting its susceptibility to electron-driven decomposition mechanisms.

The most comprehensive study relevant to electron scattering from isoflurane is presented in the PhD thesis of E. Lange [31]. This work includes both theoretical and experimental investigations of elastic electron scattering. Theoretical differential and integral cross sections (DCSs and ICSs) were obtained using the Schwinger multichannel method with pseudopotentials, as well as the independent atom model with screening-corrected additivity rules and interference effects (IAM-SCAR+I). Experimental DCSs were measured in the 10–50 eV energy range and over a scattering angle range of 8° to 70°, using a high-resolution electron energy loss spectrometer. The absolute normalization of the experimental data was achieved by scaling to the IAM-SCAR+I results at a scattering angle of 30°, and overall good agreement between theory and experiment was observed.

Together, these studies highlight the relationship between molecular structure, electronic states, and electron-driven processes in isoflurane.

Table 1.2: Summary of previous experimental and theoretical studies on isoflurane relevant to its molecular structure, spectroscopy, electron-induced processes, and scattering dynamics.

Authors	**Type of study**	**Method / Conditions**	**Main results**
Hermann et al. [26]	Molecular structure + conformational analysis	Gas Electron Diffraction (GED) + quantum chemical calculations	Two conformers in gas phase; dominant trans C–C–O–C skeleton; CHF_2 trans orientation; minor gauche conformer
Matias et al. [27]	Electron-induced fragmentation (DEA)	Crossed electron–molecular beam (0–17 eV)	Formation of Cl^-, F^- fragments; resonances at 2–3 eV and 9 eV; Cl^- peak at ∼0.6 eV
González-Méndez et al. [28]	Negative ion chemistry (IMS–MS)	Ion mobility spectrometry–mass spectrometry; cluster formation analysis	Cl^- signals due to impurities; high vertical attachment energy suppresses DEA; ions mainly from clustering processes
Lange et al. [29]	Electronic excitation + photoabsorption	Synchrotron radiation (5.0–10.8 eV)	Low-lying valence and Rydberg states; identification of singlet and triplet excitations
Kopyra et al. [30]	Electron-impact fragmentation	Electron collision experiments + theoretical modelling	Energy-dependent fragmentation; strong electron-driven dissociation pathways
E. Lange (PhD thesis) [31]	Elastic electron scattering	SMCPP + IAM-SCAR+I + experiment (10–50 eV, 8°–70°)	DCS, ICS, MTCS; good agreement between experiment and calculations

1.5.3 Sevoflurane

Sevoflurane is a widely used halogenated inhalation anesthetic characterized by a fully fluorinated structure, which makes it particularly relevant for studies of electron–molecule interactions, scattering processes, and atmospheric chemistry. Its relatively large size, high polarizability, and permanent dipole moment contribute to complex collision dynamics, making it a suitable system for both experimental and theoretical investigations. A summary of the most relevant experimental and theoretical studies on sevoflurane is given in Table 1.3.

From a structural perspective, Tang et al. [21] also investigated sevoflurane alongside halothane, providing insight into its molecular geometry and charge distribution. Their results confirmed the influence of fluorine substitution on the electronic density and dipole moment, which are key factors governing intermolecular interactions and scattering behavior.

Electron scattering from sevoflurane has been investigated in several studies. Lozano et al. [32] reported total electron scattering cross sections over a broad energy range, showing good agreement with theoretical calculations based on the IAM-SCAR+I approach and confirming its applicability to complex polyatomic systems.

The electronic excitation spectrum of sevoflurane has also been examined together with isoflurane by Lange et al. [**?**]. Using synchrotron-based photoabsorption spectroscopy combined with quantum chemical calculations, low-lying valence and Rydberg states were identified in the 5.0–10.8 eV energy range, providing insight into the excited-state structure relevant for photon-induced processes.

A detailed investigation of the conformational properties of sevoflurane was reported by Lesarri et al. [33], who employed Fourier-transform microwave spectroscopy supported by ab initio calculations. The study showed that, under isolated gas-phase conditions, sevoflurane predominantly adopts a single stable conformation characterized by a gauche fluoromethoxy group and a near-symmetric arrangement of the molecular backbone. The experimentally determined structure and dipole moment components provide an accurate description of the molecular geometry relevant for interaction processes.

Table 1.3: Summary of previous experimental and theoretical studies on sevoflurane relevant to its molecular structure, spectroscopy, electron-induced processes, and scattering dynamics.

Authors	**Type of study**	**Method / Conditions**	**Main results**
Tang et al. [21]	Molecular structure + electronic properties	Quantum chemical calculations	Charge distribution and dipole moment; influence of fluorination on electronic structure
Lesarri et al. [33]	Molecular structure + conformational analysis	Fourier-transform microwave spectroscopy + ab initio calculations	Dominant stable conformer; accurate gas-phase geometry and dipole components
Dom et al. [35]	Intermolecular interactions	Spectroscopy + theoretical calculations (C–H$\cdots\pi$ complexes)	Stable weak complexes; binding energies confirm role of dispersion and weak hydrogen bonding
Lozano et al. [32]	Electron scattering (TCS)	Magnetic beam experiment (1–300 eV) + IAM-SCAR+I	Total cross sections; good agreement with theoretical predictions
Kaur et al. [34]	Electron scattering (theory)	Single-centre expansion + model potentials (1 eV–5 keV)	DCS, ICS, ionization cross sections; importance of polarization effects
Lange et al. [29]	Electronic excitation + photoabsorption	Synchrotron radiation (5.0–10.8 eV)	Low-lying valence and Rydberg states; consistent with isoflurane

A recent theoretical study by Kaur et al. [34] reported a comprehensive set of electron-impact scattering cross sections for sevoflurane over a wide energy range from 1 eV up to 5 keV. Elastic differential and integral cross sections were calculated using the single-centre-expansion formalism with model potentials, while ionization cross sections were obtained using the binary-encounter-Bethe approach. The results show good agreement with available experimental total cross sections, confirming the reliability of simplified theoretical approaches for describing electron scattering from complex polyatomic molecules.

Intermolecular interactions of sevoflurane were investigated by Dom et al. [35], who studied weak C–H$\cdots\pi$ hydrogen-bonded complexes formed between sevoflurane and benzene using a combination of spectroscopic measurements and theoretical calculations. The results showed that such weak interactions are energetically stable, with experimentally and theoretically determined binding energies in very good agreement, providing insight into the role of dispersion and weak hydrogen bonding in stabilizing molecular complexes.

1.5.4 Desflurane

Desflurane has been studied as a representative fluorinated ether anesthetic due to its structural similarity to related compounds such as isoflurane and sevoflurane. Its molecular structure and conformational flexibility have been the subject of both experimental and theoretical investigations. A concise overview of the most relevant previous experimental and theoretical studies is presented in Table 1.4.

The gas-phase molecular structure and conformational properties of desflurane, together with isoflurane, were studied using gas electron diffraction combined with quantum chemical calculations [26]. The results showed that both molecules exist as mixtures of two conformers, where the most stable form is characterized by an almost trans arrangement of the C–C–O–C backbone and a trans-oriented CHF_2 group. The less stable conformer adopts a gauche orientation of this group, indicating the importance of subtle steric and electronic effects in determining the equilibrium structure.

The conformational preferences and microsolvation effects of desflurane were further investigated using MP2 and DFT calculations [36]. It was found that the two lowest-energy conformers are nearly isoenergetic, with their relative stability mainly governed by weak in-

tramolecular F$\cdots$H interactions. In addition, both conformers form stable complexes with a single water molecule through CH$\cdots$O and OH$\cdots$F hydrogen bonding, while fluorinated ether groups exhibit noticeable charge-transfer effects upon hydration.

Reaction dynamics of desflurane with chlorine atoms were studied theoretically by Zierkiewicz [37] using high-level CCSD(T)/CBS calculations. Hydrogen abstraction from the CHF group was identified as the most favorable reaction pathway, proceeding through a multi-step mechanism. All investigated channels were found to be slightly endothermic, with reaction enthalpies in the range of approximately 1.2 to 5.3 kcal mol^{-1}, providing detailed insight into the energetics and preferred reaction routes.

Vibrational properties and conformational behavior of desflurane were investigated experimentally and theoretically using FT-IR and Raman spectroscopy in combination with ab initio calculations [38]. The results indicated that only the two lowest-energy conformers significantly contribute to the observed spectra, while temperature-dependent spectral changes were attributed to conformational redistribution. The study also suggested weak complex formation with methyl fluoride, stabilized by non-classical hydrogen bonding interactions.

Further spectroscopic insight was obtained from vibrational absorption and circular dichroism measurements in solution [39]. Combined with theoretical modelling, these data enabled the identification of dominant conformers and provided detailed information on the stereochemical characteristics of desflurane in the studied spectral range.

Overall, these studies demonstrate that the structural flexibility, weak intermolecular interactions, and conformational dynamics of desflurane play a central role in determining its physical and chemical behavior.

Available literature does not include studies on electron-scattering cross sections for desflurane (DCS, ICS, MTCS, or TCS). Therefore, the present work represents a first step in this direction for this molecule.

Table 1.4: Summary of previous experimental and theoretical studies on desflurane relevant to its molecular structure, spectroscopy, intermolecular interactions, and reaction dynamics.

Authors	**Type of study**	**Method / Conditions**	**Main results**
Hermann et al. [26]	Molecular structure + conformational analysis	Gas Electron Diffraction (GED) + quantum chemical calculations	Two conformers in gas phase; dominant trans C–C–O–C backbone; CHF_2 trans orientation; minor gauche conformer
Sutradhar et al. [36]	Conformational analysis + microsolvation	MP2 and DFT calculations; water complexation studies	Nearly isoenergetic conformers; stability governed by weak F$\cdots$H interactions; CH$\cdots$O and OH$\cdots$F water complexes
Zierkiewicz [37]	Reaction dynamics	CCSD(T)/CBS calculations; Cl-atom reactions	Hydrogen abstraction from CHF group dominant pathway; all channels slightly endothermic (1.2–5.3 kcal mol^{-1})
Melikova et al. [38]	Vibrational spectroscopy + conformations	FT-IR (cryospectroscopy) + Raman + ab initio calculations	Two main conformers observed; temperature-dependent spectral changes; weak complex formation indicated
Polavarapu et al. [39]	Vibrational absorption + VCD analysis	Vibrational circular dichroism (VCD) + theoretical modelling	Identification of dominant conformers; stereochemical characterization in solution

1.6 Scope and Objectives of the Present Work

The interaction of low- and intermediate-energy electrons with complex polyatomic molecules represents a fundamental problem in atomic and molecular physics, with significant implications for fields such as radiation chemistry, atmospheric physics, and medical physics. In particular, halogenated anesthetic molecules, due to their structural complexity, high polarizability, biological importance, and pronounced environmental relevance—including their relatively long atmospheric lifetimes, high global warming potentials (GWPs), and contribution to greenhouse gas emissions—constitute challenging targets for both experimental and theoretical investigations of electron–molecule scattering processes.

Despite numerous studies addressing the electronic structure, fragmentation dynamics, and photon-induced processes in molecules such as sevoflurane, isoflurane, and halothane, experimental data on elastic electron scattering remain limited, especially in the intermediate energy range. Furthermore, for certain molecules such as desflurane, no experimental differential or integral cross-section data are currently available. This lack of comprehensive and systematically obtained scattering data hinders the accurate modelling of electron transport and interaction processes in biologically relevant media, as well as in atmospheric and environmental contexts where electron-driven processes can influence molecular stability and decomposition pathways.

The primary scope of the present work is therefore to perform a detailed experimental investigation of elastic electron scattering from four representative volatile anesthetic molecules—sevoflurane, isoflurane, halothane, and desflurane—in the gas phase and in the intermediate electron energy range. The study is based on the crossed electron–molecular beam technique, which enables precise determination of angular distributions of scattered electrons and, consequently, differential cross sections (DCSs).

The main objectives of this dissertation can be summarized as follows:

- To measure relative and absolute differential cross sections for elastic electron scattering from the selected anesthetic molecules over a range of incident electron energies and scattering angles;
- To derive integral cross sections (ICSs) and momentum transfer cross sections (MTCSs) from the measured DCS data, providing a more complete description of the scattering process;
- To compare the obtained experimental results with available theoretical calculations, particularly those based on the Independent Atom Model with screening-corrected additivity rules and interference effects (IAM-SCAR+I), in order to assess the validity and limitations of these approaches for complex polyatomic systems;
- To identify systematic trends in the scattering behavior as a function of molecular structure, such as the role of halogen substitution, molecular size, dipole moment, and degree of fluorination;
- To provide the first set of experimental electron scattering cross-section data for desflurane, thereby filling an important gap in the existing literature;
- To contribute to the broader understanding of electron-driven processes in biologically and environmentally relevant molecules, with potential applications in radiation damage modelling, plasma medicine, and the assessment of atmospheric degradation mechanisms of greenhouse gases.

Through these objectives, the present work aims to extend the existing database of electron–molecule scattering cross sections and to provide reliable experimental benchmarks for future theoretical developments, particularly for complex halogenated systems of both biomedical and environmental significance.

1.7 Structure of the Thesis

The present dissertation is structured in a systematic manner in order to provide a coherent and logically consistent development of the investigated problem, from the general physical context to the detailed analysis of the obtained results.

Chapter 1 introduces the scientific background and motivation of the study. It includes an overview of the historical development and classification of anesthetic agents, as well as a discussion of their chemical structure and physicochemical properties. The fundamental principles underlying their anesthetic action are outlined, and particular attention is devoted to their environmental impact, especially in the context of greenhouse gas emissions. Furthermore, a comprehensive review of previous experimental and theoretical investigations of the selected molecules is presented. The chapter concludes with a clear formulation of the scope and objectives of the present work.

Chapter 2 provides the theoretical framework necessary for the description and interpretation of electron–molecule scattering processes. Starting from the fundamental concepts of collision theory, the formal definition of differential and integral cross sections is introduced. The partial wave expansion method is then developed in detail, including its connection to measurable quantities via the scattering amplitude and the optical theorem. Subsequently, the Independent Atom Model (IAM) and its refined variants, incorporating screening corrections and interference effects, are discussed as practical approaches for treating complex molecular targets.

Chapter 3 is devoted to the experimental methodology. It contains a detailed description of the experimental apparatus employed in this work, with particular emphasis on the UGRA electron spectrometer. The operating principles of its main components are presented, including the electron source, energy analyzer, and detection system. The procedures for measuring relative and absolute differential cross sections are described in a rigorous manner, together with the methods used for data normalization and the evaluation of experimental uncertainties.

Chapter 4 presents the results obtained in this study and their detailed analysis. The measured differential cross sections, as well as the derived integral and momentum transfer cross sections, are reported for each of the investigated molecules: halothane, isoflurane, sevoflurane, and desflurane. A systematic comparison with available theoretical predictions and literature data is carried out, with the aim of assessing the consistency and reliability of the results. Particular emphasis is placed on the identification of trends related to molecular structure and on the role of electron–molecule interaction mechanisms.

Chapter 5 summarizes the main findings of the dissertation and formulates the principal conclusions. In addition, possible directions for future research are outlined, both in terms of further experimental investigations and the development of improved theoretical models for complex polyatomic systems.

The dissertation is completed by a comprehensive list of references and an appendix containing supplementary material relevant to the presented analysis.

Chapter 2

Theoretical Background

A clear theoretical framework is essential for understanding electron–molecule scattering and for interpreting the experimental results presented later in this work. Since scattering is a fundamental process in atomic and molecular physics, the basic concepts must first be outlined before moving to more specific models relevant to the present study. In this chapter the focus will be on elastic scattering, where the energy of the incident electron is conserved, as this process provides direct information about the effective interaction potential within the molecule.

The chapter begins with a brief overview of the general concepts of scattering theory, introducing the scattering amplitude and the relation between differential and integral cross sections. The independent atom model (IAM) is then presented as a practical approximation, together with its limitations and the corrections needed when interatomic interference and multiple scattering effects become important. In this context, the role of screening corrections (SCAR), interference contributions, and the additivity rule (AR) is discussed, as well as their reformulations when applied to molecular systems.

Finally, attention is given to specific cases where additional effects must be taken into account, such as the influence of molecular dipole moments or the corrections required at intermediate electron energies. The material presented in this chapter provides the theoretical basis for the methodologies and interpretations used throughout the rest of the thesis.

2.1 Types of collision

To describe the process of electron scattering by a molecular target, we consider a homogeneous, well-collimated beam of monoenergetic electrons with energy E_{in} and initial wave vector $\vec{k}_{\text{in}}$, which is directed towards a target molecule (AB). The electrons propagate along the z-axis, so $\vec{k}_{\text{in}} = k_{\text{in}}\hat{z}$, and are scattered, emerging with a final energy and wave vector, E_{r} and $\vec{k}_{\text{r}}$, respectively. It is assumed that the experimental setup ensures that each molecule scatters the incoming electrons independently, as if isolated. The scattered electrons are detected beyond the range of the interaction potential, and the detector records the angle at which the electrons are scattered following the interaction. Several processes may arise (Figure 2.1):

1. **Elastic scattering** where no energy is transferred to the internal degrees of freedom of the molecule, so the electronic and nuclear (vibrational and rotational) states of the molecule remain unchanged after the collision. However, the scattered electron may continue to move in a different direction and orientation from its initial path.

   Elastic scattering arises from the interaction of the incident electron with the effective molecular potential, which includes electrostatic, exchange, and polarization contributions. The relative importance of these interactions depends on the incident electron

energy and the structural properties of the target molecule. In general, long-range interactions such as polarization are more significant at lower energies, while short-range interactions dominate at higher energies. Despite the absence of internal excitation, elastic scattering reflects the spatial distribution of the molecular potential and provides insight into the electronic structure of the target.

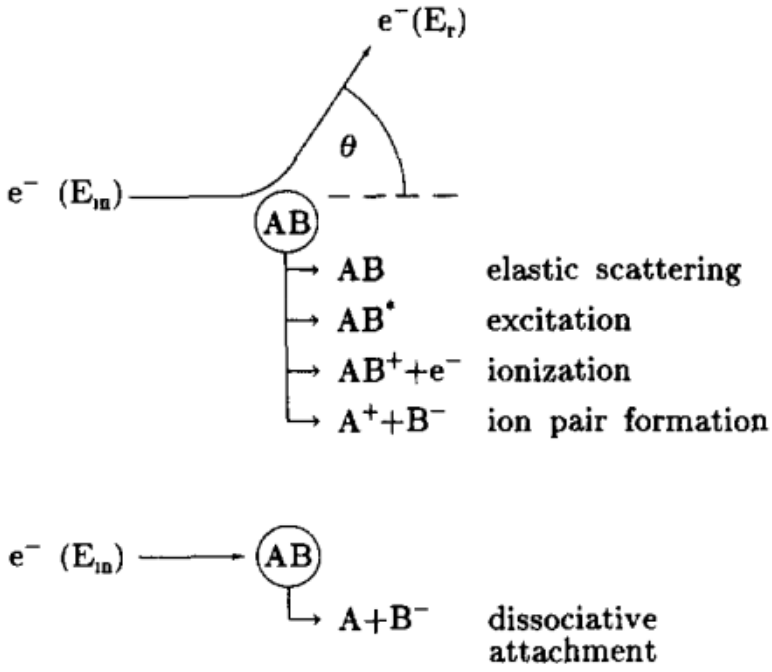

Figure 2.1: The diagram illustrates the process of electron scattering on a molecule and some possible outcomes. An incident electron with a known energy E_{in} collides with a molecular target AB, and may transfer a portion of its initial energy, ΔE, to the target and scatter at an angle relative to its original direction, retaining a residual energy. The excited target AB^* may subsequently emit a photon or undergo dissociation (dissociative excitation). The target may also temporarily capture the incident electron and later dissociate into a neutral and a stable negative fragment, as shown in the lower part of the Figure [40].

2. **Inelastic scattering**, where the incident electron transfers part of its energy to the internal degrees of freedom of the target molecule, and can be classified as following [1].

   - **Rotational excitation**
     A collision with a charged projectile induces changes in the rotational state of the molecule. This scattering process is particularly important in the case of polar molecules, where the long-range dipole potential strongly enhances the interaction with low-energy electrons.

     Rotational excitation involves very small energy transfers, typically in the meV range, and is therefore most significant at low incident electron energies and small scattering angles. The corresponding cross sections often exhibit a strong forward-peaked behaviour. Due to the limited energy resolution of most electron scattering experiments, rotationally inelastic processes are commonly indistinguishable from elastic scattering and are therefore included in the quasi-elastic signal.

[1] The asterisk (*) denotes that the atom or molecule is in an excited state.

- **Vibrational excitation**
  The interaction of the incident electron with the molecule induces a change in its vibrational state. This process involves energy transfers typically ranging from a few tenths of an eV up to about 1 eV, depending on the molecular vibrational modes.

  Vibrational excitation can occur via direct scattering, driven by the short-range interaction potential, or through resonant mechanisms involving temporary electron capture. In the latter case, the formation of a transient negative ion significantly enhances the excitation probability. This process plays an important role in energy transfer and redistribution in molecular gasses and plasmas.

- **Electronic excitation**
  After the collision, the target molecule is left in an electronically excited state, meaning that one of its bound electrons is promoted to a higher energy level. This process requires larger energy transfer compared to rotational and vibrational excitation, typically several electronvolts.

  Electronic excitation is often accompanied by subsequent processes such as photon emission (radiative decay) or molecular fragmentation (dissociative excitation). These channels are particularly relevant in atmospheric physics, plasma environments, and radiation chemistry, where they contribute to the production of reactive species.

- **Ionization**
  In this case, the incident electron has sufficient energy to remove a bound electron from the target molecule, leading to the formation of a positive ion and two outgoing electrons. This process occurs when the incident energy exceeds the ionization threshold of the molecule.

  Ionization is one of the dominant scattering channels at intermediate and high electron energies. It plays a crucial role in electron transport phenomena, gas discharges, and plasma formation, as it leads to the generation of secondary electrons that can further induce additional ionization events.

- **Dissociative electron attachment and auto-detachment**
  A collision is considered fast when the velocity of the incoming electron is significantly greater than that of the target electrons; under such conditions, the incident electron acts as a weak perturbation. However, when the velocities of the incident and target electrons are comparable, the incoming electron may be temporarily captured by the molecule, forming a transient negative ion state.

  This intermediate state, often referred to as a resonance, can decay through different pathways. In dissociative electron attachment, the molecule fragments into a neutral and a negative ion:

  $$e^- + AB \rightarrow [AB^-]^* \rightarrow A + B^- \qquad \text{dissociative electron attachment}$$

  Alternatively, the temporary anion may release the additional electron, leaving the molecule in an excited or ground state:

  $$e^- + AB \rightarrow [AB^-]^* \rightarrow AB^* + e^- \qquad \text{auto-detachment}$$

  These resonant processes are highly energy-dependent and are particularly important at low and intermediate electron energies, where they can significantly enhance inelastic cross sections.

The different scattering processes described above are well documented in the literature [41–51].

A specific mode of interaction or fragmentation of the composite system formed by the incident electron and the target molecule AB during a collision is called a channel. It is characterized by the number and type of particles resulting from the interaction. In elastic scattering, the electron and the molecule remain in their initial states, meaning the system stays within the same channel. In inelastic or reactive collisions, the system transitions from an initial to a different final channel. A channel is considered open if the process it represents is permitted by conservation laws (such as energy conservation); otherwise, it is referred to as closed.

2.2 Cross section

In the context of collision experiments, the concept of cross-section is a fundamental measure used to characterize the likelihood of specific interaction outcomes. In the formulation provided by Bransden and Joachain [43], the cross section is defined as:

> *"The cross-section for a certain type of event in a given collision is defined as the ratio of the number of events of this type per unit time and per unit scatterer, to the flux of the incident particles with respect to the target."*

Owing to the fact that cross-sections are inherently independent of the incident particle flux, it is customary to normalize this quantity to unity. Consequently, cross-sections can equivalently be described as *"transition probabilities per unit time, per unit target scatterer and per unit flux of the incident particles with respect to the target."* [52]

Consider the scattering process between an incident electron beam and a molecular target. Let N_e denote the flux of incident electrons, defined as the number of electrons crossing a unit area per unit time, perpendicular to the beam direction and at rest relative to the target. Let n_M represent the number of target molecules available to interact with the electron beam. If we denote by N_{sc} the total number of electrons scattered per unit time as a result of collisions between the incoming electrons and the target molecules, then the scattering process can be quantitatively described based on these parameters:

$$N_{\text{sc}} = N_e n_M \sigma_{\text{sc}} \tag{2.1}$$

In this context, σ_{sc} represents the total cross-section for the given scattering process. Total cross-sections for elastic scattering, inelastic scattering, and other possible interaction channels can be defined analogously. If we denote by N_{tot} the total number of incident electrons that have interacted per unit time with the target molecules, then the total cross-section σ_{tot} is given by:

$$N_{\text{tot}} = N_e n_M \sigma_{\text{tot}} \tag{2.2}$$

If only elastic scattering occurs between the electrons and the target molecules, then σ_{tot} reduces to the integral elastic cross-section σ_{el}. However, when additional scattering channels are open (such as rotational, vibrational, or electronic excitation, or ionization), the total cross-section becomes the sum of the integral cross-sections corresponding to each open channel:

$$\sigma_{\text{tot}} = \sum_i \sigma_i \tag{2.3}$$

where σ_i denotes the integral cross-section for the i-th open channel.

If the electron were treated as a classical point-like particle and the atomic target as a rigid sphere of radius a, the collision cross-section would simply be given by the geometric cross-section, πa^2. However, since electrons obey the laws of quantum mechanics, they also exhibit wave-like behavior. Moreover, atomic or molecular targets do not have sharply defined boundaries. As a result, the collision cross-section is not a constant but rather depends on the incident electron energy E_{in}.

It is clear from the above discussion that total cross-sections have the dimensions of an area. In atomic units (a.u.), the natural unit of length is the Bohr radius $a_0 \approx 5.29 \times 10^{-11}\,\text{m}$, so it is convenient to express atomic cross-sections in units of $a_0^2 \approx 2.80 \times 10^{-21}\,\text{m}^2$. Alternatively, cross-sections are also frequently reported in units of $\pi a_0^2 \approx 8.80 \times 10^{-21}\,\text{m}^2$.

2.2.1 Differential cross-section

Continuing with the description of the scattering process, let us define the concept of the differential cross section, which quantitatively describes the probability that an incoming electron is scattered into a specific direction.

Consider a uniform beam of non-interacting, monoenergetic electrons incident on a molecular target consisting of n identical and well-separated molecules. It is assumed that the molecules are spaced far enough apart to ensure that each scattering event involves only one molecule, and that the target is sufficiently thin so that multiple scattering can be neglected. The electrons, each with mass m, travel from infinity with velocity v, along the Z-axis.

Let N denote the number of incident electrons, with well defined energy E_{in}, crossing a unit area perpendicular to the beam per unit time—this defines the incident flux. Let $\mathrm{d}N'$ represent the number of electrons scattered per unit time into a small solid angle $\mathrm{d}\Omega$, centered about the direction $\Omega \equiv (\theta, \phi)$, where θ and ϕ are the polar and azimuthal angles with respect to the beam axis.

Under the experimental conditions described above, the number of scattered electrons $\mathrm{d}N'$ detected per unit time within the solid angle $\mathrm{d}\Omega$ is found to be directly proportional to the incident flux N, the number density of target molecules n, and the size of the solid angle $\mathrm{d}\Omega$. This allows us to express the observed count rate as:

$$\mathrm{d}N' = Nn\,\sigma(E_{\text{in}}, \theta, \phi)\,\mathrm{d}\Omega, \tag{2.4}$$

where $\sigma(E_{\text{in}}, \theta, \phi) \equiv \frac{\mathrm{d}\sigma(E_{\text{in}}, \theta, \phi)}{\mathrm{d}\Omega}$ is the proportionality factor known as the *differential scattering cross section*. It describes the probability that an electron is scattered into a given direction (θ, ϕ) per target molecule and per unit solid angle. The unit of measurement for the differential cross section with respect to angle is expressed in square meters per steradian [m^2/sr].

In many scattering experiments, the target molecules are randomly oriented in space, making it possible to determine only the orientation-averaged cross section. As a consequence, the differential cross section becomes independent of the azimuthal angle ϕ. Furthermore, due to the finite energy and angular resolution of the detection system, the measured cross section represents a value averaged over these experimental variables.

Thus, the experimentally determined differential cross section, for a given incident energy E_{in}, is expressed as:

$$\text{DCS}(E_{\text{in}}, \theta) = \frac{\mathrm{d}\sigma(E_{\text{in}}, \theta)}{\mathrm{d}\Omega}, \tag{2.5}$$

where $\text{DCS}(E_{\text{in}}, \theta)$ represents the number of scattered electrons per unit solid angle, averaged over molecular orientations and experimental resolution, at the scattering angle θ and incident electron energy E_{in}.

The *total scattering cross section* is obtained by integrating the differential cross section over all scattering angles. This means summing the contributions from all directions into which scattering can occur. Mathematically, it is expressed as:

$$\sigma_{\text{tot}}(E_{\text{in}}) = \int \frac{\mathrm{d}\sigma(E_{\text{in}},\theta)}{\mathrm{d}\Omega}\,\mathrm{d}\Omega = 2\pi \int_0^{\pi} \frac{\mathrm{d}\sigma(E_{\text{in}},\theta)}{\mathrm{d}\Omega}\,\sin\theta\,\mathrm{d}\theta. \tag{2.6}$$

The total electron scattering cross section introduced above represents the sum of the integral cross sections corresponding to all energetically allowed (open) scattering channels (as in Equation 2.3).

Below the first inelastic threshold, the total electron scattering cross section reduces to the integral cross section for elastic scattering. In this study, the main focus is on the **differential cross section for elastic electron scattering**, $\frac{\mathrm{d}\sigma_{el}}{\mathrm{d}\Omega}$, which is defined as the number of electrons scattered per unit of time into a differential solid angle element $\mathrm{d}\Omega$ in the direction specified by the angles $(\theta\,,\phi)$, as a result of the interaction between an incident electron beam of unit flux and a molecular (or atomic) target.

2.3 General Characteristics of Potential Scattering

Let us examine the non-relativistic scattering of a spinless particle with mass m in the presence of a potential $V(\mathbf{r})$. The dynamics of the system are governed by the time-dependent Schrödinger equation:

$$\left(-\frac{\hbar^2}{2m}\nabla^2 + V(\mathbf{r})\right)\Psi(\mathbf{r},t) = i\hbar\frac{\partial}{\partial t}\Psi(\mathbf{r},t). \tag{2.7}$$

This equation admits stationary-state solutions of the form:

$$\Psi(\mathbf{r},t) = \psi(\mathbf{r})\,e^{-iEt/\hbar}, \tag{2.8}$$

where the spatial wave function $\psi(\mathbf{r})$ satisfies the time-independent Schrödinger equation

$$\left(-\frac{\hbar^2}{2m}\nabla^2 + V(\mathbf{r})\right)\psi(\mathbf{r}) = E\psi(\mathbf{r}), \tag{2.9}$$

The energy E of the particle is well-defined.

For convenience, we introduce the *reduced potential* $U(\mathbf{r})$, defined as:

$$U(\mathbf{r}) = \frac{2m}{\hbar^2}V(\mathbf{r}). \tag{2.10}$$

Using this substitution, the time-independent Schrödinger equation becomes:

$$\left[\nabla^2 + k^2 - U(\mathbf{r})\right]\psi(\mathbf{r}) = 0. \tag{2.11}$$

In the following analysis, we assume that the potential $V(\mathbf{r})$ decreases more rapidly than $1/r$ as $r \to \infty$. Under this condition, the scattering wave function, denoted $\psi_{\mathbf{k}}(\mathbf{r})$, satisfies the free-particle Schrödinger equation in the asymptotic region:

$$\left(\nabla^2 + k^2\right)\psi_{\mathbf{k}}(\mathbf{r}) = 0, \tag{2.12}$$

At large distances, the wave function can be written as the sum of the incident and scattered components:

$$\psi_{\mathbf{k}}(\mathbf{r}) \approx \psi_{\text{in}}(\mathbf{r}) + \psi_{\text{sc}}(\mathbf{r}), \tag{2.13}$$

where ψ_{in} represents the incident plane wave, and ψ_{sc} describes the scattered part of the wave.

Assuming the incident particles are monoenergetic and propagate along the direction of the wave vector $\mathbf{k}_i$, which we take to be aligned with the z-axis, the incident wave can be expressed as:

$$\psi_{\text{in}}(\mathbf{r}) = Ae^{i\mathbf{k}_i\cdot\mathbf{r}} = Ae^{ikz}, \tag{2.14}$$

where A is a normalization constant.

Far from the scattering center, the scattered part of the wave function must describe an outgoing flux of particles radiating away from the target. In this asymptotic region, the scattered wave resembles a spherical wave whose amplitude depends on the direction $\mathbf{r}$ and the energy E (or, equivalently, on the wave number k). The scattering wave function in this region can be written as:

$$\psi_{\text{sc}}(\mathbf{r}) \approx A\frac{f(E,\theta,\phi)}{r}e^{ikr}, \tag{2.15}$$

where θ and ϕ are the polar and azimuthal angles of the position vector $\mathbf{r}$, measured relative to the direction of the incident beam (taken along the z-axis). Hence, the full wave function $\psi_{\mathbf{k}}(\mathbf{r})$ in the large r limit takes the following asymptotic form:

$$\psi_{\mathbf{k}}(\mathbf{r}) \underset{r\to\infty}{\sim} A\left[e^{ikz} + \frac{f(E,\theta,\phi)}{r}e^{ikr}\right], \tag{2.16}$$

where the first term represents the incoming plane wave and the second term corresponds to the outgoing scattered wave.

The function f, known as the *scattering amplitude*, is a fundamental quantity in scattering theory, as it is directly linked to the differential cross section via the relation:

$$\frac{d\sigma}{d\Omega} = |f(E,\theta,\phi)|^2 \tag{2.17}$$

Equation 2.17 provides the essential connection between the asymptotic form of the wave function $\psi_{\mathbf{k}}(\mathbf{r})$ and the measurable quantity—the differential cross section. This relationship is of fundamental importance, as it bridges the theoretical framework with experimental observations.

2.4 The Partial Wave Method

As established in previous section, both the scattering amplitude and the cross sections are governed by the asymptotic behaviour of the stationary scattering wave function. In this chapter, we focus on exploiting this property in the special case of a central potential, i.e., a potential that depends solely on the distance r from the scattering center. Under such conditions, the solutions of the Schrödinger equation 2.9 can be separated in spherical polar coordinates, allowing us to establish a clear relation between the radial solutions and the asymptotic form of the scattering wave function. This approach, commonly referred to as the *partial waves method*, provides a systematic way to extract the scattering amplitude and corresponding cross sections [44].

Let us now examine the scattering of a spinless particle of mass m by a real central potential $V(r)$. We employ a spherical coordinate system in which the z-axis is aligned with the incident beam, while the origin is chosen at the center of the potential, coinciding with the position vector $\mathbf{r}$. Since the potential is central, the Hamiltonian H, together with the angular momentum

operators L^2 and L_z, mutually commute. This allows us to search for eigenfunctions that are common to all three operators. As a consequence, the scattering wave function can be expanded into partial waves characterized by definite quantum numbers l and m:

$$\psi_k(\mathbf{r}) = \sum_{l=0}^{\infty} \sum_{m=-l}^{l} c_{lm}(k)\, R_l(k,r)\, Y_{lm}(\theta,\phi). \tag{2.18}$$

Here the dependence on the wave number $k = \sqrt{2mE}/\hbar$ is made explicit both in the expansion coefficients $c_{lm}(k)$ and in the radial functions $R_l(k,r)$. The functions $Y_{lm}(\theta,\phi)$ are the spherical harmonics, which describe the angular dependence of the wave function in spherical coordinates. The essence of the partial waves method is to exploit this expansion in order to derive a practical expression for the scattering amplitude.

Because the incident beam is directed along the z-axis, the system is axially symmetric with respect to this axis. Consequently, only the terms with $m = 0$ contribute to the expansion. The scattering wave function can then be written in the simplified form

$$\psi_k(\mathbf{r}) = \sum_{l=0}^{\infty} c_l(k)\, R_l(k,r)\, Y_{l0}(\theta), \tag{2.19}$$

where the spherical harmonics reduce to

$$Y_{l0}(\theta) = \sqrt{\frac{2l+1}{4\pi}}\, P_l(\cos\theta), \tag{2.20}$$

with P_l denoting the Legendre polynomials. This result greatly simplifies the analysis, since the angular dependence of the scattering process is now fully described in terms of $P_l(\cos\theta)$.

Let us now focus on the radial part of the problem. In order to simplify the radial Schrödinger equation, it is convenient to introduce the new function

$$u_l(k,r) = r\, R_l(k,r), \tag{2.21}$$

together with the reduced potential $U(r)$, as already defined in 2.10. This substitution eliminates the first derivative term that would otherwise appear in the radial equation when expressed in spherical coordinates. The radial equation then takes the compact form

$$\left[\frac{d^2}{dr^2} + k^2 - \frac{l(l+1)}{r^2} - U(r)\right] u_l(k,r) = 0. \tag{2.22}$$

At large distances $r \to \infty$, the radial wave functions $R_l(k,r)$ take the asymptotic form

$$R_l(k,r) \sim \frac{1}{kr} \sin\left(kr - \frac{l\pi}{2} + \delta_l(k)\right), \tag{2.23}$$

where $\delta_l(k)$ are the so-called phase shifts, which contain all the information about the interaction potential[2], and can be obtained from expresion:

$$\tan\delta_l(k) = -k \int_0^{\infty} j_l(kr)\, U(r)\, R_l(k,r)\, r^2\, dr, \tag{2.24}$$

where $j_l(kr)$ is the spherical Bessel function.

[2]The phase shift $\delta_l(k)$ quantifies how much the presence of the scattering potential modifies the phase of the l-th partial wave compared to free motion. Physically, it measures the delay (or advance) of the scattered wave due to the interaction with the target.

Inserting this asymptotic form into the partial wave expansion of the wave function 2.19 and comparing with the general scattering boundary condition 2.16, one obtains the expression for the scattering amplitude:

$$f(\theta) = \frac{1}{k}\sum_{l=0}^{\infty}(2l+1)\, e^{i\delta_l(k)} \sin\delta_l(k)\, P_l(\cos\theta). \tag{2.25}$$

If we use the expression 2.17, the corresponding differential cross section is given by [53]

$$\begin{aligned}\frac{d\sigma}{d\Omega}(k,\theta) = |f(k,\theta)|^2 = \frac{1}{k^2}\sum_{l=0}^{\infty}\sum_{l'=0}^{\infty}(2l+1)(2l'+1)\exp\{i\left[\delta_l(k)-\delta_{l'}(k)\right]\} \\ \times \sin\delta_l(k)\, \sin\delta_{l'}(k)\, P_l(\cos\theta)\, P_{l'}(\cos\theta).\end{aligned} \tag{2.26}$$

By using the orthogonality of the Legendre polynomials, one obtains for the total cross section

$$\sigma_{\text{tot}}(k) = 2\pi\int_0^{\pi}\frac{d\sigma}{d\Omega}(k,\theta)\, \sin\theta\, d\theta = \frac{4\pi}{k^2}\sum_{l=0}^{\infty}(2l+1)\, \sin^2\delta_l(k). \tag{2.27}$$

The total cross section is often expressed in terms of the effective cross sections of the individual partial waves,

$$\sigma_{\text{tot}}(k) = \sum_{l=0}^{\infty}\sigma_l(k), \tag{2.28}$$

where

$$\sigma_l(k) = \frac{4\pi}{k^2}(2l+1)\, \sin^2\delta_l(k). \tag{2.29}$$

2.4.1 Optical Theorem

Let us now return to relation 2.25. By noting that $P_l(0) = 1$, the scattering amplitude in the forward direction simplifies to

$$f(\theta=0) = \frac{1}{k}\sum_{l=0}^{\infty}(2l+1)\, e^{i\delta_l(k)} \sin\delta_l(k). \tag{2.30}$$

From this expression, we immediately obtain for its imaginary part

$$\text{Im}\, f(\theta=0) = \frac{1}{k}\sum_{l=0}^{\infty}(2l+1)\, \sin^2\delta_l(k). \tag{2.31}$$

A direct comparison with eq. 2.27 then leads to the important result

$$\sigma_{\text{tot}} = \frac{4\pi}{k}\,\text{Im}\, f(\theta=0), \tag{2.32}$$

which is the celebrated *optical theorem* [54], sometimes referred to as the Bohr-Peierls-Placzek relation. Physically, it arises from the conservation of probability flux: the destructive interference between the incident and scattered waves in the forward direction casts a "shadow" behind the target, reducing the intensity of the incident beam. As a result, the total number of scattered particles is directly proportional to the total cross section.

2.5 Molecular Scattering - The Independent Atom Model

Having introduced the general concepts of scattering theory and the formulation of cross sections in terms of the scattering amplitude, it is instructive to consider practical approximations that allow for the treatment of electron–molecule collisions. One of the most widely used approaches is the **Independent Atom Model (IAM)** [55–58], which provides a simplified but effective framework for describing molecular scattering processes.

The essential assumption of IAM is that the scattering of an electron from a molecule can be approximated as the incoherent sum of the scattering events of its individual atomic constituents. In this picture, the molecular target is decomposed into a set of atoms fixed at their equilibrium positions, and the complex electron–molecule interaction is reduced to a superposition of independent electron–atom collisions. The model therefore neglects any simultaneous interaction of the incident electron with more than one atomic center, as well as interference effects arising from the molecular electronic structure.

Despite these limitations, the IAM has proven to be a valuable tool for interpreting and predicting scattering data, particularly at medium and high electron impact energies, where the semiclassical nature of the approximation yields good agreement with experiment. However, for low energies (typically below 20 eV), where exchange and correlation effects, molecular binding, and multiple scattering contributions become increasingly important, the predictive accuracy of the model is considerably reduced [59].

To improve the performance of the IAM, several correction schemes have been introduced. **The Screening Corrected Additivity Rule (SCAR)** [60,61] accounts for the fact that inner atoms within a molecule are partially shielded by neighboring atoms, reducing their effective contribution to the overall cross section. Furthermore, the **interference correction** [62,63] explicitly considers the coherent superposition of the electron waves scattered by different atomic centers, thereby incorporating diffraction-like effects that become relevant at intermediate energies. In addition, for polar molecules, where long-range dipole interactions strongly affect the scattering dynamics, further modifications of the IAM are required to properly account for the enhanced forward scattering contribution.

The simplicity of the IAM, combined with these correction schemes, makes it a practical and flexible method for estimating molecular cross sections in cases where more elaborate ab initio approaches are computationally demanding. In the following section, the mathematical formulation of the IAM and its corrected variants will be presented, together with their applicability and limitations in the context of elastic electron scattering from molecular targets.

2.5.1 The Atomic Scattering Amplitudes

The scattering amplitudes of the constituent atoms of the investigated molecule can be obtained using equation 2.25. To determine the phase shift for the l-th partial wave, the radial equation 2.22 is solved numerically under the appropriate boundary conditions. In this procedure, the reduced potential $U(\mathbf{r})$ is replaced by a complex, spherically symmetric, and energy-dependent optical potential $V_{opt}(\mathbf{r})$ [57].

In general, the optical potential is written as the sum of a real and an imaginary part,

$$V_{\text{op}}(r) = V_R(r) + iV_I(r), \tag{2.33}$$

where the real part $V_R(r)$ describes the elastic interaction between the incident electron and the target, while the imaginary part $V_I(r)$ accounts for the absorption of flux into all energetically allowed inelastic channels. The inclusion of $V_I(r)$ ensures that the calculated scattering amplitudes reproduce the correct balance between elastic and inelastic processes, in agreement

with the optical theorem.

The real component $V_R(r)$ is given by:

$$V_R(r) = V_s(r) + V_{pol}(r) + V_{ex}(r). \tag{2.34}$$

where V_s is the static term obtained from a Hartree–Fock calculation of the atomic charge distribution [64], V_{ex} represents the exchange interaction arising from the indistinguishability of the incident and target electrons [65], and V_{pol} denotes the long-range polarization potential [66].

For the elastic scattering process, the calculations were performed without including the absorptive term $iV_I(r)$ in equation 2.33.

2.5.2 IAM Approach with Interference

Under the assumption of the Independent Atom Model (IAM) approximation, the molecular cross sections can be derived from the approximate expression for the multi-center scattering amplitude [67]:

$$F(\theta) \approx \sum_{i}^{\text{atoms}} f_i(\theta) e^{i\vec{q}\cdot\vec{r}_i}, \tag{2.35}$$

where $\vec{q} = \vec{k}_f - \vec{k}_i$ denotes the momentum transfer vector, $\vec{r}_i$ are the positions of the atomic centers, and $f_i(\theta)$ represent the individual atomic scattering amplitudes.

Since this expression corresponds to independent scattering from each atom, the IAM approximation is considered valid only when the interatomic distances are large compared to the wavelength of the incident electron.

Based on the molecular scattering amplitude, the differential elastic cross section for a molecule can be obtained by averaging the squared modulus of the scattering amplitude $F(\theta)$ over all molecular orientations [67, 68]:

$$\frac{d\sigma_{\text{elastic}}^{\text{molecule}}}{d\Omega} = \sum_{i,j} f_i(\theta) f_j^*(\theta) \frac{\sin(qr_{ij})}{qr_{ij}}\,, \tag{2.36}$$

which can be rewritten as

$$\frac{d\sigma_{\text{elastic}}^{\text{molecule}}}{d\Omega} = \sum_{i} |f_i(\theta)|^2 + \sum_{i\neq j} f_i(\theta) f_j^*(\theta) \frac{\sin(qr_{ij})}{qr_{ij}} = \sum_{i} \frac{d\sigma_{\text{elastic}}^{\text{atom } i}}{d\Omega} + \frac{d\sigma_{\text{interference}}}{d\Omega}\,, \tag{2.37}$$

where $q = |\vec{q}| = 2k\sin(\theta/2)$ is the momentum transfer and r_{ij} is the distance between atoms i and j. In the limit $qr_{ij} \to 0$, the second term approaches unity: $\frac{\sin(qr_{ij})}{qr_{ij}} = 1$.

The second term represents the interference contribution to the total differential elastic cross section, arising from the interaction of waves scattered by different atoms within the molecule. This contribution is particularly significant at small scattering angles, as it strongly affects the integrated cross section and must be taken into account in precise simulations, such as Monte Carlo calculations [69], and for experimental data normalization procedures [70].

Since only **elastic processes** are considered, which are sufficient for the objectives of this study, under these conditions the total cross section will be equal to the corresponding integrated elastic cross section.

By integrating equation 2.37, the total molecular cross section can be expressed as:

$$\sigma_{\text{elastic}}^{\text{molecule}} = \sum_{\text{atoms}} \sigma_{\text{elastic}}^{\text{atom } i} + \sigma_{\text{interference}} \tag{2.38}$$

where $\sigma_{\text{interference}}$ represents the integrated value of the interference contribution from the differential cross section discussed previously. It is important to note that this interference contribution would not appear in equation 2.38 if the total cross section were directly derived from equation 2.35 by applying the optical theorem. This approach is known as the **Additivity Rule (AR)** and has been extensively discussed in the literature [55, 56, 60, 61, 68, 71–78].

As discussed in [62], the exact expression is that given in equation 2.38, whereas the discrepancy with the AR approach arises from the approximate nature of equation 2.35, which does not fully satisfy the conditions of the optical theorem. It has also been shown that the interference terms are significant only at small scattering angles, yet their integrated contribution $\sigma_{\text{interference}}$ cannot be neglected even at high energies.

At intermediate energies (10–100 eV), where atomic cross sections are not small compared to the interatomic distances within the molecule, the IAM approximation ceases to be valid, as atoms can no longer be considered independent scattering centers and multiple scattering within the molecule becomes significant. Approximate methods have shown that significant corrections are required for the IAM approach within this energy range [58, 60, 74, 76, 79, 80]. It has also been demonstrated [60] that the energy range over which these corrections are relevant depends on the size of the molecule: for N_2 and CO, up to approximately 200 eV; for CO_2, up to 300 eV; and for benzene, even up to 600 eV.

2.5.3 IAM-SCAR Method

Representative calculations of molecular cross sections are based on a corrected version of the IAM approach, known as the **SCAR procedure (Screening Corrected Additivity Rule)**, which approximately accounts for the effects of multiple scattering [59, 60, 81].

In this method, the overlap between the total atomic cross sections is evaluated for each atom with respect to all others. For a pair of atoms i and j at a distance r_{ij}, the average mutual overlap is given by $\sigma_{ij} = \sigma_i\sigma_j/\alpha_{ij}$, with $\alpha_{ij} = \max(4\pi r_{ij}^2, \sigma_i, \sigma_j)$. Assuming $\sigma_i \geq \sigma_j$, for short interatomic distances ($4\pi r_{ij}^2 < \sigma_i$) the atoms are considered to fully overlap, i.e. $\sigma_{ij} = \sigma_j$, while for larger separations the screening is approximated as $\sigma_{ij} = \sigma_i\sigma_j/(4\pi r_{ij}^2)$, which corresponds to atom j covering a fraction $\sigma_j/(4\pi r_{ij}^2)$ of the solid angle around atom i, or vice versa [61].

For diatomic molecules, the resulting SCAR cross section can be written as $\sigma_{\text{SCAR}} = \sigma_1 + \sigma_2 - \sigma_{12}$. An equivalent representation is obtained as a weighted sum of the total atomic cross sections:

$$\sigma_{\text{elastic}}^{\text{molecule}} = \sum_{\text{atoms}} s_i \cdot \sigma_{\text{elastic}}^{\text{atom } i} \tag{2.39}$$

where the screening coefficients are defined as $s_i = 1 - \frac{1}{2}\sigma_{12}/\sigma_i$ for $i = 1, 2$. These coefficients can be interpreted as correction factors that account for the overlapped fraction of each atomic cross section which does not contribute to the molecular value.

For polyatomic molecules, screening corrections involving three or more atoms must be considered. These multiple overlaps can be approximately evaluated in a recursive manner, by accounting for the screening of each additional atom with respect to the previously corrected ones (see [60] for details). This procedure leads to the same general expression for the SCAR total cross section as in equation 2.39, with the screening coefficients given by

$$s_i = \sum_{k=1}^{N} \frac{(-1)^{k+1}}{k!}\, \varepsilon_i^{(k)}\,, \tag{2.40}$$

where N is the number of atoms in the molecule, and the parameters $\varepsilon_i^{(k)}$ arise from k-atom overlaps, defined recursively as

$$\begin{aligned} \varepsilon_i^{(1)} &= 1, \\ \varepsilon_i^{(k)} &= \frac{N-k+1}{N-1} \sum_{j(\neq i)} \frac{\sigma_j \, \varepsilon_j^{(k-1)}}{\alpha_{ij}} \qquad (k = 2, \ldots, N)\,, \end{aligned} \tag{2.41}$$

with the sum extending over all atoms of the molecule except the ith one.

It should be noted that this treatment enables an approximate evaluation of multiple overlaps in arbitrary molecules, requiring only the corresponding atomic cross sections and the relative positions of the constituent atoms. Importantly, it does not rely on molecular symmetry considerations and involves no adjustable parameters [61].

SCAR Extension to Elastic Differential Cross Sections

Calculating differential elastic molecular cross sections requires additional considerations. A fully detailed treatment is rather complex, but a semiclassical interpretation allows for simple and practical approximate expressions. The main contributions relevant to this analysis are illustrated in Fig.2.2, which shows the spherical average of the molecule as viewed from one of its constituent atoms [59].

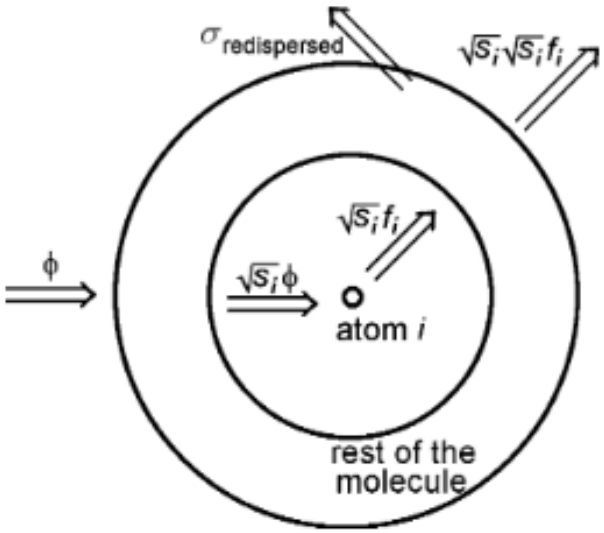

Figure 2.2: This figure presents an analysis of the screening coefficients that influence the wave amplitudes associated with both the direct and redispersed (rescattered) contributions to the observed differential cross section, taken from [59].

It should first be noted that, owing to the average geometrical screening by the rest of the molecule, the incident flux on each atom i is reduced by a factor s_i (or $\sqrt{s_i}$ at the amplitude level). However, the outgoing wave amplitude associated with atom i is not $\sqrt{s_i} f_i$, but rather $s_i f_i$, since the $\sqrt{s_i} f_i$ contribution from atom i is further reduced by an additional $\sqrt{s_i}$ factor due to the screening effect of the remaining atoms in the molecule.

Consequently, two contributions must be taken into account in the molecular elastic cross section: a direct term arising from single scattering events, and a redispersed term originating from the further scattering of the already attenuated $\sqrt{s_i} f_i$ amplitudes:

$$\frac{d\sigma^{\text{molecule}}_{\text{elastic}}}{d\Omega} = \frac{d\sigma^{\text{direct}}_{\text{elastic}}}{d\Omega} + \frac{d\sigma^{\text{redispersed}}_{\text{elastic}}}{d\Omega}\,, \tag{2.42}$$

$$\sigma^{\text{molecule}}_{\text{elastic}} = \sigma^{\text{direct}}_{\text{elastic}} + \sigma^{\text{redispersed}}_{\text{elastic}}\,. \tag{2.43}$$

The different terms in the above expressions can be estimated as follows. For the direct contribution, the standard procedure used in non-screening studies [60, 67, 68] can be applied to expression 2.35, but with $s_i f_i(\theta)$ replacing $f_i(\theta)$, leading to

$$\frac{d\sigma^{\text{direct}}_{\text{elastic}}}{d\Omega} = \sum_i s_i^2 \cdot \frac{d\sigma^{\text{atom }i}_{\text{elastic}}}{d\Omega} + \sum_{i\neq j} \nu s_i s_j f_i(\vec{q}) f_j^*(\vec{q}) \cdot \frac{\sin(qr_{ij})}{qr_{ij}}, \tag{2.44}$$

$$\sigma^{\text{direct}}_{\text{elastic}} = \sum_i s_i^2\, \sigma_i^{\text{elastic}}. \tag{2.45}$$

The redispersed flux can then be estimated as the difference between the total and direct contributions,

$$\sigma^{\text{redispersed}}_{\text{elastic}} = \sum_i s_i(1-s_i)\, \sigma_i^{\text{elastic}}. \tag{2.46}$$

While the exact angular distribution of this term is difficult to obtain, two limiting cases provide reasonable estimates: (i) for large deviations, directionality is lost and an isotropic distribution can be assumed,

$$\left(\frac{d\sigma^{\text{redispersed}}_{\text{elastic}}}{d\Omega}\right)_{\text{iso}} = \frac{\sigma^{\text{redispersed}}_{\text{elastic}}}{4\pi}, \tag{2.47}$$

(ii) in case of strong forward scattering, the same angular dependence as the direct term can be assumed,

$$\left(\frac{d\sigma^{\text{redispersed}}_{\text{elastic}}}{d\Omega}\right)_{\text{same}} = \frac{\sigma^{\text{redispersed}}_{\text{elastic}}}{\sigma^{\text{direct}}_{\text{elastic}}} \frac{d\sigma^{\text{direct}}_{\text{elastic}}}{d\Omega}. \tag{2.48}$$

Since the true distribution lies between these extremes, an interpolation is introduced by weighting the two cases with factors X_{iso} and X_{same} ($X_{\text{iso}} + X_{\text{same}} = 1$):

$$\frac{d\sigma^{\text{molecule}}_{\text{elastic}}}{d\Omega} \approx X_{\text{iso}} \frac{\sigma^{\text{redispersed}}_{\text{elastic}}}{4\pi} + \left[1 + X_{\text{same}} \frac{\sigma^{\text{redispersed}}_{\text{elastic}}}{\sigma^{\text{direct}}_{\text{elastic}}}\right] \frac{d\sigma^{\text{direct}}_{\text{elastic}}}{d\Omega}. \tag{2.49}$$

A simple estimate for X_{iso} and X_{same} can be obtained by assuming that electrons deviating by more than 45° belong to the isotropic group, while the rest follow the direct distribution:

$$X_{\text{same}} \approx \frac{\int_0^{45^\circ} \frac{d\sigma^{\text{direct}}_{\text{elastic}}}{d\Omega} \sin\theta\, d\theta}{\int_0^{180^\circ} \frac{d\sigma^{\text{direct}}_{\text{elastic}}}{d\Omega} \sin\theta\, d\theta}, \qquad X_{\text{iso}} = 1 - X_{\text{same}}. \tag{2.50}$$

As seen in Eq.2.44, the direct contribution can be regarded as a screened version of Eq.2.37. The first term of the sum corresponds to the individual atomic contributions reduced by the s_i factors, while the second term accounts for the reduced interference between different atoms in the molecule.

It should be noted that the application of the Additivity Rule (AR)—i.e., neglecting the integrated interference contributions while including them in the differential cross sections—can lead to a discrepancy between Eqs. 2.44 and 2.45. To avoid this inconsistency, an additional

reduction factor ν is introduced, which is applied to the positive values of the interference term $\frac{d\sigma_{\text{interference}}}{d\Omega}$ in order to satisfy the condition

$$\int d\Omega \, \frac{d\sigma_{\text{interference}}}{d\Omega} = 0 \, .$$

However, it has recently been shown that, in order to properly account for multiple-center interactions, the integrated interference contribution $\sigma_{\text{interference}}$ must be included in the calculation of the total cross section. Consequently, the AR approach requires revision. This method, which incorporates interference contributions within the AR procedure, is referred to as AR+I. In line with this, the SCAR method must also be reformulated to include these contributions. This topic will be addressed in the following section.

2.5.4 Screening Corrections to the Interference Contributions

It should be noted that previous studies on interference terms in multiple-scattering calculations have been rather limited, typically restricted to first-order corrections in double or triple scattering [60, 78, 81] or to small molecular systems [79]. These works suggest that multiple scattering generally reduces both the integrated interference contribution and the differential cross section at small scattering angles. However, due to their limitations, no general conclusions can be drawn, emphasizing the need for a consistent incorporation of interference terms within the SCAR and AR+I frameworks.

The analysis of interference contributions in multi-center potentials remains challenging, particularly at low incident energies. Nonetheless, systematic studies across multiple geometries, interatomic distances, and energies reveal consistent trends [62]:

- Interference contributions obtained via the AR method in [62] are well applicable when interatomic distances are large compared to both the geometric cross-section radius and the projectile wavelength.
- Otherwise, these contributions must be reduced or even neglected.

In order to quantitatively define this criterion, the interatomic distance r_{ij} for each pair of atoms i and j was compared with the length parameters defined as

$$\rho_{ij} = \max\left(\sqrt{\frac{\sigma_i}{\pi}}, \sqrt{\frac{\sigma_j}{\pi}}, \frac{1}{k}\right), \tag{2.51}$$

It should be noted that the expression $\sqrt{\sigma/\pi}$ corresponds to the radius of a circle with area σ, so the condition

$$r_{ij} = \max\left(\sqrt{\frac{\sigma_i}{\pi}}, \sqrt{\frac{\sigma_j}{\pi}}\right) \tag{2.52}$$

represents the situation in which the geometric areas of the two circles begin to overlap — specifically, the center of the smaller circle reaches the edge of the larger one.

Therefore, for any atom pair satisfying the condition $k\, r_{ij} > 1 \quad \text{and} \quad r_{ij} > \beta_{ij}$, the geometric overlap of the cross sections can be considered moderate, and the corresponding interference effects can be attenuated.

A simple procedure can then be proposed by introducing a factor ν_{ij}, which smoothly attenuates the interference terms according to whether $r_{ij} > \beta_{ij}$ or $r_{ij} < \beta_{ij}$. For practical purposes, ν_{ij} can be defined as

$$\nu_{ij} = \frac{r_{ij}^2}{r_{ij}^2 + \rho_{ij}^2}, \tag{2.53}$$

which provides the expected functional behavior. This procedure, referred to as the **IAM-SCAR+I treatment** [62], essentially differs from the previous SCAR method only by the replacement of expressions 2.39 and 2.45 with the corresponding screened forms given below.

$$\sigma_{\text{elastic}}^{\text{molecule}} = \sum_{\text{atoms}} s_i \cdot \sigma_{\text{elastic}}^{\text{atom } i} + \sigma_{\text{interference}} \tag{2.54}$$

$$\sigma_{\text{elastic}}^{\text{direct}} = \sum_{\text{atoms}} s_i^2 \cdot \sigma_{\text{elastic}}^{\text{atom } i} + \sigma_{\text{interference}} \tag{2.55}$$

where the interference contribution is now defined as

$$\sigma_{\text{interference}} = \int \left(\sum_{i \neq j} \nu_{ij}\, s_i s_j\, f_i(\vec{q}) f_j^*(\vec{q})\, \frac{\sin(q r_{ij})}{q r_{ij}} \right) d\Omega. \tag{2.56}$$

with s_i being the screening coefficients introduced in Eq.2.39. This simple procedure provides a significant improvement of both differential and integral scattering cross sections at intermediate energies, while retaining the high-energy efficiency of the IAM method.

2.5.5 Polar Molecules

It should be emphasized that the IAM-SCAR procedure does not include vibrational or rotational excitations. For polar molecules, however, additional dipole-driven rotational excitation cross sections can be evaluated following the approach of Jain [82]. In this method, the differential and integral cross sections for rotational transitions of a free electric dipole are calculated within the first Born approximation (FBA). These contributions can then be incorporated into the IAM-SCAR results in an incoherent manner, simply by adding them as an independent channel. Since rotational excitation energies are typically only a few meV, the Born approximation is valid provided that the incident electron energy exceeds about 20 eV. Under these conditions, rotational excitation cross sections $J \rightarrow J'$ are obtained by weighting the population of the Jth rotational state at 300 K and estimating the mean excitation energy from the corresponding rotational constants [75].

When the permanent dipole moment of the molecule is sufficiently large (as in the case of anestetic molecules), the first Born approximation (FBA) becomes unreliable at medium and large scattering angles. To address this limitation, a correction following the approach of Dickinson [83] was introduced, which significantly improves the description of electron scattering cross sections for strongly polar molecules. In this procedure, the differential cross section retains the FBA expression at small angles, while a first-order corrective term is applied at larger angles:

$$\frac{d\sigma^B}{d\Omega} \approx \frac{D^2}{6E_i \sin^2(\theta/2)} \quad \text{for} \quad \theta < \theta_c, \tag{2.57}$$

$$\frac{d\sigma^{Dck}}{d\Omega} \approx \frac{\pi D}{64E_i \sin^3(\theta/2)} \quad \text{for} \quad \theta > \theta_c, \tag{2.58}$$

where D is the molecular dipole moment and E_i the projectile energy. For dipole moments larger than $D = 0.75$ D, the two expressions merge smoothly at the critical angle θ_c, defined as their intersection point [75].

The IAM-SCAR+I calculations in this study were conducted by the research group led by Professor Gustavo García at CSIC (Consejo Superior de Investigaciones Científicas), Madrid, Spain.

Chapter 3

Experimental Setup and Methodology

A clear description of the experimental setup and methodology is essential for understanding the measurements presented in this work and for assessing the reliability of the obtained results. Since elastic electron scattering experiments are highly sensitive to the stability and precision of the apparatus, careful attention must be given to both the instrumental design and the applied measurement procedures.

In this chapter, the general principles of electron spectrometers are first introduced, with emphasis on the detection of scattered electrons and the determination of differential cross sections. The UGRA apparatus, which has been specifically designed and constructed at the Laboratory for Atomic Collision Processes of the Institute of Physics in Belgrade, represents the core experimental system used in this work. It is an electron spectrometer consisting of three main components: an electron gun, a molecular (or atomic) gas source, and an analyzer system with a detector for charged particles. Together, these elements enable precise studies of electron–molecule interactions under well-controlled conditions. The chapter provides a detailed description of the vacuum chamber, electron optics, analyzer lenses, and the double cylindrical mirror analyzer (DCMA), as well as the detection system based on a channeltron. The methodology for measuring relative and absolute differential cross sections is then outlined, including the application of the relative flow method for absolute normalization. In addition, procedures for extrapolating integral and momentum transfer cross sections are presented. Finally, the evaluation of measurement uncertainties is discussed, ensuring a transparent and comprehensive account of the experimental accuracy.

3.1 Fundamentals of the Electron Spectrometers

Figure 3.1 presents a generalized schematic of the apparatus employed in electron spectroscopy experiments. These experiments play a central role in probing atomic and molecular structures and interactions, as well as in validating theoretical models that describe such phenomena.

The main components of the apparatus include a source of nearly monoenergetic electrons, a collision chamber containing a dilute gas, an energy analyzer for detecting scattered electrons or stable negative ion fragments, and a collector for the unscattered electron beam. Since negative ions can also originate from the collision region and typically follow similar trajectories to electrons in electrostatic systems, a mass-selective device with sufficient resolution to distinguish ions from electrons is often desirable, although it is not always implemented in practice. In most cases, the absence of a mass filter does not significantly affect the results, as the cross sections for dissociative attachment are generally much smaller than those for inelastic electron scattering [40].

Electrons can be generated by several methods, including thermionic emission, photoelectron emission, secondary electron emission, and field emission. In most cases, they are produced

via thermionic emission from a heated filament. The electrons then pass through a monochromator, which selects a narrow portion from the initially broad energy distribution. Upon exiting the monochromator with a fixed energy, the electrons are accelerated or decelerated to the desired collision energy using a voltage V_M before entering the interaction chamber. Scattered electrons at a given scattering angle θ are first slowed down or accelerated to an energy suitable for the analyzer. In dissociative attachment experiments, stable negative ion fragments are collected, energy-analyzed, and, if necessary, passed through a mass filter prior to detection.

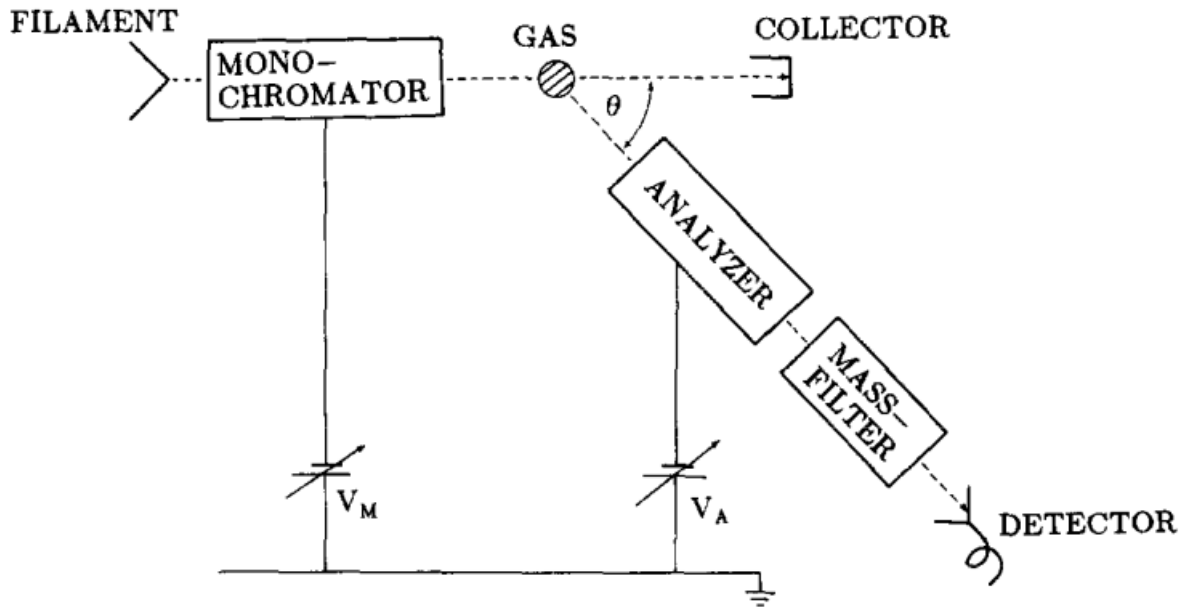

Figure 3.1: Schematic representation of the general experimental setup for electron-impact spectroscopy. Electrons emitted from the filament first pass through the monochromator at low fixed energy, after which they are accelerated (or decelerated) to the desired collision energy E_{in} by applying a variable voltage. The scattered electrons (or stable negative ion fragments) are collected at an angle θ, slowed down to match the pass energy of the analyzer, subjected to energy (and, if applicable, mass) analysis, and subsequently counted. Taken from [40].

Various implementations of the general setup depicted in Figure 3.1 have been developed in different laboratories. These designs primarily differ in the type of energy-dispersing elements employed in the monochromator and analyzer (e.g., cylindrical or hemispherical electrostatic, trochoidal, or Wien-filter), the nature of the target (stationary gas in a collision chamber versus a molecular beam), the type of mass filter used (such as sector magnets, quadrupoles, or time-of-flight devices), and other technical details. A notable class of instruments, the electron transmission spectrometers, operates without an energy analyzer entirely.

3.1.1 Spectra

With the general setup illustrated in Figure 3.1, four distinct types of spectra can, in principle, be obtained. However, most practical instruments are specialized and typically cannot record all four types.

- **Electron Transmission Spectrum (ETS)**

  In electron transmission experiments, the analyzer is omitted, and the total transmitted electron current, I_t, arriving at the collector is measured. The decrease in the electron

current caused by the presence of gas allows the approximate determination of the total scattering cross section as a function of the incident electron energy, although this is limited by the incomplete rejection of scattered electrons. The formation of a temporary negative ion often results in relatively narrow features in the total cross section, making electron transmission spectroscopy a useful tool for probing the electronic states of negative ions. To enhance the visibility of weak variations in the cross section due to resonances, ETS data are often presented in derivative form, showing the derivative of the transmitted current, dI_t/dE_{in}, as a function of the incident electron energy, E_{in}.

- **Energy-Loss Spectrum (ELS)** In energy-loss experiments, the scattered electron current is measured as a function of the energy loss, ΔE. This can be achieved either by keeping the analyzer voltage, V_A (and hence the residual electron energy, E_r), fixed while scanning the incident voltage, V_i (incident energy E_{in}), or vice versa. The former approach is often preferred, as the excitation dynamics depend on the excess energy above the excitation threshold, and spectra recorded at constant E_r exhibit a more uniform behavior across the entire energy-loss range.

  Peaks in the energy-loss spectrum indicate that the target molecule can absorb a specific amount of energy and possesses a corresponding excited state, either vibrational or electronic. Therefore, energy-loss spectroscopy provides direct information about the excited states of the neutral target molecule.

  Electron energy-loss spectroscopy is a valuable complement to optical spectroscopic methods, as it allows the observation of transitions that are forbidden under electric dipole or spin selection rules. This technique has enabled the identification of numerous previously unobserved electronic states in various molecules [84–90].

- **Energy-Dependence Spectrum (EDS)** In energy-dependence experiments, the probability of exciting a specific state of the neutral molecule is measured as a function of the incident electron energy, E_{in}. This is accomplished by simultaneously scanning both E_{in} and E_r, thereby maintaining a constant energy loss, ΔE, corresponding to the selected excitation feature. The presence of a temporary negative ion state often leads to an enhancement or variation in the excitation probability, meaning that the energy-dependence spectrum provides valuable insight into the electronic states of negative ions.

  Two important subclasses of this technique are the energy dependence of vibrational excitation and the energy dependence of electronic excitation. The former is particularly effective for detecting very broad shape resonances, since the cross sections for non-resonant vibrational excitation are typically quite small; as a result, the method is not significantly affected by the background signal that complicates ETS. Nevertheless, strong excitation of infrared-active vibrations can also occur in the absence of a resonance. The energy dependence of electronic excitation, on the other hand, is especially useful for identifying core-excited resonances.

- **Dissociative Attachment Spectrum (DAS)** In dissociative attachment experiments, a mass filter is placed in series with the analyzer and adjusted to transmit only a specific stable fragment anion, such as O^-, H^-, Cl^-, CH_3^-, or C_2H^-, while the yield of this fragment is measured as a function of the incident electron energy. In many cases, it is also desirable to record the kinetic energy distribution of the fragment ions, as this provides valuable information for elucidating the underlying dissociation mechanisms.

  Typically, the formation of stable fragment anions occurs exclusively via the dissociation of a temporary molecular anion; consequently, the dissociative attachment spectrum carries direct information on the electronic states of the negative ion.

Electron scattering experiments represent a fundamental tool in modern atomic and molecular physics, as they provide direct information on interaction dynamics and allow stringent tests of theoretical models. Among the available experimental approaches, the crossed-beam technique has proven to be particularly powerful due to its ability to deliver high resolution in both angular and energy distributions of the scattered particles.

In electron spectroscopy experiments, the count rate of scattered particles (most commonly electrons) is monitored as a function of variable parameters such as incident energy, residual energy, scattering angle, and energy loss. The resulting dependencies are directly proportional to the differential cross sections of the process under investigation, provided that the geometrical factor and the transmission of the system are properly taken into account. In such experiments, molecular beams are most frequently used as the target, offering several advantages over a static gas atmosphere. These advantages primarily concern the well-defined preparation of atoms or molecules for collision and the favorable shape of the interaction volume.

The experimental results presented in this work were obtained using the UGRA apparatus (an acronym for *UGaona RAspodela*, i.e., Angular Distribution), located at the Laboratory for Atomic Collision Processes, Institute of Physics, Zemun. The applied technique was the crossed-beam method, in which an electron beam intersects a molecular beam at right angles, with the scattered particles subsequently analyzed in terms of both angle and energy.

3.2 General Description of the UGRA Apparatus

The UGRA apparatus is an electron spectrometer whose principal components include an electron beam source (electron gun), a molecular (or atomic) beam source, and an analyzer system equipped with a detector for charged particles. Together, these elements enable the precise study of electron–molecule (or electron–atom) interactions under well-controlled conditions. A photograph of the apparatus from the outside is shown in Figure 3.1, while Figure 3.3 presents the interior of the vacuum chamber. A schematic diagram of the experimental setup is given in Figure 3.4.

Figure 3.2: Picture of the UGRA Apparatus.

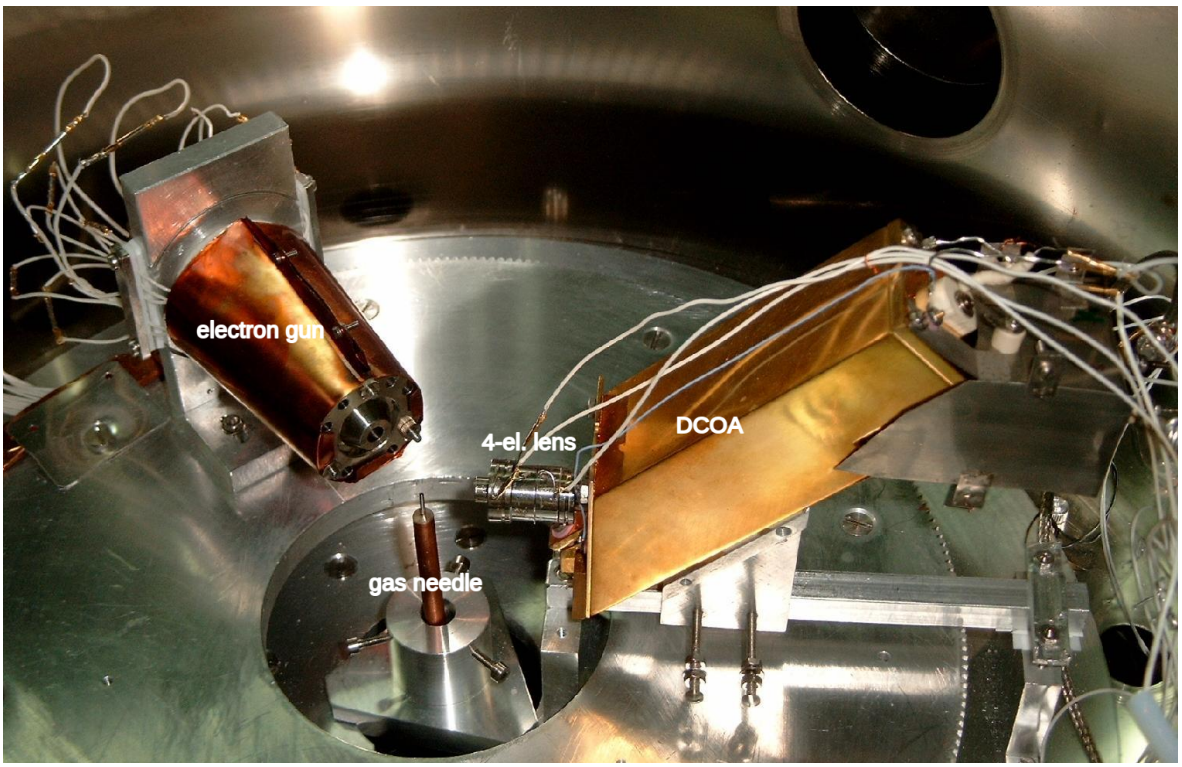

Figure 3.3: Photograph of the interior of the UGRA apparatus, showing the main components housed within the stainless-steel vacuum chamber.

The target gas is formed by a stainless-steel gas needle, with a length of $l = 40$ mm and a diameter of $d = 0.5$ mm, positioned vertically from above into the scattering region. The needle operates in the effusive regime, which ensures higher particle density and improved beam collimation.

According to Lucas [91], the properties of the atomic beam can be predicted and optimized. The optimum atomic beam is obtained when $I(0)^2/(NH^2)$ is maximized, where $I(0)$ is the axial intensity, N the throughput, and H the beam halfwidth. It has been shown that $I(0)^2/(NH^2) \propto l^2/d$. Thus, the optimum beam is achieved when the ratio of the square of the tube length to its diameter is maximum, which in our case corresponds to 3200. These expressions are valid for tubes where $\gamma = d/l < 10$ and for sufficiently low gas pressures such that the particle mean free path satisfies $\lambda \geq d$. In our experimental setup, $\gamma = 80$ and $\lambda \approx d$.

The incident electron beam is generated by thermionic emission from a hairpin-type cathode operated at a heating current of about 2–2.5 A. The electron gun produces a well-collimated, nearly monoenergetic beam that intersects the molecular beam at right angles in the center of the interaction region. The gun is mounted on a rotatable platform, enabling adjustment of the scattering angle over a range of approximately –40° to +130° with respect to the optical axis of the analyzer. The angular resolution of the apparatus is about ±2°, as estimated from elastic scattering on argon [92]. For this purpose, calibration measurements are routinely performed by locating the characteristic deep minimum in the elastic differential cross section of argon at well-known incident electron energies and comparing with published reference data [93–96].

Electrons scattered under a given angle are energy-selected using a double cylindrical mirror analyzer (DCMA). Before entering the analyzer, the electrons were decelerated (or accelerated) and focused by a four-element cylindrical lens system. After energy analysis, they are refocused by a three-element lens into a single-channel electron multiplier (channeltron), which operates in the pulse-counting mode. Each detected electron produces a pulse that is processed through a sequence of electronic modules (amplification, discrimination, and filtering) before being converted into a standard TTL signal.

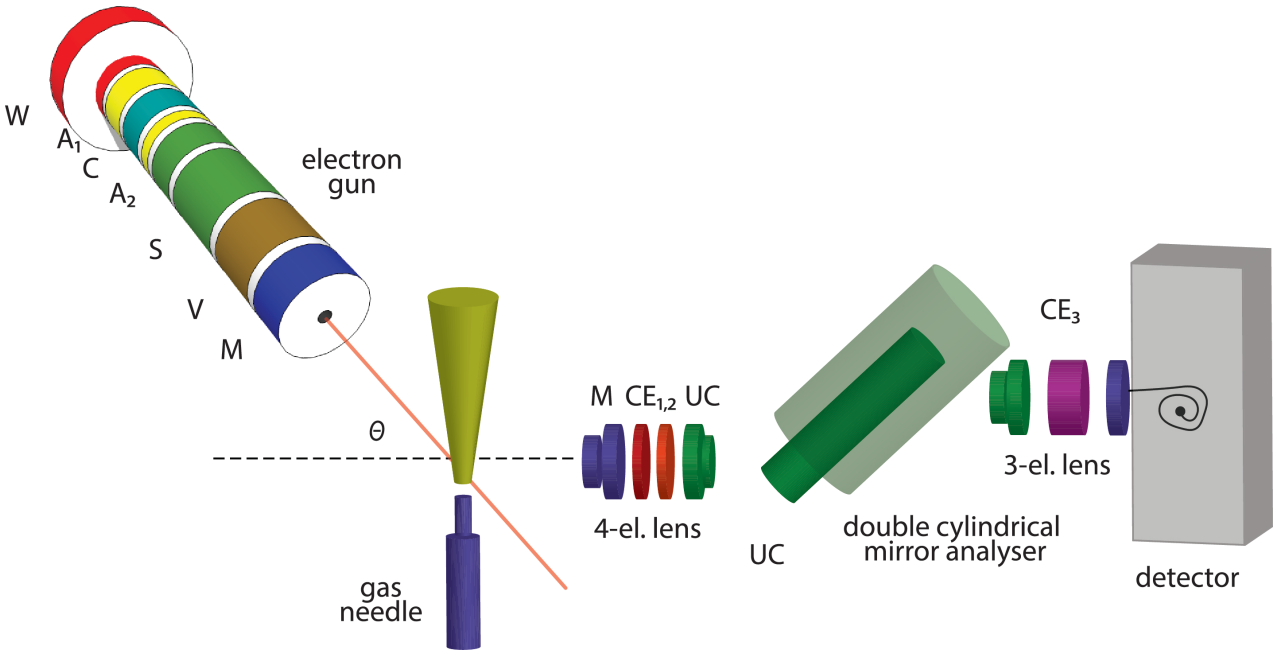

Figure 3.4: Schematic representation of the UGRA experimental setup, consisting of an electron gun, a molecular (or atomic) beam source introduced through a gas needle, and an analyzer system with a detector for charged particles [13].

All elements of the spectrometer are enclosed in a stainless-steel cylindrical vacuum chamber equipped with two concentric μ-metal shields, which suppress the influence of the Earth's magnetic field and other external perturbations. The chamber is evacuated by a turbomolecular pump backed by a rotary pump, achieving a base pressure on the order of 10^{-7} mbar. Typical operating pressures during measurements are on the order of 10^{-6} mbar, under which multiple scattering remains negligible. Pressure inside the chamber is monitored by an ionization gauge mounted at its base.

Data acquisition and experimental control are carried out using an I/O interface card operated by a dedicated C++ program (`AQUGRA`), developed in our laboratory. The program records the electron counts as a function of incident energy and scattering angle, while simultaneously storing key experimental parameters such as chamber pressure, electrode voltages, electron gun settings, and analyzer configuration for each experimental point.

3.2.1 Vacuum Chamber

All components of the experimental setup are enclosed within a cylindrical stainless-steel vacuum chamber, 690 mm in diameter and 550 mm in height, allowing the achievement of ultra-high vacuum conditions. The interior of the chamber is shown in Figure 3.3. Inside, two concentric aluminum plates are mounted: the larger plate is fixed to the chamber base, while the smaller plate can rotate above it. Both plates have central circular openings through which the gas needle passes.

The chamber is surrounded by two concentric μ-metal shields to suppress the influence of the Earth's magnetic field and other external magnetic disturbances down to the order of 10^{-7} T [92]. Vacuum is maintained using a turbomolecular pump (TMP), which operates by transferring momentum from the rotating elements of the pump to the gas molecules. The pump consists of a series of angled rotor and stator disks: the rotor disks rotate while every second disk remains stationary as a stator. The rotor blades are oriented such that gas molecules acquire significant velocity in the pump outlet direction after collisions with the blades, while

the stator blades decelerate and compress the gas before it enters the next rotor-stator stage.

For proper TMP operation, a pre-vacuum on the order of 10^{-2} mbar is required, which is provided by a rotary backing pump connected in series with the TMP. Chamber pressure is monitored using an ionization gauge mounted at the chamber base, which measures the ion current produced by electron collisions with gas molecules. The lowest pressure achieved in the system was $3 \cdot 10^{-7}$ mbar. During our experiments, the base pressure was approximately $6 \cdot 10^{-7}$ mbar, and the working pressure was about $4 - 7 \cdot 10^{-6}$ mbar.

3.2.2 Electron Gun

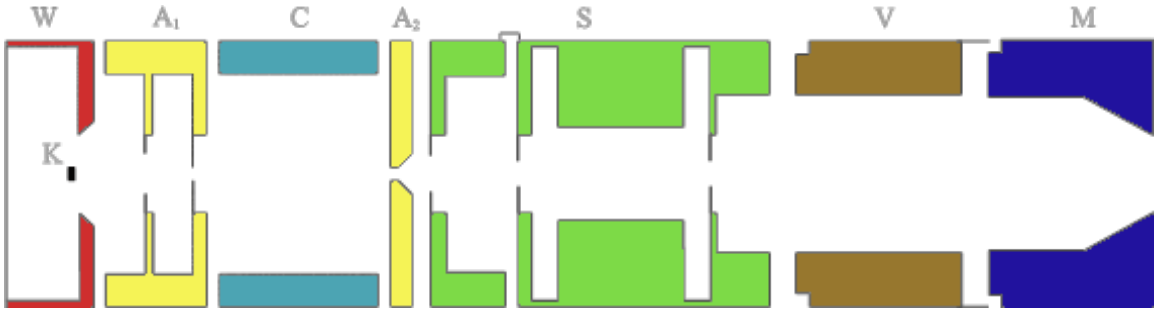

Figure 3.5: Detailed schematic of the electron gun, generated using the SIMION software, adapted from [97].

The electron gun used in the present experiments, shown schematically in Figure 3.5, was designed and built in the Laboratory for Atomic Collisions at the Institute of Physics. It is capable of producing an electron beam current of a few microamperes within the energy range of 40–300 eV. Primary electrons are generated via thermionic emission from a tungsten-thorium (W–Th) hairpin cathode, with a current between 2.1 and 2.3 A. The cathode current must be gradually increased at the start of operation to prevent burnout, initially in 0.1 A steps every 5 minutes up to 1 A, and then every 2 minutes until reaching the working current.

The electron gun consists of a system of cylindrical electrodes, which can be divided into two functional groups:

- The extraction and collimation section, comprising electrodes W, A1, C, and A2.
- The focusing section, including electrodes A2, S, V, and M, which direct the beam into the interaction region.

Fine adjustment of the beam trajectory is accomplished using four deflector electrodes located within electrode S. The electron energy is determined by the potential difference between the cathode (center of the tungsten filament) and the last electrode M, which is held at ground potential. All other electrodes "float" relative to the cathode. Since the experimental setup does not include a monochromator, the electron energy spread is governed by the initial thermal distribution of electrons and is approximately 0.5 eV in the energy-loss mode.

The gun assembly is enclosed in a grounded copper shield and mounted on a movable support, allowing rotation around the gas needle that produces the target molecular or atomic beam. The interaction volume is defined by the overlap of the electron and target beams and the acceptance angle of the analyzer. Due to the relatively wide spatial profile of the electron beam, the interaction volume remains essentially independent of the rotation angle once the system is properly aligned and the beam is well-focused.

The primary beam current, measured before the target gas is introduced, is monitored with a Faraday cup. Typical currents were in the range of 100–300 nA at a cathode current

of 2.22–2.3 A, depending on the electron energy. The Faraday cup, placed at an angle of 46.3° relative to the electron beam axis, allows precise calibration of the beam alignment and assessment of the angular distribution. During measurements, the beam current and other relevant experimental parameters—including electrode voltages, electron beam energy, and rotation angle—are continuously recorded using a digital ammeter and data acquisition system.

Figure 3.6 presents the primary electron beam current as a function of the x-coordinate of the Faraday cup. Both the experimental data and the corresponding SIMION simulation are shown. Measurements were performed at an incident electron energy of 100 eV, with the Faraday cup positioned at 43.1° relative to the analyzer system. During these measurements, the electron gun electrode voltages were set to W = −12.9 V, A = 147.9 V, C = −34.1 V, S = 103.8 V, V_1 = 14.5 V, D_x = 5.7 V, and D_y = −1.7 V, while the cathode current was 2.23 A. The D_x and D_y electrodes, located within the S electrode, were used to fine-tune the beam trajectory perpendicular to the electron gun axis.

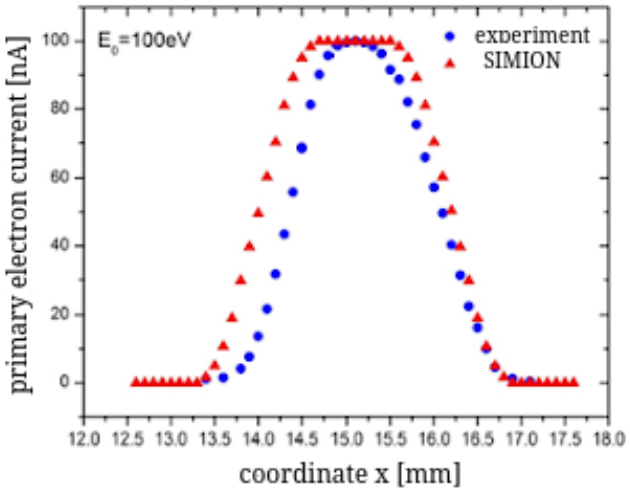

Figure 3.6: Dependence of the primary electron beam current on the x-coordinate of the Faraday cup. Experimental data are compared with SIMION simulations. Measurements were performed at an incident electron energy of 100 eV, with the Faraday cup positioned at 43.1° relative to the analyzer system.

3.2.3 Analyzer System

Scattered electrons emerging from the interaction region at a given angle θ first pass through an analyzer lens. In the UGRA apparatus, this function is performed by a four-electrode cylindrical lens, whose schematic is shown in Figure 3.7.

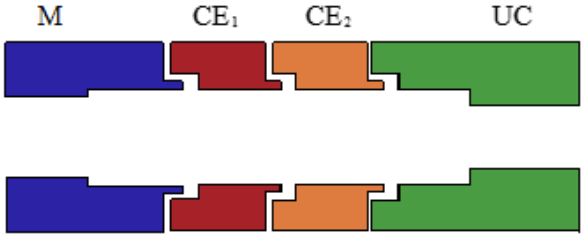

Figure 3.7: Schematic of the four-electrode cylindrical lens used in the UGRA apparatus. Adapted from [98]

The first electrode (M) is always held at zero potential relative to the interaction region, and its length is sufficient to prevent penetration of electric fields into the interaction volume. The last electrode (UC) is connected to the inner cylinder of the analyzer. The voltages on the central electrodes (CE1 and CE2) are defined relative to UC.

The analyzer lens in the UGRA apparatus serves multiple purposes:

- It collects the charged particles emerging from the interaction region and directs them toward the entrance of the energy analyzer, simultaneously focusing the beam for precise energy analysis.
- It defines the particle energy immediately at the analyzer entrance, allowing energy scanning of the investigated electrons while maintaining a fixed transmission energy of the analyzer.
- Since there are no entrance apertures before the analyzer lens to define the acceptance angle, the potential distribution along the lens also affects the angular resolution of the measurements.

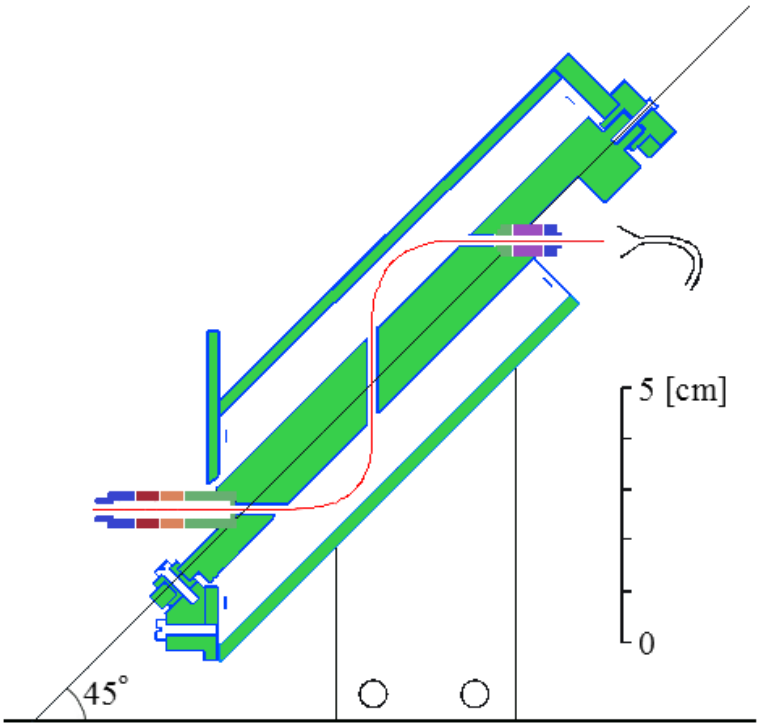

Figure 3.8: Schematic representation of the analyzer system. The energy analysis is performed by a double cylindrical mirror analyzer (DCMA). At the entrance of the analyzer, a four–electrode cylindrical electron lens is employed, while at the exit a three–electrode cylindrical lens is used for focusing and guiding the transmitted electrons. Adapted from [98].

The energy analyzer employed in the UGRA apparatus is a double cylindrical mirror analyzer (DCMA). This device essentially consists of two cylindrical mirror analyzers (CMA) arranged in series, a configuration that combines favorable optical properties with relatively simple construction. A schematic cross section of the DCMA used in our experiments is shown in Figure 3.8. The radii of the inner and outer cylinders are $R_U = 6$ mm and $R_V = 12$ mm, held at potentials UC and VC, respectively. Charged particles enter the analyzer under an angle of $\theta = 45°$ with respect to the cylinder axis.

The pass energy E_p of the electrons transmitted through the analyzer is determined by the potential difference between the two cylinders and the construction parameters of the device. In general, the relation is linear and can be expressed as

$$E_p = k\,\Delta V_{DCMA},$$

where k is a constant defined by the geometry of the analyzer. For the DCMA implemented in the UGRA apparatus, experimental characterization has shown that $k \approx 1.32$. In our measurements, the potential difference ΔV_{DCMA} was typically fixed at 23 V, resulting in a pass energy of approximately 30.2 eV. For instance, to select electrons of 100 eV, they must be retarded to the pass energy by applying $UCM \approx -69.8$ V at the final electrode of the entrance lens.

The energy resolution of the analyzer is typically 3%–4% of the pass energy E_p. Thus, in order to achieve high energy resolution on the order of a few tens of meV, one would operate at low pass energies of only a few eV. However, in the present work the analyzer was predominantly used in the high-pass-energy regime, which provides a stronger signal and constant transmission at the expense of energy resolution. This trade-off is particularly important for measurements of differential cross sections as a function of incident electron energy, where signal intensity and stability are of primary concern.

The complete analyzer system in the UGRA setup is complemented by two lens assemblies: a four-electrode cylindrical lens at the entrance, which directs and focuses electrons into the DCMA, and a three-electrode cylindrical lens at the exit, which collects and guides transmitted electrons toward the detector.

3.2.4 Electron Detection System

The detection of scattered electrons in the UGRA apparatus is performed using a channeltron, i.e., a single-channel electron multiplier. This device operates by applying a high voltage across its length, with the configuration depending on the type of particles being detected. For electron detection, the channeltron entrance (the "nose") is grounded, while a large positive voltage is applied to its opposite end. In contrast, when detecting positive ions, a high negative voltage is applied at the entrance in order to accelerate the ions toward the channeltron, while the exit is grounded.

Upon striking the inner wall of the channeltron, each incident particle (electron or ion) produces secondary electrons. These secondary electrons are subsequently accelerated along the length of the channeltron, where they impact the walls again, generating additional secondary electrons. Since the potential difference is positive along the entire length of the tube, this avalanche multiplication process continues until a large number of electrons is produced, with a typical gain of the order of 10^8. The resulting pulse is transmitted through an RC filter, preamplifier, and amplifier before reaching a fast discriminator. Finally, the analog signal is converted into a logical TTL signal, which is then directed to a multichannel analyzer, a counter, and a ratemeter.

One of the intrinsic limitations of channeltrons is the saturation effect, which occurs when the density of space charge inside the detector becomes sufficiently large to repel secondary electrons before they acquire enough energy for further collisions. Moreover, the operational characteristics of a channeltron gradually change over time, due to modifications of the high-resistance inner surface. This degradation process can be accelerated by interactions with reactive molecules [99]. A practical manifestation of this aging effect is the progressive increase of the operating voltage: during extended periods of measurement, the required working voltage of the channeltron typically shifts from approximately 2.2 kV up to 2.8 kV.

The acquisition of experimental data is carried out by a Tracor Northern TN-1705 multichannel analyzer, which generates a variable voltage linearly dependent on the channel number, so that signals are accumulated over a predefined dwell time per channel. In addition, a National Instruments multifunctional I/O card is employed for computer control and data transfer, operating under the dedicated C++ software package `AQUGRA` [92, 97, 99].

3.3 Types of Measurements and Methods

The UGRA apparatus allows for the following types of measurements:

- **Energy Distribution Spectra of Positive Ions** When determining these spectra, the incident energy E_0, scattering angle θ, and pass energy E_p are kept fixed. The intensity of the positive ion current I is recorded as a function of the accelerating voltage UCM applied to the last electrode of the entrance electron lens, i.e., $I = f(UCM)$. The accelerating voltage UCM is stepwise varied (scanned), thereby transferring the additional energy required for the efficient detection of ions. In this way, the resulting spectra provide the dependence of the positive ion current on the kinetic energy of the ions after the collision, $I = f(E_{\text{kin}})$, where lower kinetic energies correspond to higher values of the accelerating voltage UCM.

- **Electron Energy-Loss Spectra** These measurements provide the dependence of the scattered electron intensity on the energy lost during the collision. During the acquisition of such spectra, the pass energy E_p, incident electron energy E_0, and scattering angle θ are kept constant. Similar to the procedure for recording positive ion kinetic energy distribution spectra, the electron count rate is collected as a function of the potential applied to the last electrode of the entrance analyzer lens, UCM, which in this case acts as a retarding potential.

- **Excitation Functions** These measurements provide the dependence of the intensity of a given process on the incident electron energy E_0. During the acquisition, the scattering angle θ and the pass energy E_p are kept constant, while the measured quantity is the signal intensity I as a function of E_0.

- **Relative Differential Cross Sections (rDCSs)** The relative differential cross sections (rDCSs) are determined by measuring the count rate of scattered electrons at the maximum of the elastic peak in the electron energy-loss spectrum. Two types of rDCS measurements can be performed. In the first, the count rate is recorded as a function of the scattering angle θ, while keeping the incident electron energy E_0, the pass energy E_p, and the potential UCM fixed. In the second, the count rate is measured as a function of the incident electron energy E_0, with fixed parameters θ, E_p, and UCM. In this work, the measurements of primary interest are those performed as a function of the scattering angle θ.

- **Absolute Differential Cross Sections (DCSs)** The absolute differential cross sections (DCSs) are determined using the relative flow method [100–103], in which the signals of elastically scattered electrons from the target molecule are compared with those from a reference gas under identical experimental conditions. In this procedure, both the incident electron energy E_0 and the scattering angle θ are kept fixed. The data obtained in this way are used to normalize the relative cross sections to an absolute scale.

In the present work, the last two types of measurements—relative differential cross sections and absolute differential cross sections—are of primary interest.

3.3.1 Measurement of Relative Differential Cross Sections for Elastic Electron Scattering

Crossed-beam experiments represent a powerful method for investigating particle interactions and for determining differential cross sections. In such experiments, the cross section is related to the measured intensity of the scattered signal through a rather complex expression that includes both geometrical and instrumental functions [104]. The cross section, averaged over the angular and energy resolution of the apparatus, can be expressed as the product of the measured signal intensity and a proportionality function.

In the case of an idealized scattering geometry and a perfect apparatus, this proportionality function would be constant, i.e., independent of the scattering angle and the electron energy. However, in real experiments, several factors come into play: an extended interaction volume, a non-localized and non-uniform target density, as well as distributions of the incident beam flux. As a consequence, the proportionality function becomes dependent on the scattering angle. In addition, electron optics, and thus the detector efficiency, generally depend on the electron energy.

Therefore, the proportionality function applied to the measured intensity of scattered electrons, in order to derive the cross section, is a function of both the scattering angle and the electron energy. Although, in principle, this function could be used to obtain absolute cross sections, in practice it is far more reliable to generate only relative cross sections and perform the normalization to an absolute scale by other means.

The relationship between the intensity of scattered electrons and the differential cross section can be obtained by assuming that the electron and molecular beams originate from distant point-like sources, characterized by a small divergence of the electron beam and a significant divergence of the molecular beam, respectively. Both beams are considered to be spherically symmetric.

Furthermore, it is assumed that the angular response function of the detector is independent of the scattering angle, being equal to unity inside the scattering volume and zero outside, and that it is independent of the energy response function. The spatial and energy distribution functions of the primary electron beam are taken as independent, while the target molecules are assumed to be randomly oriented, making the scattering process independent of the azimuthal angle φ.

Under these assumptions, for elastic electron scattering one obtains:

$$I(E_0, \theta) = DCS(E_0, \theta)\, F(E_0)\, V_{\text{eff}}, \tag{3.1}$$

where:

- $I(E_0, \theta)$ – measured intensity of elastically scattered electrons of initial energy E_0 at scattering angle θ,
- $DCS(E_0, \theta)$ – differential cross section,
- $F(E_0)$ – dimensionless function representing the detector response,
- V_{eff} – effective scattering volume, defined as:

$$V_{\text{eff}} = \int \rho(r)\, f(r)\, \Delta\Omega(r)\, G[\theta(r)]\, dr, \tag{3.2}$$

with:

- $\rho(r)$ – spatial distribution density of target molecules,

- $f(r)$ – spatial distribution function of incident electrons,
- $\Delta\Omega(r)$ – solid angle of the detector at position r,
- $G[\theta(r)]dr$ – angular dependence of the differential cross section.

The integration is performed over the scattering volume, which is defined by the intersection of the incident electron beam with the molecular target beam within the acceptance angle of the detector [104].

From Eq. (3.1), the expression for the differential cross section as a function of the scattering angle at a given incident energy E_0 can be written as:

$$DCS_{E_0}(\theta) = \frac{I_{E_0}(\theta)}{F(E_0)\, V_{\text{eff}}}, \tag{3.3}$$

In the experiment, the intensity $I_{E_0}(\theta)$ is directly measured, while the determination of $DCS_{E_0}(\theta)$ (up to the constant $1/F(E_0)$) requires knowledge of the effective scattering volume $V_{\text{eff}}(\theta)$, or alternatively, that this volume be made constant across the angular range.

One common method of obtaining the correction for the effective scattering volume, particularly important at small scattering angles, is by comparing the measured differential cross sections for a reference target (e.g., Ar) under identical experimental conditions with the already established reference data [93, 96]. In addition, the impact of correction factors can be reduced by increasing the acceptance angle of the detector.

In the present work, the scattering volume within the "field of view" of the detector was adjusted such that $V_{\text{eff}}(\theta)$ remained effectively constant across most of the angular range. The validity of this procedure was experimentally verified by comparing our results for Ar with the previously reported measurements [93, 96]. Corrections were applied only when necessary, i.e., for small scattering angles ($\theta < 40°$).

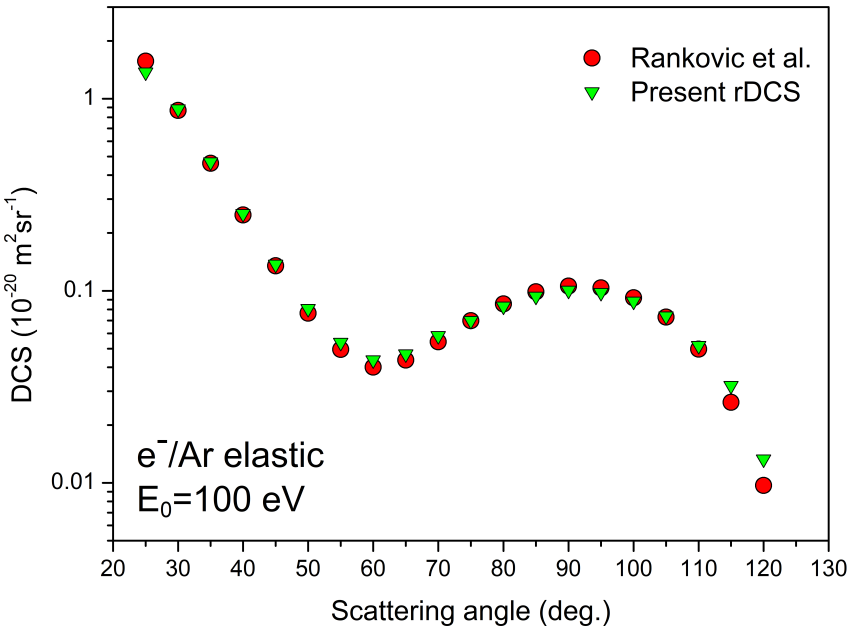

Figure 3.9: Correction curve obtained by comparing the measured relative differential cross sections for Ar at 100 eV with previously published data [96]. The normalization to the reference data provides the correction factors at small scattering angles.

On Fig. 3.9, the correction curve is shown, where our measured relative cross sections for Ar at 100 eV were compared with the previously published data [96]. Our relative cross

sections were normalized to the reference data in order to achieve the best agreement, and the comparison yielded the correction factors that were subsequently applied at small scattering angles. In this way, the effective scattering volume correction was determined directly under our experimental conditions, ensuring that deviations arising from the angular dependence of $V_{\text{eff}}(\theta)$ were properly accounted for.

3.3.2 Measurement of Absolute Differential Cross Sections for Elastic Electron Scattering

In our experiment, we first measured the relative differential cross sections (rDCSs) for elastic electron scattering from anesthetic molecules at a fixed incident electron energy as a function of the scattering angle. The next step is to transform these relative measurements, which are more straightforward to obtain and well established, into an absolute scale. This is achieved by employing known reference absolute differential cross sections [93,96], thereby enabling reliable normalization of the experimental data.

The relative differential cross sections are normalized to an absolute scale by means of a few absolute points (in our case two or three) at different scattering angles using the relative flow method, developed by Srivastava et al. [100], with argon, a gas of well-known absolute cross sections, serving as the reference [101–103]. The essence of the experiment lies in comparing the elastic scattering signals for the target molecule and the reference gas at the same incident electron energy, the same scattering angle, and under identical experimental conditions. The crucial aspect of absolute cross section measurements by the relative flow method is ensuring that these experimental conditions remain the same, which is achieved by adjusting the gas beams so that both the reference gas and the target molecule produce identical beam profiles, i.e., the same angular flux distribution. To accomplish this, certain experimental requirements must be satisfied.

It was demonstrated computationally by Olander and Kruger (1970) that for $K_\lambda \geq \gamma$ (where K_λ is the Knudsen number, defined as the ratio between the molecular mean free path and the gas needle length, $K = \lambda/L$, and γ is the ratio of the gas needle diameter to its length, d/L), the angular distribution functions of any two gases are identical [105]. The necessary condition is that the pressures at the gas needle are such that the mean free paths for both gases are the same.

From gas-kinetic theory, the relationship between the mean free path, the pressure, and the square of the molecular kinetic diameter is given by:

$$\lambda = \frac{RT}{\sqrt{2}\pi N_A \, D^2 p}, \tag{3.4}$$

where $R = 8.314$ J mol^{-1}K^{-1} is the universal gas constant, $N_\text{A} = 6.022 \times 10^{23}$ mol^{-1} is Avogadro's number, λ is the mean free path, T is the gas temperature, p is the pressure behind the gas needle, and D^2 is the square of the gas kinetic diameter.

From this expression, it follows that the mean free path of a gas molecule is inversely proportional to both the square of its kinetic diameter and the pressure. To ensure identical experimental conditions (i.e., the same beam profiles and the same mean free paths), the pressures and the squares of the gas kinetic diameters for the reference gas ($p_{\text{ref}}, D^2_{\text{ref}}$) and the target gas ($p_x, D^2_x$) must satisfy the following relation:

$$\frac{p_x}{p_{\text{ref}}} = \frac{D^2_{\text{ref}}}{D^2_x}, \tag{3.5}$$

If these conditions are satisfied, the measured intensities of scattered electrons can be converted into absolute differential cross sections using the following expression [101–103]:

$$\mathrm{DCS}_x(E_0,\theta) = \mathrm{DCS}_{\mathrm{ref}}(E_0,\theta)\,\frac{N_x\,F_{\mathrm{ref}}}{N_{\mathrm{ref}}\,F_x}\sqrt{\frac{M_{ref}}{M_x}}, \tag{3.6}$$

where $\mathrm{DCS}_x(E_0,\theta)$ and $\mathrm{DCS}_{\mathrm{ref}}(E_0,\theta)$ denote the absolute differential cross sections for elastic electron scattering from the target molecules and the reference gas, respectively. N_x and N_{ref} are the measured intensities of the scattered electrons, F_x and F_{ref} are the corresponding mass flows, while M_x and M_{ref} represent the molecular masses of the target and the reference gas, respectively.

This relation represents the essence of the relative flow method, since it allows the measured relative differential cross sections for the target to be normalized to an absolute scale by direct comparison with the reference gas of known absolute cross sections.

In addition to the measurement of the scattered electron intensities from both the target molecules and the reference gas (N_x and N_{ref}), another experimentally determined quantity is the mass flow F of the two gases. Since the gas pressure can be efficiently monitored during the experiment, it is necessary to establish a direct relation between the pressure and the corresponding mass flow.

The preparation of the system for measurements is carried out as follows:

1) The schematic of the gas system of the UGRA apparatus are shown in Figure 3.10. Let us first consider the sample gas line. By means of valves V_1 and V_2, the line is evacuated with a mechanical rotary pump to the forevacuum level ($p \approx 10^{-2}\,\mathrm{mbar}$) in several pumping cycles, thereby removing any residual gas (with valves V_x, V_4, and V_5 kept closed), up to valve V_5, which is used to admit the gas into the chamber through the gas needle. Then, the system is further evacuated by the turbomolecular pump to a high vacuum of the order of $10^{-7}\,\mathrm{mbar}$.

   Before admitting the sample into the vacuum chamber (by fine adjustment of valve V_4), several freeze–thaw–pump cycles are performed at liquid nitrogen temperature, using valves V_x, V_1, and V_2. This procedure is crucial to clean the sample gas line from impurities and to remove adsorbed contaminants from the walls.

   The reference gas line is evacuated through valves V_3 and V_2 down to the forevacuum level, with valves V_{ref}, V_6, and V_5 closed. In this way, forevacuum conditions are achieved up to valves V_4 and V_6, while opening valve V_5 provides high vacuum from that point onward.

2) The next step is to introduce the sample and reference gases into the chamber. The reference gas is admitted through the gas needle by opening valve V_{ref} and, with the regulating valve V_9 properly positioned (to direct the gas through the needle), by carefully opening valve V_6 until the desired pressure is reached and equilibrium is established. The pressure at the needle, p_{ref}, is monitored with a Baratron gauge.

   Subsequently, valve V_9 is adjusted to divert the reference gas through the side leak, and the chamber pressure is then monitored with an ionization gauge. When the pressure at the needle drops nearly to zero, the sample gas is introduced into the chamber through the needle. This is accomplished by opening valve V_x, positioning the distribution valve V_8 accordingly, and carefully opening valve V_4 until the desired pressure is reached on the Baratron gauge. The pressures of both gases are adjusted so that their mean free paths are approximately the same, which is achieved when the condition from Eq.3.5 is satisfied.

3) Once the sample gas is set to enter the chamber through the needle and the reference gas through the side leak (i.e., with V_8 directed toward the baratron and V_9 set to the

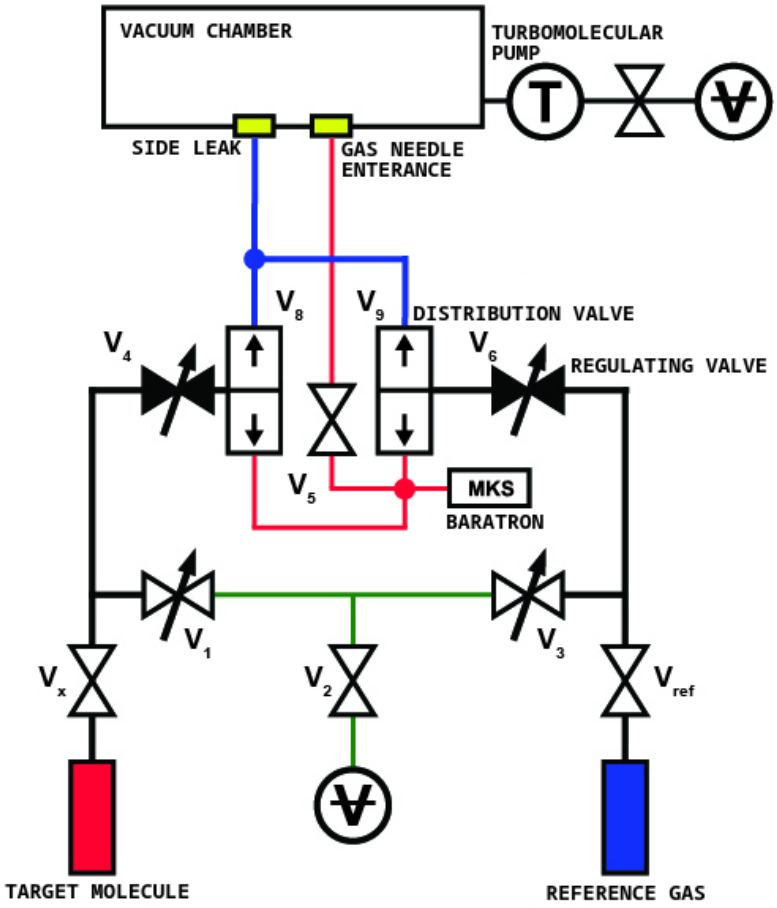

Figure 3.10: Gas system of the UGRA apparatus.

side leak), the pressure P_B at the baratron is measured by closing valve V_5, starting from p_x. Using the `LabView` program, the change in p_B over time was monitored to determine dp_B/dt. After recording the required dependence, valve V_5 is opened and the pressure is allowed to return to the initial value p_x. This measurement allows determination of the gas flow for the sample. The same procedure is repeated for the reference gas, with the sample now entering through the side leak and the reference gas through the needle.

4) The mass flow, $F = dn/dt$, can be obtained from the measured pressure change over time, dp_B/dt [103], using the ideal gas law,

$$pV_0 = nRT_0, \tag{3.7}$$

where T_0 is the temperature, R is the universal gas constant, n is the number of moles of gas, p is the pressure, and V_0 is the volume. Differentiating with respect to time gives

$$\frac{dp}{dt} = \frac{RT_0}{V_0}\frac{dn}{dt} = cF. \tag{3.8}$$

From this relation, the mass flow can be determined by measuring the pressure change over time, under the condition that the gas volume V_0 and temperature T_0 remain constant. The flow F corresponds to the slope of the $p(t)$ curve in the region where the pressure varies linearly with time. Figure 3.11 shows examples of $p(t)$ curves for the reference gas and the sample gas, with the corresponding flows determined from the linear fit.

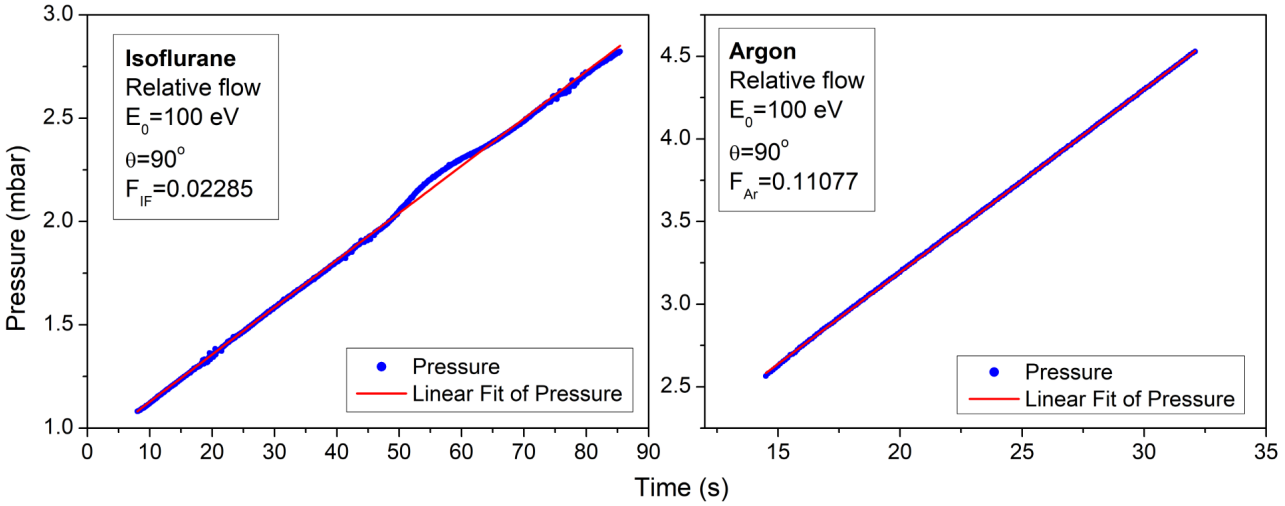

Figure 3.11: Examples of $p(t)$ curves for the sample gas (isflurane) and the reference gas (Ar), used to determine the mass flow F from the slope of the linear region.

The total pressure in the chamber (sample + reference gas) was monitored using an ionization gauge and did not exceed order of magnitude of 10^{-6} mbar. When the molecules of the sample gas (or the reference gas) are introduced into the chamber through the needle (with the valve positions described previously) and the beam stabilizes, the measurement of the elastically scattered electron intensity is performed at a specified incident electron energy and scattering angle. A single measurement at a given energy E_0 and angle θ consisted of the following steps:

1. Measurement of the intensity of electrons scattered from the sample, N_x (with the sample gas entering the chamber through the gas needle and the reference gas through the side inlet).

2. Measurement of the mass flow for the sample gas, F_x.

3. Measurement of the intensity of electrons scattered from both the sample and the reference gas entering through the side inlet, representing the background signal to be subtracted.

4. Measurement of the intensity of electrons scattered from the reference gas, N_{ref} (with the reference gas entering the chamber through the needle and the sample gas through the side inlet).

5. Measurement of the mass flow for the reference gas, F_{ref}.

For each fixed electron energy E_0 and scattering angle θ, typically 2–3 consecutive measurements were performed, and the mean value was calculated.

For gas targets (e.g., Ar), the determination of the gas flow can be performed with high accuracy by monitoring the pressure variation over time. However, for some molecular targets, effects such as adsorption on surfaces can significantly influence the measurement of the flow F and, consequently, the value of the differential cross section. These effects are particularly pronounced during the pressure increase regime (Method of Pressure Increase, MPI, as defined in [106]) at room temperature, since the system is far from equilibrium and adsorption/desorption effects are not compensated [106].

These effects can be mitigated by heating the entire system, including the sample, tubing, valves, and needle. Heating reduces adsorption, thereby increasing the accuracy of the F measurement, which in turn improves the precision of the absolute differential cross section

determination according to Equation 3.6. Additionally, the heater power is adjusted to maintain a small positive temperature gradient from the sample to the needle, preventing condensation and improving the signal by increasing the vapor pressure of the sample.

3.3.3 Integral and Momentum Transfer Cross Sections

Since our experimental differential cross sections (DCSs) were obtained over a limited angular range, it is necessary to extrapolate them to include the smallest (0°) and largest (180°) scattering angles in order to determine elastic integral cross sections (ICSs) and momentum transfer cross sections (MTCSs).

The extrapolation was performed by considering the theoretically obtained shapes of the DCSs at small (0–25°) and large (120–180°) scattering angles, while the experimental DCS values from 25° to 125° were retained. The theoretical DCSs were normalized to the experimental points to ensure the best agreement. The normalized theoretical points at the extreme angles were then treated as extrapolated experimental values.

Using the resulting DCSs over the full angular range, the ICSs and MTCSs were calculated by standard integration:

$$\mathrm{ICS} = 2\pi \int_0^\pi \mathrm{DCS}(\theta) \sin\theta \, d\theta, \tag{3.9}$$

$$\mathrm{MTCS} = 2\pi \int_0^\pi \mathrm{DCS}(\theta)(1 - \cos\theta) \sin\theta \, d\theta. \tag{3.10}$$

This procedure allows the evaluation of integral quantities that account for the entire angular distribution of elastically scattered electrons, providing a complete description of the scattering process.

3.3.4 Evaluation of Measurement Uncertainties

Uncertainties of the relative differential cross sections as a function of the scattering angle include both statistical uncertainty, determined from the Poisson distribution, and system stability uncertainty („Short Term Stability Error“), estimated from the spread of repeated measurements at the same energy and angle. In our measurements, the statistical uncertainties were typically in the range of 0.1–5.5%, while the uncertainties due to short-term system instabilities ranged between 0.3–18%. At small scattering angles (below 40°), the overall uncertainty of the relative DCSs was increased by 20% in order to account for possible variations of the effective scattering volume.

For the absolute DCSs, obtained by the relative flow method, the total uncertainty is predominantly determined by the accuracy of the reference absolute cross sections for argon. The uncertainties related to the measured signal intensities and gas flow rates were found to be small, owing to stable experimental conditions and a high signal-to-noise ratio. In this work, we employed the absolute DCSs of Ranković et.al.(2018) [96] as the reference set for incident electron energies 50, 100, 150, 200 and 300 eV, while for 250 eV we used the data of Williams and Willis (1975) [93].

The uncertainties of the reference absolute DCSs are about 20%, which represents the minimum error contribution. The overall uncertainty for DCSs was calculated by summing the squares of individual independent uncertainties and taking the square root. Consequently, the aggregate uncertainty of our absolute DCS measurements was estimated to be about 20–25%, while at small scattering angles it could reach up to 30%.

The total uncertainties of the integral cross sections (30%) arise from the absolute DCS uncertainties (25% in average) and uncertainties of the extrapolation of DCSs to 0° and to 180°

(15%) and numerical integration (8%). Following the same procedure as for DCS uncertainties, the overall uncertainty was calculated by taking the square root of the sum of the squares of the individual independent uncertainties.

Chapter 4

Results and Discussion

In this chapter, the results of our measurements are presented and discussed for the series of halogenated anesthetics investigated in this work. The analysis is structured by molecular targets, with separate sections devoted to halothane, isoflurane, sevoflurane, and desflurane. For each compound, the physical and chemical properties relevant to the experiment are first summarized, followed by a description of the sample preparation and application of the relative flow method. Subsequently, the measured differential, integral, and momentum transfer cross sections are compared with available theoretical calculations and previously published data, where such references exist. This organization enables a clear assessment of the consistency and reliability of the present results and facilitates comparison across the studied molecules.

4.1 Halothane

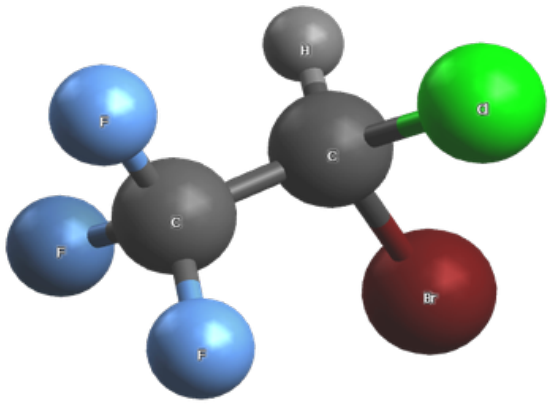

Figure 4.1: Schematic representation of the molecular structure of halothane ($CF_3CHBrCl$), illustrating the arrangement of the halogen substituents around the ethane backbone [107].

Halothane, commonly known as 2-bromo-2-chloro-1,1,1-trifluoroethane ($CF_3CHBrCl$), is a multihalogenated derivative of ethane. It is a clear, colorless, and highly volatile liquid characterized by a sweet, chloroform-like odor. The compound has a boiling point of 50.2°C, a molar mass of 197.379 g/mol, a vapor pressure of 243 mmHg [108], and a dipole moment of 1.41 D [21]. The molecular structure of halothane is presented in Figure 4.1.

Halothane was first synthesized in 1954 by Charles Suckling and introduced into clinical practice in 1956 as an inhalational anesthetic [109]. Since its introduction, halothane has been extensively studied, and more recent investigations have increasingly focused on its environmental impact.

Table 4.1: Chemical properties of halothane.

Property	Symbol	Value
Boiling point	T_b	50.2°C
Molar mass	M	197.379 g/mol
Vapor pressure	p_v	243 mmHg
Dipole moment	μ	1.41 D
Estimated gas kinetic diameter	D_{HL}	5.6 Å
Global warming potential	GWP	218*
Ozone depletion potential	ODP	1.56**

* Computed value for halothane in relation to GWP for CCl_2F_2 (CFC-12, freon-12).
** ODP values relative to CCl_3F (CFC-11, freon-11).

In this work, both experimental and theoretical cross sections for elastic electron scattering from halothane are presented. Absolute differential cross sections (DCSs) were measured in the intermediate incident energy range of 50–300 eV and for scattering angles between 20° and 110°. Initially, relative DCSs were obtained and subsequently placed on an absolute scale by means of the relative flow technique, employing argon as the reference gas (see Chapter 3). The experimental results are complemented by calculations within the IAM-SCAR+I framework (Chapter 2). In addition, integral cross sections (ICSs)and momentum transfer cross sections (MTCSs) both experimental and theoretical, are reported for the same energy range.

Anhydrous halothane with a stated purity of more than 99% was employed as the target gas in the present measurements. The sample was stored in a sealed glass container and introduced into the scattering chamber through a stainless steel gas line and a needle system. Prior to use, several freeze–pump–thaw cycles were carried out under vacuum in order to remove dissolved impurities. Since halothane is liquid at room temperature (boiling point 50.2°C; vapor pressure 243 mmHg at 20°C, see Table 4.1), the container was heated to approximately 40°C to ensure adequate vapor pressure. To avoid condensation of the vapor in the line or chamber, both the gas line and the chamber were heated to establish a positive temperature gradient, from 40°C at the container up to 50°C near the gas needle. Under optimal vacuum conditions, the base pressure of the chamber was $6 \cdot 10^{-7}$ mbar, which increased by about one order of magnitude upon gas admission.

As described in Section 3.3.2, during the relative flow measurements absolute values can be obtained by adjusting the pressures behind the gas needle for the reference gas, argon (p_{Ar}), and the target gas, halothane (p_{HL}), in such a way that their ratio is inversely proportional to the square of their gas kinetic diameters (D_{Ar} and D_{HL}). With the gas kinetic diameter of argon known as $D_{\mathrm{Ar}} = 3.58$ Å and that of halothane estimated as $D_{\mathrm{HL}} = 5.6$ Å [110], the required pressure ratio is found to be $p_{\mathrm{Ar}} : p_{\mathrm{HL}} \approx 2.45$. In the present experiment, pressures were set to $p_{\mathrm{HL}} = 1.0 \times 10^{-6}$ mbar and $p_{\mathrm{Ar}} = 2.5 \times 10^{-6}$ mbar, thus fulfilling this condition. For each incident electron energy, three absolute reference points were determined at the scattering angles of 40°, 70°, and 100°.

To the best of the author's knowledge, only one previous study by Maioli et al. [25] has provided combined experimental and theoretical DCSs and ICSs for electron scattering from halothane. In that study, both theoretical and experimental investigations of elastic electron scattering from halothane were carried out. On the theoretical side, differential and integral cross sections were computed using the Schwinger multichannel method with pseudopotentials (SMCPP), as well as the independent atom model with screening corrected additivity rule and interference effects (IAM-SCAR+I). Experimentally, relative elastic DCSs were measured with a VG-SEELS 400 electron scattering spectrometer for incident energies of 10, 20, 30, and 50 eV over the angular range 7°–100°. Absolute values of the experimental DCSs were obtained

by normalization to the theoretical data at 30°, and the reported results showed reasonable agreement with the theoretical predictions.

4.1.1 Differential Cross Sections

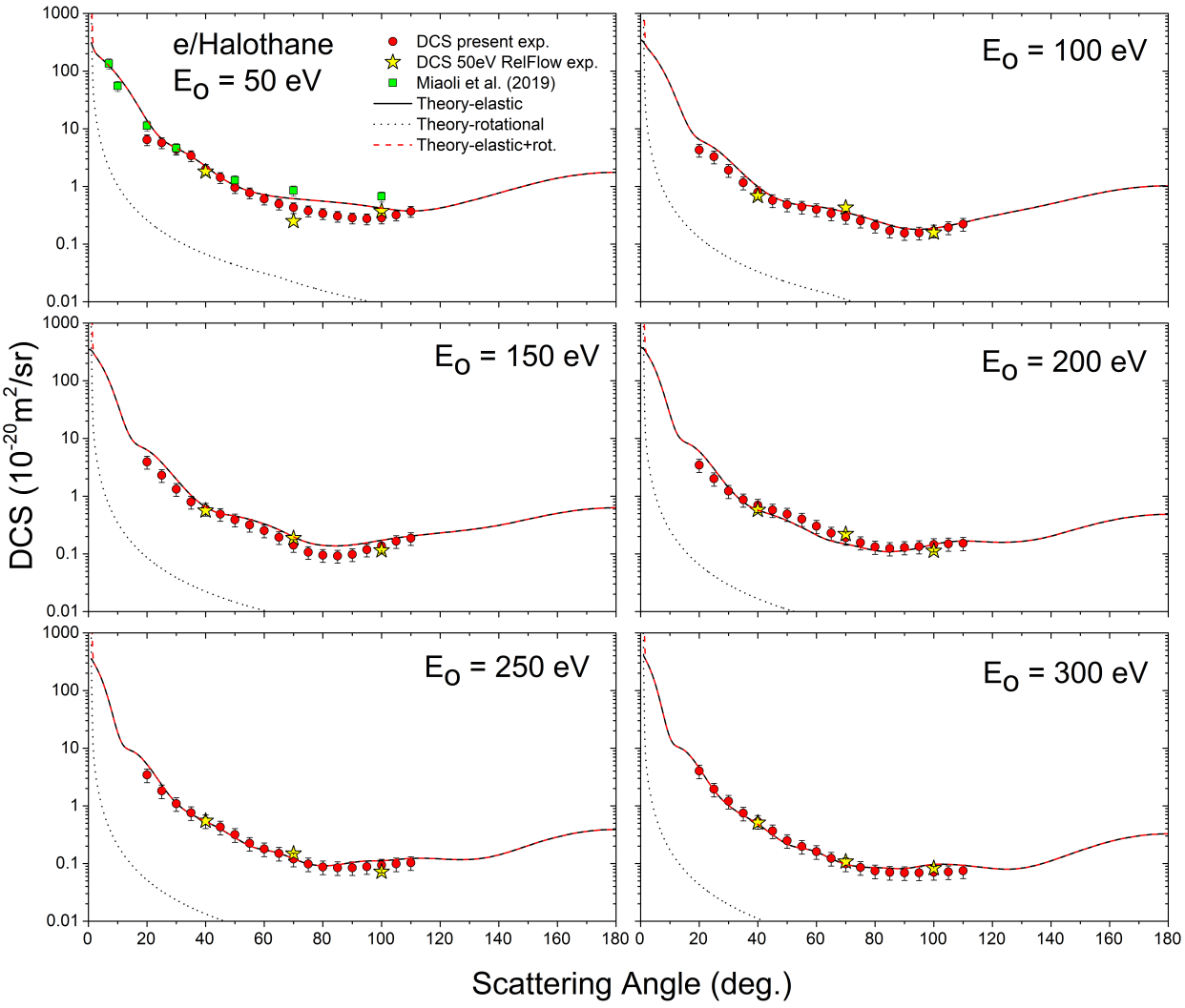

Figure 4.2: Absolute differential cross sections (in units 10^{-20}m^2/sr) for elastic electron scattering from a halothane molecule at energies of 50, 100, 150, 200, 250, and 300 eV. The present results include the following: present experimental data (red circles), present theory (elastic scattering - black solid line, rotational excitations - black dots and combined elastic and rotational cross sections - red dashed line), experimental absolute points obtained by the relative flow method (yellow stars), and experimental results by Maioli et al. at 50 eV (green squares) [107].

The experimentally determined absolute differential cross sections for elastic electron scattering from halothane at incident energies of 50, 100, 150, 200, 250, and 300 eV are summarized in Table 4.2 and displayed in Fig. 4.2 (red circles). In addition, the directly measured reference points at selected energies and scattering angles of 40°, 70°, and 100°, obtained using the relative flow technique and employed to normalize the relative data to an absolute scale, are also shown (yellow stars). The consistency observed between these independently obtained datasets (relative and absolute) provides strong support for the reliability of the applied experimental

procedures. Furthermore, Fig. 4.2 includes a comparison of the present experimental absolute cross sections with corresponding theoretical predictions.

As can be seen from Fig. 4.2, the overall agreement between experiment and theory improves with increasing incident electron energy, culminating in an almost quantitative match at 300 eV. The most significant discrepancy is observed at 50 eV around a scattering angle of 20°, which is most likely associated with detector saturation effects during the measurement. Since our experimental data include unresolved rotational excitations, they should be regarded as quasi-elastic. The theoretical model, therefore, provides both the purely elastic and the elastic+rotational cross sections, with the purely rotational contribution also shown separately. Importantly, the difference between the elastic and quasi-elastic cross sections is noticeable only at very small scattering angles, while within the angular range of the present experiment (20°–110°) this deviation remains negligible. For instance, at 50 eV, where the rotational excitations reach their maximum contribution, their effect on the quasi-elastic signal varies from only 1.5% to 4.5%, which is well below the experimental uncertainty (minimum value around 20%).

Consistent with general trends reported for molecular targets [**?**, **?**, **?**], the DCSs display a broad minimum near 100° at lower impact energies (50 and 100 eV), which gradually fades at higher energies. In the 200–300 eV range, the angular distributions become nearly flat between 80° and 110°, confirming the dominant role of forward scattering and the diminishing influence of low-energy rotational dynamics at larger scattering angles.

At an incident energy of 50 eV, our differential cross sections are compared with the experimental results reported by Maioli et al. [107]. A very good agreement is observed at a scattering angle of 30°, while at the remaining angles our measured values tend to be somewhat lower. It should be noted, however, that the absolute scale of the Maioli dataset was obtained by normalizing to theoretical calculations (IAM-SCAR+I) at 30°, whereas the present results are independently normalized using the relative flow method and are therefore free from any theoretical input. In this respect, our data provide an important independent benchmark. Furthermore, to the best of our knowledge, there are no previously published experimental DCS data for halothane at incident energies above 100 eV. The present measurements thus fill an evident gap in the literature and can serve as a valuable reference point for future theoretical and experimental investigations.

4.1.2 Integral and Momentum Transfer Cross Sections

Figure 4.3 shows the experimental and theoretical integral cross sections (ICSs) for electron scattering from halothane. The experimental data include the present measurements of elastic scattering over the 50–300 eV energy range, as well as previously reported results by Maioli et al. [25] for 10–50 eV. The theoretical ICSs account for purely elastic scattering, inelastic processes, rotational excitations, total cross sections, and the combined elastic plus rotational contributions.

Figure 4.3 illustrates that, while the overall shapes of the experimental and theoretical integral cross sections are similar, the measured values are systematically lower than the calculated ones. Since the experimental DCS data cover a limited angular range, the reported integral cross sections rely significantly on extrapolation. To ensure consistency, the calculated DCS were first normalized to the measured absolute values, and these normalized data were then integrated. The resulting integral cross sections, presented in Table 1, carry an estimated uncertainty of 35% due to the extrapolation procedure. At the single energy (50 eV) where comparison with the data of Maioli [25] is possible, excellent agreement was found.

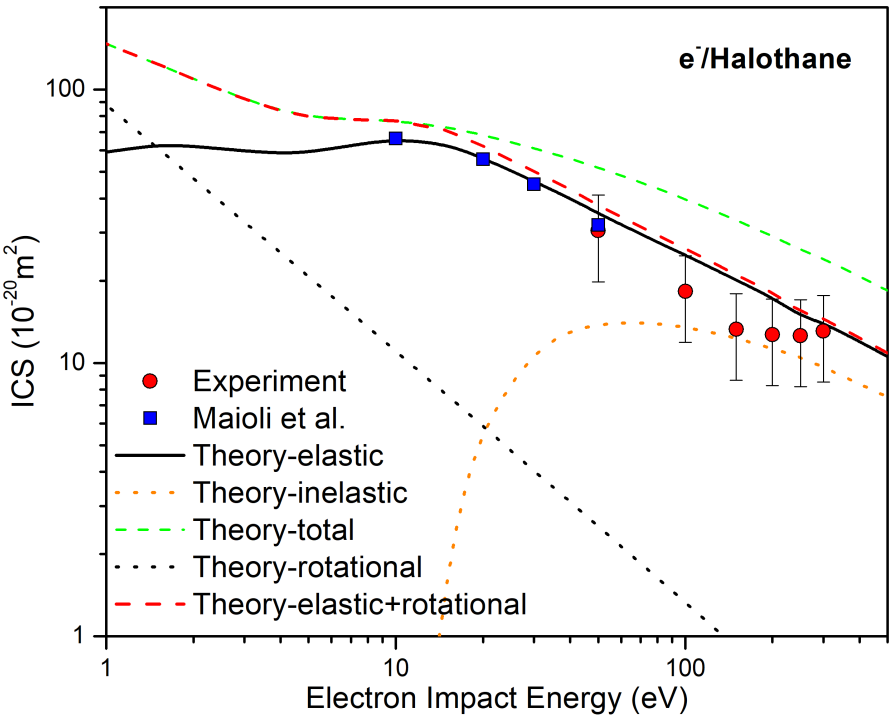

Figure 4.3: Integral cross sections for electron interactions with the halothane. The following results are included: present experimental points (red circles), present theoretical elastic (black solid line), inelastic (orange dots), rotational (black dots), elstic+rotational (red dashed line) and total (green dashed line) ICSs, as well as ICS by Maioli et al. (blue squares) [25].

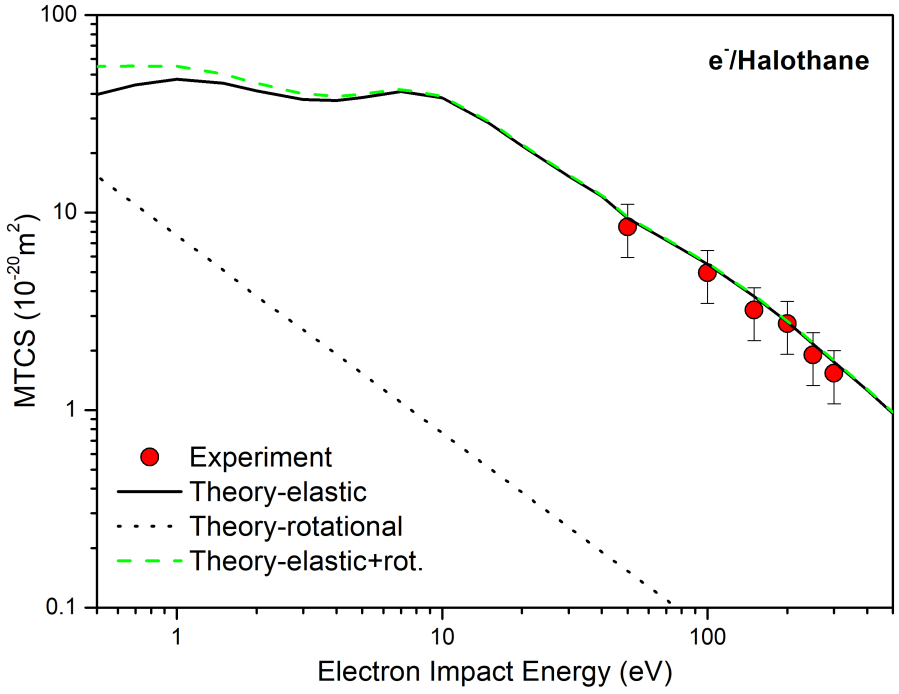

Figure 4.4: Momentum transfer cross sections for electron scattering from the halothane molecule. The present experimental data are shown as red circles, while the theoretical ones are presented as follows: elastic (solid black curve), rotational (black dots), and combined elastic+rotational (green dashed line).

In Figure 4.4, the momentum transfer cross sections (MTCSs) for electron scattering from halothane are shown. Experimental results, covering 50–300 eV, are plotted with error bars, while theoretical values are given for 1–500 eV. The latter comprise purely elastic (solid black line), rotational (dotted line), and combined quasi-elastic contributions (red dashed line).

As illustrated in the figure, in contrast to the integral cross sections, the experimental momentum transfer cross sections exhibit an excellent overall agreement with the theoretical predictions. This behavior can be attributed to the $1 - \cos\theta$ weighting factor in Eq. 3.10, which is used to calculate the MTCS from the differential cross sections. Due to this factor, the contributions from small scattering angles—where the largest deviations between experiment and theory are observed—are significantly suppressed. Consequently, the MTCS is primarily influenced by scattering at intermediate angles, where the experimental and theoretical DCSs are in much better agreement. As a result, even though the DCSs at forward angles show noticeable discrepancies, their impact on the MTCS is minor, and the overall match between experimental and calculated MTCSs is very good across the measured energy range.

Table 4.2: Experimental differential and integral (in unit $10^{-20}\,\mathrm{m}^2$) cross sections for elastic electron scattering from the halothane molecule. The absolute uncertainties, provided in parentheses, have been rounded to two significant figures. The relative uncertainties associated with the differential cross sections (DCSs) vary between 21.2 % and 26.6 %, while the estimated uncertainty for the integral cross section (ICS) is approximately 35 %. These uncertainty estimates reflect both statistical and systematic contributions inherent to the experimental procedure [107].

	DCS ($10^{-20}\,\mathrm{m}^2\mathrm{sr}^{-1}$)					
$\theta\,(^\circ)$	50 (eV)	100 (eV)	150 (eV)	200 (eV)	250 (eV)	300 (eV)
20	6.5(1.4)	4.3(1.1)	3.92(98)	3.46(89)	3.44(92)	4.0(1.1)
25	5.7(1.2)	3.29(82)	2.31(58)	2.02(52)	1.82(48)	1.95(52)
30	4.43(94)	1.92(48)	1.33(33)	1.23(32)	1.09(29)	1.20(23)
35	3.41(72)	1.16(29)	0.80(20)	0.87(22)	0.76(20)	0.749(20)
40	1.99(42)	0.79(20)	0.60(15)	0.70(18)	0.55(15)	0.536(14)
45	1.43(30)	0.57(14)	0.49(12)	0.58(15)	0.43(11)	0.368(98)
50	0.96(20)	0.48(12)	0.392(98)	0.49(13)	0.318(85)	0.250(66)
55	0.77(16)	0.44(11)	0.319(80)	0.40(10)	0.224(60)	0.198(53)
60	0.61(13)	0.40(10)	0.255(64)	0.303(78)	0.179(48)	0.161(43)
65	0.50(11)	0.339(85)	0.194(48)	0.230(59)	0.150(40)	0.123(33)
70	0.429(91)	0.295(74)	0.142(35)	0.191(49)	0.120(32)	0.099(26)
75	0.377(80)	0.253(63)	0.107(27)	0.157(41)	0.098(26)	0.085(23)
80	0.340(72)	0.208(52)	0.095(24)	0.132(34)	0.087(23)	0.074(20)
85	0.304(64)	0.171(43)	0.092(23)	0.125(32)	0.085(23)	0.070(19)
90	0.284(60)	0.154(39)	0.098(24)	0.130(33)	0.084(22)	0.069(18)
95	0.275(58)	0.157(39)	0.118(30)	0.134(35)	0.088(24)	0.069(18)
100	0.285(60)	0.170(43)	0.138(34)	0.145(38)	0.094(25)	0.070(19)
105	0.320(68)	0.195(49)	0.166(41)	0.150(39)	0.099(26)	0.072(19)
110	0.370(78)	0.223(56)	0.187(47)	0.153(40)	0.103(28)	0.075(20)
ICS	31(12)	18.3(6.4)	13.3(4.7)	12.7(4.4)	12.6(4.4)	13.1(4.6)
MTCS	8.5	5.0	3.2	2.7	1.9	1.5

4.2 Isoflurane

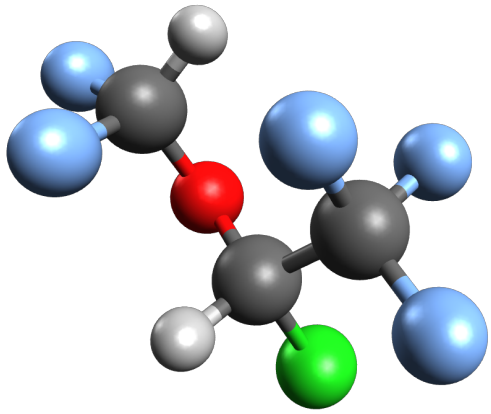

Figure 4.5: The figure provides a schematic representation of the molecular structure of isoflurane, highlighting the arrangement of its halogen and oxygen atoms.

Isoflurane (2-chloro-2-(difluoromethoxy)-1,1,1-trifluoroethane, $CF_3CHCl\text{-}O\text{-}CHF_2$), developed originally by Ohio Medical Products approximately five decades ago, has become one of the most widely employed inhalational anesthetics in clinical practice [111]. It is classified as a non-flammable halogenated ether and is typically encountered as a clear, colorless liquid characterized by a mild, somewhat ether-like odor. The compound possesses a molecular weight of 184.49 g/mol, a boiling point of 48.5 °C, and a vapor pressure of 330 mmHg [112]. Furthermore, its estimated dipole moment amounts to 2.47 D [113]. The relevant physicochemical characteristics of isoflurane are summarized in Table 4.3, while its molecular structure is illustrated in Figure 4.5.

In recent years, beyond its medical applications, isoflurane has attracted increasing attention due to its potential environmental impact, particularly in the context of greenhouse gas emissions and climate change considerations.

Table 4.3: Chemical properties of isoflurane.

Property	Symbol	Value
Boiling point	T_b	48.5°C
Molar mass	M	184.49 g/mol
Vapor pressure	p_v	330 mmHg
Dipole moment	μ	2.47 D
Estimated gas kinetic diameter	D_{IF}	5.57 Å
Global warming potential	GWP	1401*

* Computed value for isoflurane in relation to GWP of CO_2 for a 20-year time horizon.

In this section, we present both experimental and theoretical results for the elastic scattering of electrons from the isoflurane molecule. The measurements were carried out over a selected range of incident electron energies, E_0, extending from 50 to 300 eV, and within a scattering angular interval between 25° and 125°. The reliability and consistency of the experimental data are further supported by theoretical predictions obtained within the IAM-SCAR+I framework, which provides a solid basis for comparison. In addition to the differential cross sections, this study also reports integral cross sections (ICSs) and momentum transfer cross sections (MTCSs), derived from both experiment and theory, covering the same energy range [8].

Anhydrous isoflurane, with a stated purity exceeding 99%, was employed as the target gas in the present experiments. Prior to use, the sample underwent several freeze–pump–thaw cycles under vacuum in order to eliminate dissolved impurities, following the same preparation procedure as described for halothane. The substance was introduced into the scattering chamber through a gas needle connected to a line system originating from a glass reservoir. Under optimal vacuum conditions, the base pressure in the chamber was typically $6 \cdot 10^{-7}$ mbar, increasing by approximately one order of magnitude upon admission of the gas.

For isoflurane, the same relative flow procedure was applied as described for halothane. Using the gas kinetic diameter of argon ($D_{\mathrm{Ar}} = 3.58$ Å) and the estimated value for isoflurane ($D_{\mathrm{IF}} = 5.57$ Å) [8], the required pressure ratio was $p_{\mathrm{Ar}} : p_{\mathrm{IF}} \approx 2.4$. In the present measurements, the pressures were set to $p_{\mathrm{IF}} = 1.0{\times}10^{-6}$ mbar and $p_{\mathrm{Ar}} = 2.4{\times}10^{-6}$ mbar, in agreement with this condition. For each incident energy, two absolute reference points were obtained at scattering angles of 40° and either 70°, 80°, or 90°.

The key reference for isoflurane is the PhD thesis of E. Lange [31], which reports both theoretical (SMCPP and IAM-SCAR+I) and experimental cross sections. Differential cross sections were measured for incident energies between 10 and 50 eV and scattering angles from 8° to 70°, with the absolute scale established by normalization to IAM-SCAR+I at 30°. The results showed overall good agreement between experiment and theory.

4.2.1 Differential Cross Sections

In the case of isoflurane, absolute differential cross sections for elastic electron scattering were obtained at incident energies of 50, 100, 150, 200, 250, and 300 eV. These results are displayed in Fig. 4.6 (red circles), together with the directly measured reference points at selected scattering angles (40° and either 70°, 80°, or 90°), indicated by red stars. The latter points, determined through the relative flow technique, were employed to scale the relative measurements to an absolute level, ensuring consistency between independent datasets. The comparison with theoretical predictions is also included in Fig. 4.6, providing additional verification of the experimental procedure. A numerical overview of the obtained absolute cross sections is presented in Table 4.4.

As illustrated in Fig. 4.6, the experimentally obtained differential cross sections for isoflurane exhibit a generally very good level of consistency with the corresponding theoretical results. In particular, the agreement is excellent at an incident electron energy of 100 eV. Nevertheless, some discrepancies can be observed, most notably at 50 eV and a scattering angle of 25°, where the measured values deviate from theory. This deviation is most likely a consequence of saturation effects in the electron multiplier detector (channeltron), which can occur under experimental conditions optimized for high-statistics measurements at minimum. In this regime, extremely high counting rates are encountered, primarily due to the relatively large incident electron current, the limited energy resolution, and the fact that cross sections in this angular range can vary by several orders of magnitude. Furthermore, at 150 eV our measured DCSs are consistently lower than the calculated values, which consequently results in reduced values of the corresponding integral cross sections (ICSs).

It should also be emphasized that, under the present experimental conditions, rotational excitations cannot be separated from purely elastic scattering. Accordingly, the experimental data represent “quasi-elastic” cross sections, which are therefore compared with the sum of the calculated elastic and rotational contributions. This combined theoretical dataset is represented by the red dashed line in Fig. 4.3, and provides a more realistic reference for comparison with experiment. The analysis indicates that rotational excitations contribute significantly at small scattering angles, with the effect being most pronounced at 50 eV. Given that isoflurane is a polar molecule with a substantial permanent dipole moment [113], such a strong role of

rotational excitations is not unexpected.

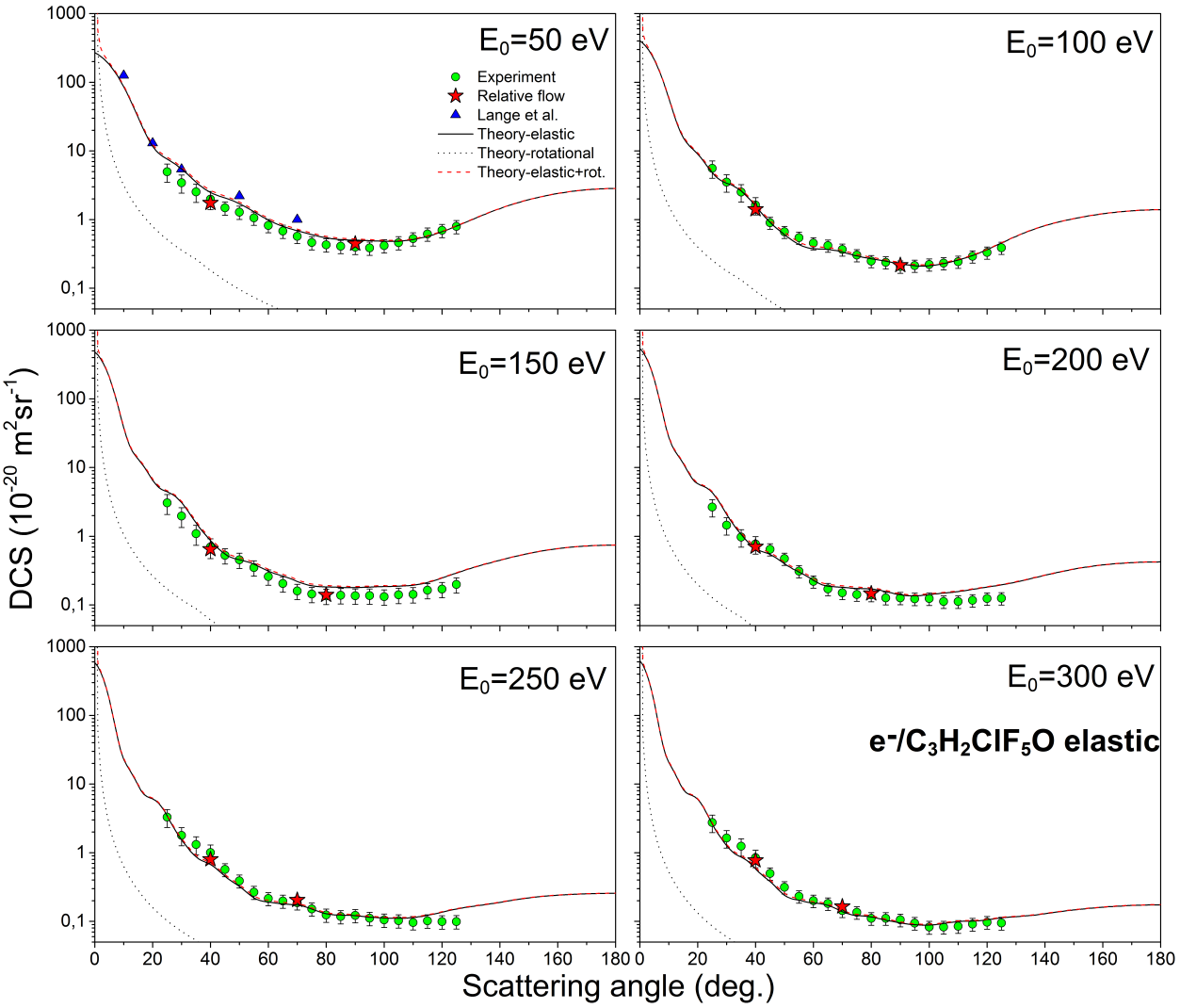

Figure 4.6: Absolute differential cross sections (in units of $10^{-20}\,\mathrm{m^2\,sr^{-1}}$) for elastic electron scattering from the isoflurane molecule are presented at incident electron energies of 50, 100, 150, 200, 250, and 300 eV. Several data sets are displayed for comparison: the present experimental measurements are depicted as circles (green online), while the corresponding theoretical predictions are given by a solid black curve for elastic DCSs, black dots for rotational DCSs, and a red dashed line for their combined contribution. Experimental absolute reference points obtained via the relative flow method are marked with red stars, whereas earlier experimental results reported by Lange [31] at 50 eV are shown as blue triangles.

In addition, the angular dependence of the DCSs exhibits trends characteristic of molecular targets, consistent with previous observations reported in the literature [114, 115]. At incident electron energies of 50 and 100 eV, a broad minimum appears around 100°, which becomes less pronounced as the energy increases. At higher incident electron energies, the measured DCSs exhibit a trend that resembles the Rutherford-type angular dependence. Specifically, the cross sections become strongly peaked in the forward direction, reflecting the dominance of small-angle scattering, while at larger scattering angles (above 80°) the DCSs flatten out, showing only minor variations with angle. This behavior is consistent with expectations for molecular targets at intermediate-to-high energies, where the scattering process is increasingly governed by the long-range Coulomb interaction and the independent atom picture becomes

more appropriate.

A comparison was made between the present results and those reported by Lange [31] at an incident electron energy of 50 eV. At 30° scattering angle, our data and Lange's measurements are in good agreement, falling within the experimental uncertainty. At other angles, however, the present values tend to be systematically lower than those reported previously. It is difficult to provide a definitive explanation for the observed differences between our experimental results and those reported by Lange. Nevertheless, it should be emphasized that the present cross sections were normalized to an absolute scale by means of the relative flow method, whereas the earlier data were placed on an absolute scale by normalization to the IAM-SCAR+I calculation at a scattering angle of 30°. This methodological distinction may, at least in part, account for the discrepancies. It also underlines the importance of applying independent normalization procedures when comparing different experimental datasets, particularly in the case of complex polyatomic targets such as isoflurane.

These new measurements fill a notable gap in the available experimental data for isoflurane, providing, to the best of our knowledge, the first absolute differential cross sections in the intermediate-to-high energy range of 100–300 eV.

4.2.2 Integral and Momentum Transfer Cross Sections

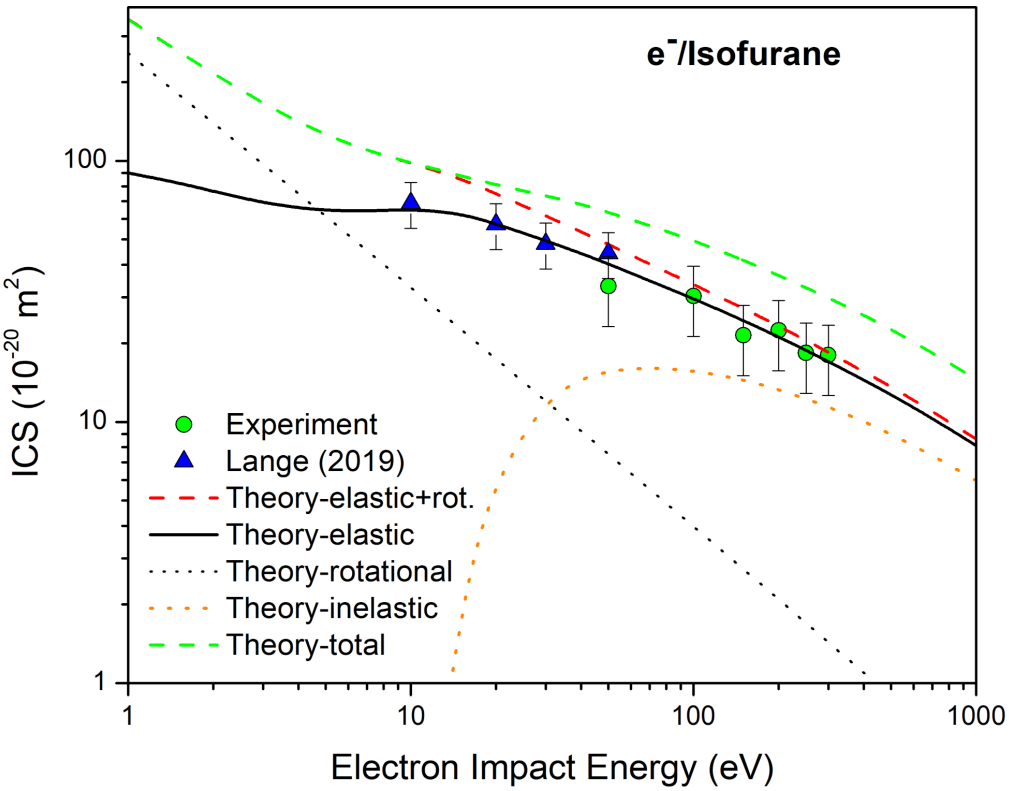

Figure 4.7: Absolute integral cross sections (in units of 10^{-20} m^2) for electron scattering from the isoflurane molecule. The present experimental measurements are displayed as circles (green online). Theoretical values are presented for purely elastic scattering (black solid line), quasi-elastic scattering including rotational excitations (red dashed line), rotational excitations (black dots), inelastic scattering (orange dotted line), and total integral cross sections (green dashed line). For comparison, the experimental data previously reported by Lange [31] are indicated by blue triangles.

Figure 4.7 presents the corresponding experimental and theoretical integral cross sections (ICSs) for electron scattering from isoflurane. The figure includes the present experimental ICSs for elastic scattering over the incident energy range of 50–300 eV, along with previously reported experimental data by Lange [31] for energies between 10 and 50 eV. The theoretical ICSs comprise contributions from purely elastic scattering, inelastic processes, total cross sections, rotational excitations, and the combined elastic plus rotational cross sections. The latter is shown for comparison with the experimental data, as the current experimental setup does not allow for a separation of purely elastic and rotationally inelastic contributions.

As shown in Figure 4.7, the experimental and theoretical integral cross sections exhibit similar overall trends; however, the measured ICSs generally display lower magnitudes compared to the calculated values. This discrepancy is largely attributable to the limited angular coverage of our differential cross section measurements, which heavily depend on extrapolation when evaluating the integral cross sections. To ensure consistency in shape, the theoretical DCSs were normalized to the experimentally determined absolute values prior to integration. The resulting ICSs, provided in Table 4.4, carry an estimated uncertainty of approximately 30%, reflecting the uncertainties inherent in the extrapolation procedure (see Subsection 3.3.4 for further details). The most pronounced deviations occur at incident electron energies of 50 and 150 eV. At 50 eV, the discrepancy arises primarily from elevated deviations at small scattering angles due to channeltron saturation effects. Similarly, at 150 eV, the measured DCSs are systematically lower than theoretical predictions, which translates into reduced ICS values. For the remaining energy points, the agreement between experiment and theory is satisfactory, falling within the experimental uncertainties. Notably, at the single energy point of 50 eV where comparison with Lange's data [31] is possible, our measured value is observed to be slightly lower in magnitude.

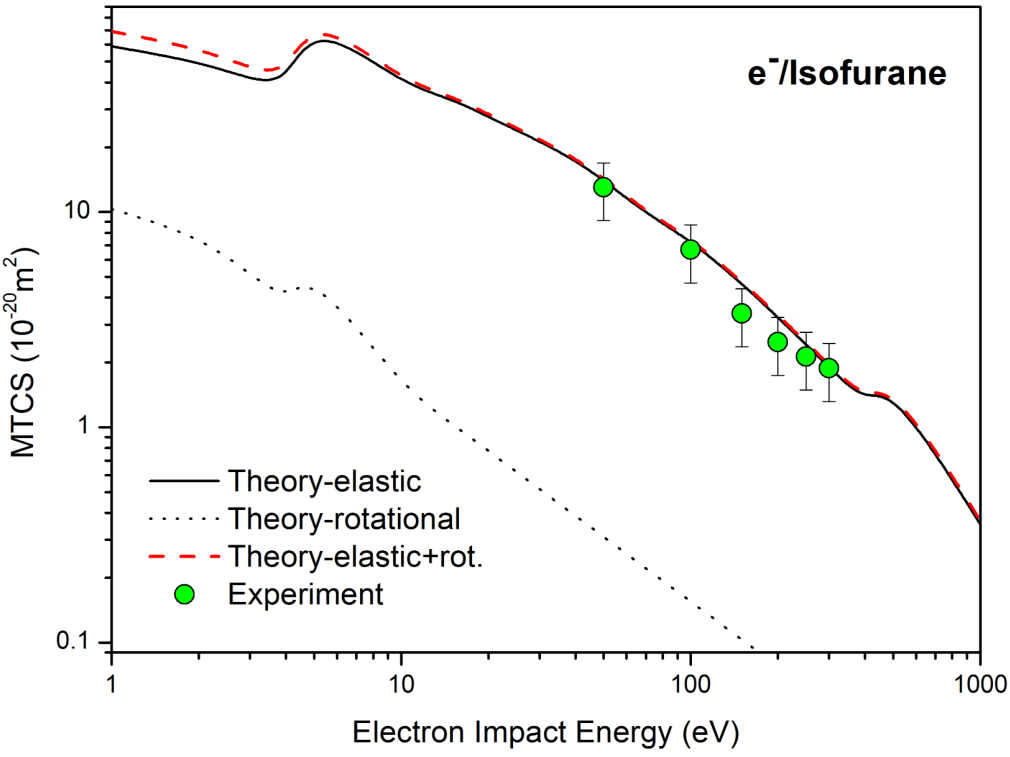

Figure 4.8: Absolute momentum transfer cross sections (in units of 10^{-20} m^2) for electron scattering from the isoflurane molecule. The present experimental data are shown as green circles, while the theoretical momentum transfer cross sections are presented as follows: elastic (solid black curve), rotational (black dots), and combined elastic+rotational (red dashed line).

In Figure 4.8, the momentum transfer cross sections (MTCSs) for electron scattering from the isoflurane molecule are presented. The experimental results, obtained in the energy range from 50 to 300 eV, are shown as discrete data points with associated error bars, while the theoretical values are displayed for the wider interval from 1 to 1000 eV. The theoretical dataset includes purely elastic contributions (solid black curve), rotational excitations (dotted black curve), as well as the combined, quasi-elastic MTCSs (red dashed curve).

Overall, the comparison demonstrates fairly good agreement between theory and experiment within the overlapping energy range. Furthermore, the experimental points follow the general decreasing trend of the MTCS with increasing energy, in line with theoretical predictions. A slight systematic offset remains, which can likely be attributed to experimental uncertainties in the absolute scale of the differential cross sections, as well as to approximations in the theoretical modeling.

The momentum transfer cross section plays a crucial role in describing electron transport through molecular gases, as it quantifies the efficiency of momentum exchange between electrons and target molecules [116–118].

Table 4.4: Experimental results for absolute differential cross-sections (DCSs), integral and momentum transfer cross-sections (ICSs and MTCSs, respectively), later two in unit $10^{-20}\,\mathrm{m}^2$, for elastic electron scattering from isoflurane. In parentheses are given absolute uncertainties of the last two digits. The relative uncertainties associated with the differential cross sections (DCSs) vary between 19.7 % and 32.1 %. The uncertainties of ICS and MTCS were estimated to be of the order of 30 %.

	DCS ($10^{-20}\,\mathrm{m}^2\mathrm{sr}^{-1}$)					
$\theta\,(^\circ)$	50 (eV)	100 (eV)	150 (eV)	200 (eV)	250 (eV)	300 (eV)
25	5.0(1.5)	5.6(1.6)	3.07(98)	2.67(76)	3.29(96)	2.74(78)
30	3.4(1.0)	3.50(99)	1.97(63)	1.45(41)	1.79(52)	1.64(47)
35	2.52(75)	2.51(71)	1.09(35)	0.97(28)	1.32(39)	1.24(35)
40	1.98(59)	1.63(46)	0.70(22)	0.77(22)	1.00(29)	0.84(24)
45	1.48(33)	0.90(18)	0.53(13)	0.65(13)	0.57(12)	0.50(10)
50	1.28(28)	0.66(13)	0.45(11)	0.472(96)	0.389(84)	0.314(64)
55	1.06(23)	0.55(11)	0.351(88)	0.311(63)	0.266(58)	0.232(48)
60	0.82(18)	0.453(91)	0.259(65)	0.220(45)	0.215(47)	0.200(41)
65	0.68(15)	0.419(84)	0.205(52)	0.171(35)	0.198(43)	0.182(38)
70	0.57(13)	0.367(74)	0.160(40)	0.150(31)	0.187(41)	0.143(30)
75	0.46(10)	0.304(61)	0.144(36)	0.142(29)	0.152(33)	0.135(28)
80	0.430(95)	0.249(50)	0.135(34)	0.140(29)	0.124(27)	0.111(23)
85	0.409(90)	0.239(48)	0.138(35)	0.126(26)	0.118(26)	0.111(23)
90	0.397(87)	0.207(42)	0.136(35)	0.127(26)	0.122(27)	0.105(22)
95	0.386(85)	0.214(43)	0.137(35)	0.123(25)	0.111(25)	0.094(20)
100	0.418(92)	0.222(45)	0.132(33)	0.124(26)	0.106(23)	0.083(18)
105	0.46(10)	0.232(47)	0.140(35)	0.112(23)	0.102(23)	0.083(18)
110	0.53(12)	0.244(49)	0.143(36)	0.112(23)	0.096(21)	0.085(18)
115	0.62(14)	0.292(59)	0.164(41)	0.117(24)	0.102(23)	0.091(19)
120	0.70(15)	0.332(67)	0.170(43)	0.124(26)	0.099(22)	0.097(21)
125	0.79(17)	0.389(78)	0.199(50)	0.125(26)	0.099(22)	0.095(20)
ICS	33.1	30.4	21.5	22.4	18.4	18.0
MTCS	13.0	6.7	3.4	2.5	2.1	1.9

4.3 Sevoflurane

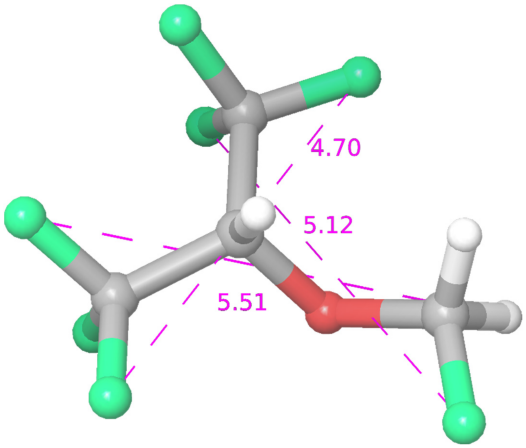

Figure 4.9: Schematic representation of the molecular structure of sevoflurane, illustrating the spatial arrangement of its fluorine, hydrogen, carbon, and oxygen atoms.

Sevoflurane (fluoromethyl 2,2,2-trifluoro-1-(trifluoromethyl)ethyl ether, $C_4H_3F_7O$) represents a modern halogenated ether anesthetic that has gained widespread acceptance in clinical practice owing to its rapid onset and favorable pharmacokinetic profile. It is classified as a non-flammable, highly fluorinated methyl isopropyl ether, typically encountered as a clear, colorless liquid with a characteristic sweet odor. The compound is characterized by a molecular weight of 200.06 g/mol, a boiling point of 58.5 °C, and a vapor pressure of 197 mmHg at 26 °C [21]. Additionally, its dipole moment has been reported as 2.33 D [21]. The key physicochemical properties of sevoflurane are listed in Table 4.5, and its molecular structure is presented in Figure 4.9.

Beyond its established role as one of the most frequently employed inhalational anesthetics, sevoflurane has also attracted considerable attention in recent investigations, particularly with respect to its environmental impact, occupational safety, and clinical applications [119].

Table 4.5: Chemical properties of sevoflurane.

Property	Symbol	Value
Boiling point	T_b	58.5°C
Molar mass	M	200.06 g/mol
Vapor pressure	p_v	197 mmHg
Dipole moment	μ	2.33 D
Estimated gas kinetic diameter	D_{SF}	5.51 Å
Global warming potential	GWP	1980*

* Computed value for sevoflurane in relation to GWP of CO_2 for a 20-year time horizon.

In this section, experimental and theoretical results for electron scattering from the sevoflurane molecule are presented. Measurements were performed for incident electron energies between 50 and 300 eV and scattering angles from 25° to 125°. The experimental findings are compared with predictions of the IAM-SCAR+I model, ensuring reliability of the data. Along with DCSs, corresponding integral and momentum transfer cross sections are also reported over the same energy range [13].

Anhydrous sevoflurane ($C_4H_3F_7O$), with a stated purity above 99%, was employed as the target gas. Its preparation and introduction into the scattering chamber followed the same

procedure as previously described for isoflurane and halothane, including several freeze–pump–thaw cycles and admission via a heated gas line and needle to ensure stable vapor pressure. The base chamber pressure was typically 5×10^{-7} mbar, rising by roughly an order of magnitude during measurements.

For sevoflurane, the same relative flow procedure as for isoflurane and halothane was applied. Using the gas kinetic diameters of argon ($D_{\mathrm{Ar}} = 3.58$ Å) and sevoflurane ($D_{\mathrm{SF}} = 5.51$ Å), the pressure ratio $p_{\mathrm{Ar}} : p_{\mathrm{SF}} \approx 2.4$ was maintained. Absolute reference points were recorded at scattering angles of 40° and 80–100°, depending on the energy.

Sevoflurane differential cross sections were determined following the same methodology as for isoflurane, as detailed in the PhD thesis of E. Lange [31], which provides the only available reference for comparison. Measurements covered incident energies from 10 to 50 eV and scattering angles between 8° and 70°, with the absolute scale normalized to IAM-SCAR+I at 20°. The experimental results showed satisfactory agreement with theoretical predictions.

4.3.1 Differential Cross Sections

Absolute differential cross sections (DCSs) for elastic electron scattering from sevoflurane were determined at incident electron energies of 50, 100, 150, 200, 250, and 300 eV, as shown in Fig. 4.14. The presented data include experimentally obtained angular distributions, normalized to an absolute scale using selected reference points derived via the relative flow method. These reference values ensure internal consistency of the dataset and enable a reliable comparison with theoretical predictions, which are also displayed in the figure.

It should be emphasized that the absolute reference points obtained via the relative flow method show excellent agreement with the corresponding relative DCS values to which they are normalized. In the normalization procedure, one reference point is used to scale the relative angular distribution to an absolute level, while the second serves as an internal consistency check of the angular dependence. The observed agreement of this second reference point, within the experimental uncertainties, with the corresponding relative DCS value at the same scattering angle confirms the reliability of the measured angular distributions and the validity of the normalization procedure. A numerical summary of the experimentally determined absolute cross sections is provided in Table 4.5.

A systematic deviation between the experimental and theoretical DCSs is observed at small scattering angles. This discrepancy can be attributed to the instability of the interaction volume at those angles during the experiment, which leads to an underestimation of the measured electron signal in the forward direction. Consequently, the experimental DCS values in this angular region are systematically lower than the corresponding theoretical predictions. Since small-angle scattering makes the dominant contribution to the integral cross section (ICS), this effect results in somewhat lower experimental ICS values compared to theory, although their overall energy dependence remains consistent.

A more pronounced discrepancy between experiment and theory is observed at an incident energy of 150 eV, particularly at intermediate and larger scattering angles in the range from approximately 80° to 125°, where the experimental data points are systematically lower than the theoretical predictions. As can be seen in Fig. 4.14, this deviation is more significant than at other energies and suggests a reduced scattered intensity in this angular region. This effect may be related to increased experimental uncertainties at larger angles, where the electron count rate is lower and the influence of background subtraction becomes more pronounced. Since scattering at intermediate and large angles contributes significantly to the momentum-transfer cross section (MTCS), this discrepancy leads to lower experimental MTCS values at 150 eV, as will be discussed in the following subsection.

Note that, under the present experimental conditions, rotational excitations cannot be

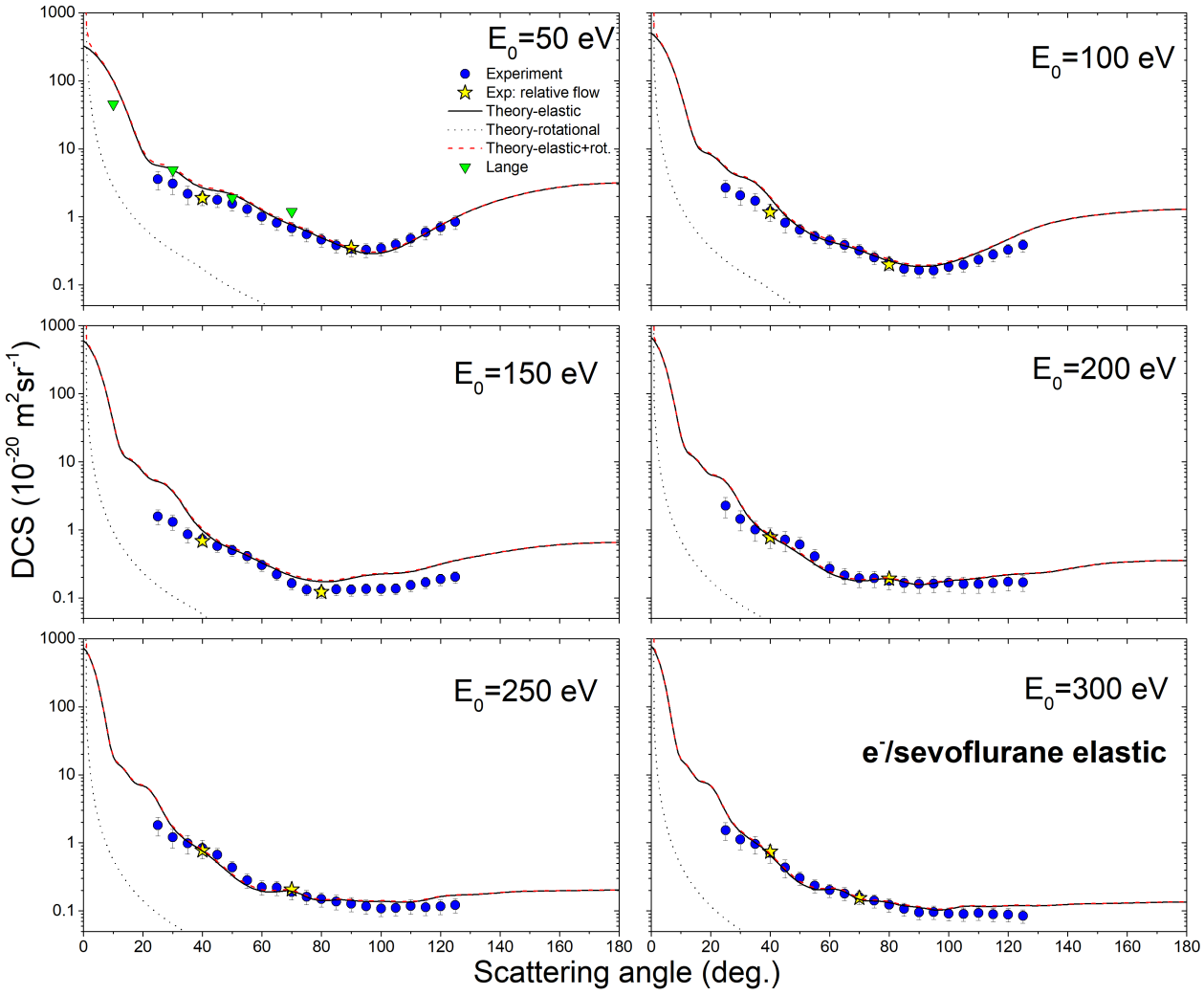

Figure 4.10: Absolute differential cross sections for elastic electron scattering from the sevoflurane molecule are shown at incident electron energies of 50, 100, 150, 200, 250, and 300 eV. The present experimental data are plotted as circles (blue online), while theoretical results are represented by a solid black curve for elastic DCSs, black dots for rotational DCSs, and a red dashed line for their combined, quasi-elastic contribution. Absolute reference points determined using the relative flow method are indicated by yellow stars, and previously reported experimental data by Lange [31] at 50 eV are shown as green triangles.

separated from purely elastic scattering. Therefore, as already discussed in the case of isoflurane (Section 4.2.1), the measured data correspond to the "quasi-elastic" cross sections. For a consistent comparison with theory, these results are confronted with the sum of calculated elastic and rotational contributions, which is shown by the red dashed line in Fig.4.14.

With regard to the normalization procedure, the relative flow method (RFM) was employed to place the measured angular distributions on an absolute scale. In this approach, argon was used as a reference gas, and its absolute differential cross sections (DCSs) were taken from the literature. Specifically, the recommended values reported by Ranković et al. [96] were adopted for incident electron energies in the range 50–200 eV and at 300 eV, while for the energy of 250 eV, where no corresponding data from the same experimental setup are available, the values from Williams and Willis [93] were used.

It should be noted that the reference datasets were obtained using different normalization procedures. Ranković et al. [96] employed helium as a reference gas within the relative flow

framework, while Williams and Willis [93] normalized their data through phase-shift analysis of relative angular distributions in the vicinity of the $^2P_{3/2,1/2}$ of argon. Despite these methodological differences, the reported absolute DCS values are consistent within the stated experimental uncertainties, as discussed in Ref. [120]. Given that the present normalization is also based on the RFM and that the measurements of Ranković et al. were performed using the same electron spectrometer (UGRA), their dataset was preferentially used wherever possible.

A comparison of the present sevoflurane DCS results with those reported by Lange [31] was performed at an incident electron energy of 50 eV, as this represents the only available overlap between the two datasets. Overall, a reasonable level of agreement is observed within the common angular range (8°–70°). In particular, at the intermediate angle of 50°, the present results are in very good agreement with the data of Lange, falling within the quoted experimental uncertainties.

At smaller and larger scattering angles, however, systematic deviations are observed. At 30°, the values reported by Lange are higher than the present results, which may be partly attributed to the previously discussed underestimation of the signal at small angles in the present experiment. On the other hand, at 70°, our results tend to agree better with the corresponding theoretical predictions used for normalization in the work of Lange, while the experimental values of Lange remain systematically higher.

Different normalization procedures were used in the two studies, which may partly account for the observed discrepancies between the datasets.

4.3.2 Integral and Momentum Transfer Cross Sections

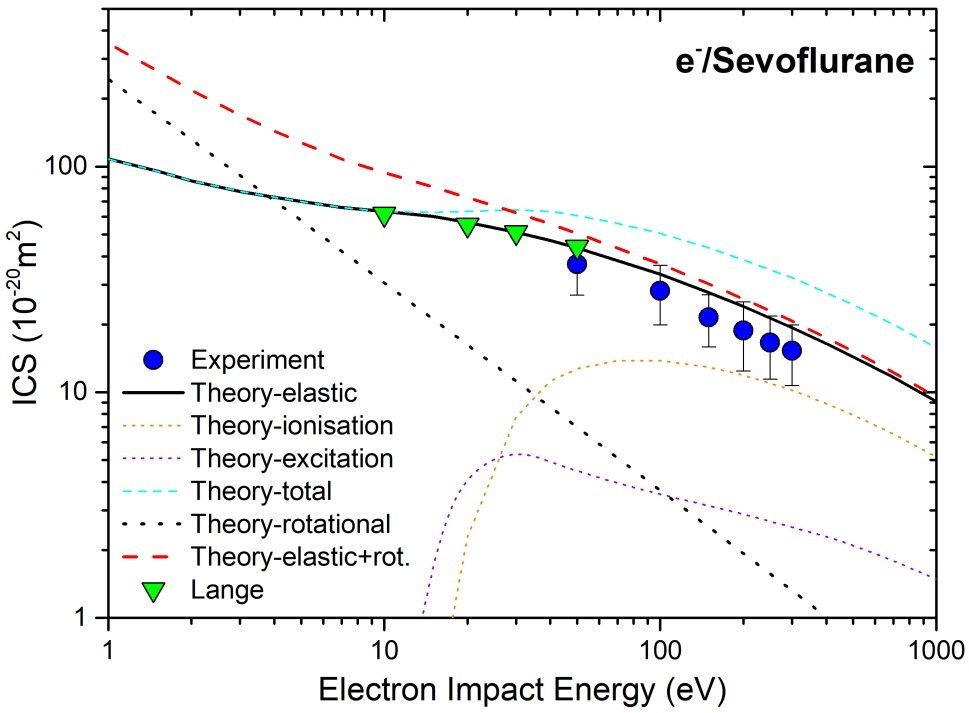

Figure 4.11: Integral cross sections for elastic electron scattering from the sevoflurane molecule. The present experimental data are shown as blue circles, while the theoretical results are represented by the solid black curve for purely elastic ICSs and the red dashed curve for quasi-elastic ICSs. The figure also includes theoretical total, rotational, excitation, and ionization cross sections, as well as experimental data points reported by Lange [31].

Figure 4.15 shows the experimental and theoretical integral cross sections (ICSs) for electron scattering from sevoflurane. The presented experimental data include the present elastic ICSs covering incident electron energies from 50 to 300 eV, together with previously published results by Lange [31] in the energy range of 10 to 50 eV. The theoretical curves account for elastic scattering, ionisation and excitation processes, total cross sections, as well as rotational contributions, including both purely elastic and elastic-plus-rotational components.

As shown in Fig. 4.15, the experimental ICS values exhibit a smooth decrease with increasing incident electron energy over the investigated range. This behaviour is characteristic of electron scattering from polyatomic molecules and reflects the reduced scattering probability at higher energies. The present experimental data are in good overall agreement with the theoretical elastic cross sections, particularly in terms of the energy dependence. Compared to previously analysed ICS results for halothane and isoflurane, the present experimental ICSs for sevoflurane show improved agreement with theory in terms of the overall shape of the energy dependence, although they remain systematically lower in absolute magnitude.

This systematic offset can be traced back to the underestimation of the forward-angle scattering intensity due to instability of the interaction volume, as discussed in the DCS analysis. Since the small-angle region provides the dominant contribution to the ICS, this limitation directly propagates into the integrated cross sections. Nevertheless, the good agreement in the overall trend indicates that the essential features of the scattering process are well reproduced.

The inclusion of rotational contributions in the theoretical model (red dashed curve) leads to an increase in the predicted cross sections, particularly at lower energies where dipole-driven rotational excitations are more pronounced, consistent with the polar character of the sevoflurane molecule. The rotational contribution (black dotted curve) decreases rapidly with increasing energy and becomes negligible at higher energies compared to the elastic channel.

Theoretical results further show that, over the majority of the investigated energy range, elastic scattering remains the dominant contribution to the total cross section. This emphasizes the importance of the present experimental data, as they provide reliable benchmark values for the leading scattering process.

In addition, the calculated inelastic channels, including ionisation (orange dotted curve) and electronic excitation (purple dotted curve), become increasingly significant with rising electron energy. Consequently, the total cross section (cyan dashed curve) exceeds the purely elastic contribution, particularly above $\sim$50 eV.

A comparison with the experimental data reported by Lange [31] shows very good agreement at the only overlapping energy of 50 eV. At this point, the present experimental value is consistent with the data of Lange within the experimental uncertainties, providing mutual validation of the two independent measurements. The present results therefore offer a seamless extension of the existing dataset toward higher energies (50–300 eV), while preserving the overall trend in energy dependence. Any minor discrepancies can be attributed to differences in experimental conditions and normalization procedures.

Figure 4.16 shows the experimental and theoretical momentum-transfer cross sections for electron scattering from sevoflurane. The presented experimental data include the present MTCS values obtained in the incident electron energy range from 50 to 300 eV. The theoretical curves correspond to purely elastic scattering (solid black line), rotational contributions (black dotted line), and the combined elastic-plus-rotational cross sections (red dashed line).

As can be seen from Fig. 4.16, the experimental MTCS values exhibit a decreasing trend with increasing electron energy, consistent with the behaviour observed for the integral cross sections. Overall, good agreement between experiment and theory is observed across most of the investigated energy range, particularly at low energy of 50 eV, where the experimental value lies close to both the elastic and elastic-plus-rotational theoretical predictions.

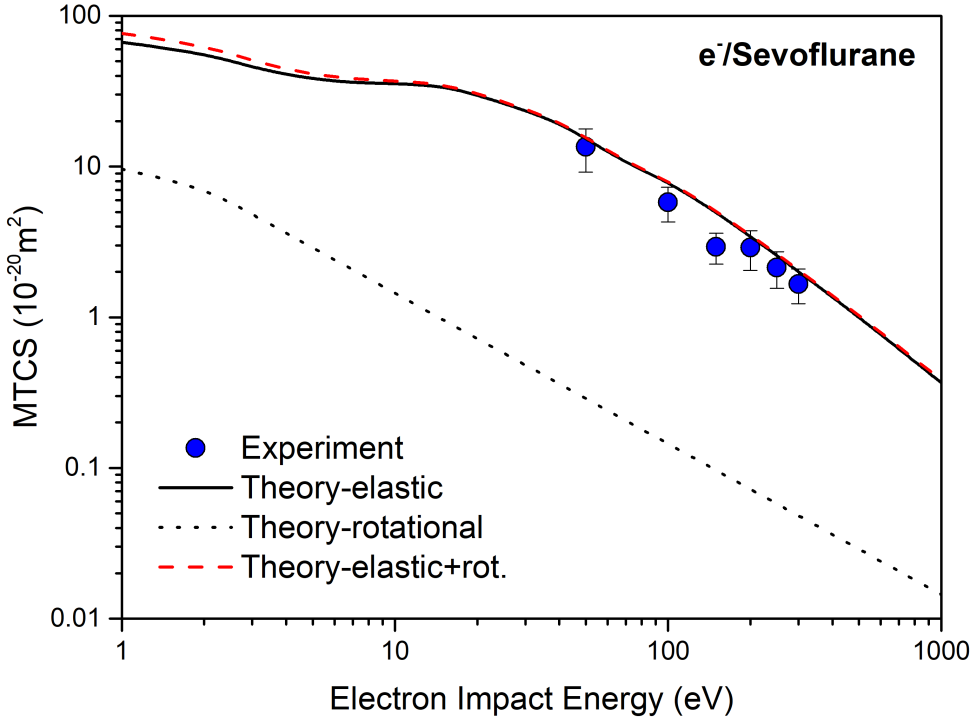

Figure 4.12: Momentum transfer cross sections for elastic electron scattering from the sevoflurane molecule. The present experimental results (blue circles) are compared with theoretical predictions, including purely elastic (solid black line) and quasi-elastic (red dashed line) contributions.

A more pronounced deviation is observed at 150 eV, where the experimental MTCS value is noticeably lower than the corresponding theoretical results. This behaviour is consistent with the discrepancy identified in the DCS analysis, where reduced experimental intensities were observed at intermediate and larger scattering angles. Since these angular regions contribute significantly to the MTCS, the underestimation of the DCSs directly propagates into lower MTCS values at this energy. At higher energies (200–300 eV), the agreement improves again, with the experimental data following the theoretical trend within the estimated uncertainties, although remaining slightly lower in magnitude.

The rotational contribution to the MTCS (black dotted curve) decreases rapidly with increasing energy and becomes negligible compared to the elastic component above approximately 10 eV. Consequently, the difference between the purely elastic and elastic-plus-rotational theoretical curves becomes small at higher energies, indicating that the MTCS is dominated by elastic scattering in this regime.

It should be noted that, to the best of our knowledge, no other experimental or theoretical MTCS data for electron scattering from sevoflurane are available in the literature. Therefore, the present results represent the first dataset of this kind and provide valuable benchmark information for future studies.

Table 4.6: Experimental results for absolute differential cross-sections (DCSs), integral and momentum transfer cross-sections (ICSs and MTCSs, respectively), later two in unit $10^{-20}\,\mathrm{m}^2$, for elastic electron scattering from sevoflurane. In parentheses are given absolute uncertainties of the last two digits.

	DCS ($10^{-20}\,\mathrm{m}^2\mathrm{sr}^{-1}$)					
$\theta\,(^\circ)$	50 (eV)	100 (eV)	150 (eV)	200 (eV)	250 (eV)	300 (eV)
25	3.6(1.1)	2.67(76)	1.57(39)	2.25(74)	1.82(56)	1.53(45)
30	3.07(93)	2.07(59)	1.31(32)	1.44(48)	1.20(37)	1.12(33)
35	2.17(66)	1.72(49)	0.86(21)	1.01(33)	0.99(30)	0.96(28)
40	1.89(43)	1.20(34)	0.72(14)	0.80(26)	0.84(26)	0.72(21)
45	1.77(40)	0.81(23)	0.58(11)	0.71(24)	0.67(16)	0.43(13)
50	1.57(36)	0.64(14)	0.499(94)	0.61(16)	0.43(10)	0.304(66)
55	1.31(30)	0.52(11)	0.407(77)	0.41(11)	0.282(67)	0.235(51)
60	1.01(23)	0.449(98)	0.304(57)	0.270(71)	0.223(53)	0.202(44)
65	0.82(18)	0.387(84)	0.222(42)	0.214(57)	0.220(52)	0.180(39)
70	0.68(15)	0.322(70)	0.163(31)	0.194(51)	0.189(45)	0.160(35)
75	0.55(13)	0.255(56)	0.133(25)	0.195(51)	0.162(38)	0.141(31)
80	0.47(11)	0.214(47)	0.122(23)	0.179(47)	0.150(36)	0.122(27)
85	0.380(86)	0.173(38)	0.133(25)	0.165(44)	0.139(33)	0.107(24)
90	0.339(77)	0.165(36)	0.132(25)	0.160(43)	0.127(30)	0.095(21)
95	0.327(74)	0.162(35)	0.136(26)	0.162(44)	0.117(28)	0.096(21)
100	0.347(79)	0.184(40)	0.135(25)	0.167(44)	0.109(26)	0.091(20)
105	0.396(90)	0.197(43)	0.137(26)	0.160(42)	0.111(27)	0.090(21)
110	0.48(11)	0.236(51)	0.153(29)	0.160(42)	0.118(28)	0.093(20)
115	0.59(13)	0.279(61)	0.169(32)	0.165(44)	0.113(27)	0.089(20)
120	0.71(16)	0.327(71)	0.188(35)	0.173(46)	0.116(28)	0.088(20)
125	0.85(19)	0.385(84)	0.202(38)	0.170(45)	0.122(29)	0.085(19)
ICS	37(10)	28.2(8.3)	21.5(5.6)	18.8(6.4)	16.6(5.2)	15.3(4.6)
MTCS	13.5(4.3)	6.1(1.5)	3.09(68)	2.90(85)	2.14(58)	1.66(43)

4.4 Desflurane

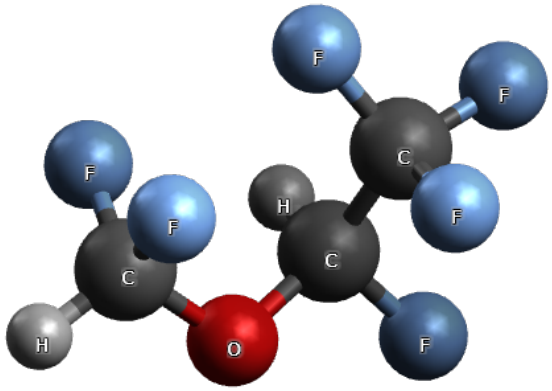

Figure 4.13: Schematic representation of the molecular structure of desflurane, highlighting the spatial configuration of its constituent fluorine, hydrogen, carbon, and oxygen atoms.

Desflurane (I-653, 2-(difluoromethoxy)-1,1,1,2-tetrafluoroethane, $C_3H_2F_6O$) is a modern volatile inhalation anesthetic widely used in clinical practice due to its rapid onset and very fast elimination from the human body. In comparison with earlier halogenated agents such as methoxyflurane, sevoflurane, enflurane, and isoflurane, desflurane undergoes minimal metabolic degradation, which contributes to its highly favorable pharmacokinetic characteristics.

The compound is a colorless liquid with a molecular weight of 168.04 g/mol, a low boiling point of 23.5 °C, and a high vapor pressure of approximately 700 mmHg at 22–23 °C [121]. Its dipole moment has been reported as 3.39 D (theoretical) and 2.87 D (experimental) [122]. The main physicochemical properties of desflurane are summarized in Table 4.7, while its molecular structure is shown in Figure 4.13.

Beyond its established clinical use as a widely applied inhalational anesthetic, desflurane has recently received increased attention due to its environmental impact. Owing to its extremely low metabolic rate (0.02%), the compound is almost entirely exhaled unchanged into the atmosphere [123]. Together with its long atmospheric lifetime of 8.9–21.4 years [9–11], this leads to high environmental persistence. Consequently, desflurane exhibits the highest global warming potential among commonly used anesthetics, with a 20-year GWP of 3714 relative to CO_2 [6].

Table 4.7: Chemical properties of desflurane.

Property	Symbol	Value
Boiling point	T_b	23.5°C
Molar mass	M	168.04 g/mol
Vapor pressure	p_v	700 mmHg
Dipole moment (theoretical/exp.)	μ	3.39 / 2.87 D
Estimated gas kinetic diameter	D_{DF}	5.8 Å
Global warming potential	GWP	3714*

* Computed value for desflurane in relation to CO_2 over a 20-year time horizon.

This section presents both experimental and theoretical results for electron scattering from the desflurane molecule. The measurements cover incident electron energies in the range from 50 to 300 eV and scattering angles between 25° and 125°. The obtained data are benchmarked

against calculations within the IAM-SCAR+I framework, providing a consistent basis for validation of the experimental results. In addition to differential cross sections, the corresponding integral and momentum transfer cross sections are also reported over the same energy interval [**?**].

Anhydrous desflurane with a stated purity above 99% was used as the target gas. It was introduced into the scattering chamber from a glass reservoir via a gas handling line and a needle inlet. Under optimal vacuum conditions, the base pressure was approximately 6×10^{-7} mbar, increasing by about one order of magnitude during measurements.

For desflurane, the relative flow method was applied in the same manner as for isoflurane and halothane. Using the kinetic diameters of argon ($D_{\mathrm{Ar}} = 3.58$ Å) and desflurane ($D_{\mathrm{DF}} = 5.8$ Å), a pressure ratio of approximately $p_{\mathrm{Ar}} : p_{\mathrm{DF}} \approx 2.6$ was maintained. Absolute normalization was performed using two reference angles, typically 40° and 70°–90°, depending on the incident energy.

Unlike the previously studied molecules (halothane, sevoflurane, and isoflurane), for which corresponding experimental datasets are available for comparison, no prior differential cross section measurements have been reported for desflurane. Consequently, the present results constitute the first systematic experimental study of electron scattering from this molecule over the investigated energy and angular ranges.

4.4.1 Differential Cross Sections

In the case of desflurane, absolute differential cross sections for elastic electron scattering were determined at incident energies of 50, 100, 150, 200, 250, and 300 eV. The results are presented in Fig. 4.14 (orange circles), together with the directly measured reference points at selected scattering angles (40° and either 70°, 80°, or 90°), indicated by blue stars. These reference points were obtained using the relative flow technique and served to normalize the relative measurements to an absolute scale, ensuring consistency between independently acquired datasets.

It should be noted that at the incident energy of 300 eV only a single reference point was obtained. The measurement at the second reference angle could not be performed because the electron signal was extremely weak, resulting in an insufficient count rate for reliable normalization. Nevertheless, the available normalization point allowed the relative data to be placed on an absolute scale. A comparison with theoretical predictions is also included in Fig. 4.14, providing additional validation of the experimental procedure. A numerical summary of the resulting absolute differential cross sections is given in Table 4.8.

As shown in Fig. 4.14, the experimentally determined differential cross sections for desflurane are generally in good agreement with the corresponding theoretical predictions. In particular, excellent agreement is observed at incident electron energies between 100 and 200 eV. At 50 eV, the experimental and theoretical results are consistent on an absolute scale in terms of magnitude; however, noticeable differences in the angular dependence are present, indicating a different shape of the angular distribution.

Furthermore, at 300 eV the measured DCSs are systematically lower than the calculated values in the angular range between 70° and 125°, which leads to reduced values of the corresponding momentum-transfer cross sections (MTCSs). A possible explanation for this discrepancy is that, during the measurements, the electron count rate at larger scattering angles decreased significantly, while the relative contribution of the background signal became more pronounced. This may have reduced the accuracy of the extracted cross sections in this angular region. In addition, at this energy only a single relative-flow absolute point was available for normalization, which could further contribute to the observed disagreement at 300 eV.

On the other hand, theoretical calculations may also exhibit increased uncertainty at medium

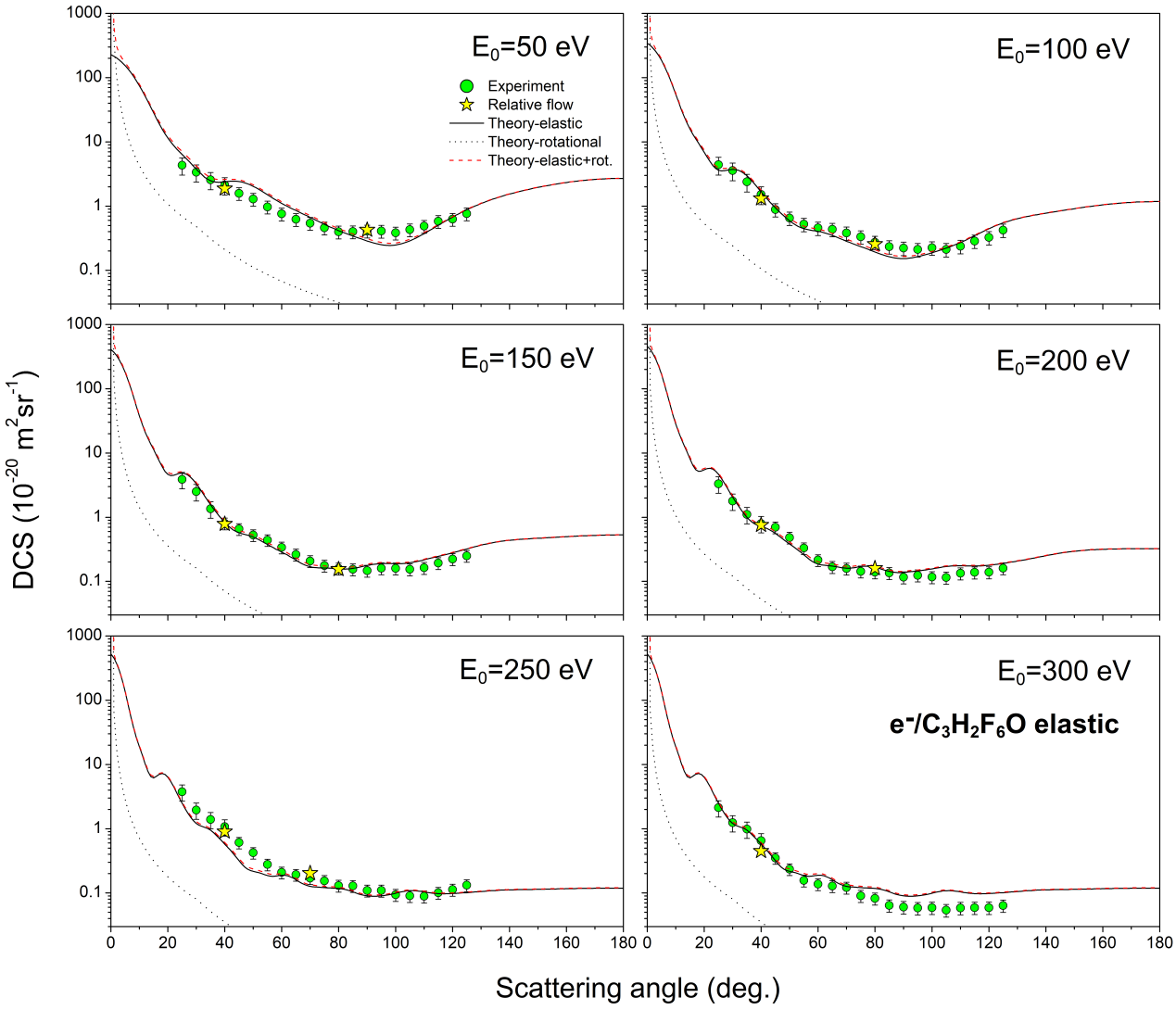

Figure 4.14: Elastic differential cross sections for electron scattering from desflurane measured at incident energies of 50, 100, 150, 200, 250, and 300 eV. Experimental data are represented by open circles (orange online), while the theoretical results are shown as a solid black line (elastic), black dots (rotational), and a red dashed line indicating the combined quasi-elastic contribution. The normalization points obtained via the relative flow method are denoted by blue star symbols.

and large scattering angles for molecules with a significant permanent dipole moment, such as desflurane [122]. This limitation, although partly mitigated by the correction proposed by Dickinson [83], may additionally contribute to the observed discrepancies between experiment and theory in this angular region.

Under the present experimental conditions, rotationally inelastic and purely elastic events cannot be experimentally separated; therefore, the measured cross sections correspond to quasi-elastic scattering. The comparison with theory is thus performed using the sum of elastic and rotational contributions.

For consistency with the previously studied molecules—sevoflurane, isoflurane, and halothane—the same approach is adopted here. Among all four systems, desflurane exhibits the largest permanent dipole moment, and consequently the most pronounced rotational contribution. This effect is most clearly observed at 50 eV in the forward scattering region, where the enhancement due to rotational scattering is strongest compared to the other investigated molecules.

Furthermore, the angular behavior of the measured differential cross sections (DCSs) follows trends typically observed for molecular targets and is consistent with previous studies reported in the literature [?,?,?]. At incident electron energies of 50 and 100 eV, the angular distributions display a broad minimum near 100°, which gradually becomes less pronounced as the incident energy increases.

At higher energies, the measured DCSs begin to exhibit an angular dependence resembling Rutherford-type behavior. In particular, the cross sections become strongly enhanced in the forward direction, indicating the increasing importance of small-angle scattering. At the same time, for larger scattering angles (above approximately 80°), the DCSs tend to level off and show only weak angular variations. Such behavior is characteristic of electron scattering from molecular systems at intermediate and higher energies, where the interaction is increasingly dominated by the long-range Coulomb potential and the independent atom approximation becomes progressively more applicable.

4.4.2 Integral and Momentum Transfer Cross Sections

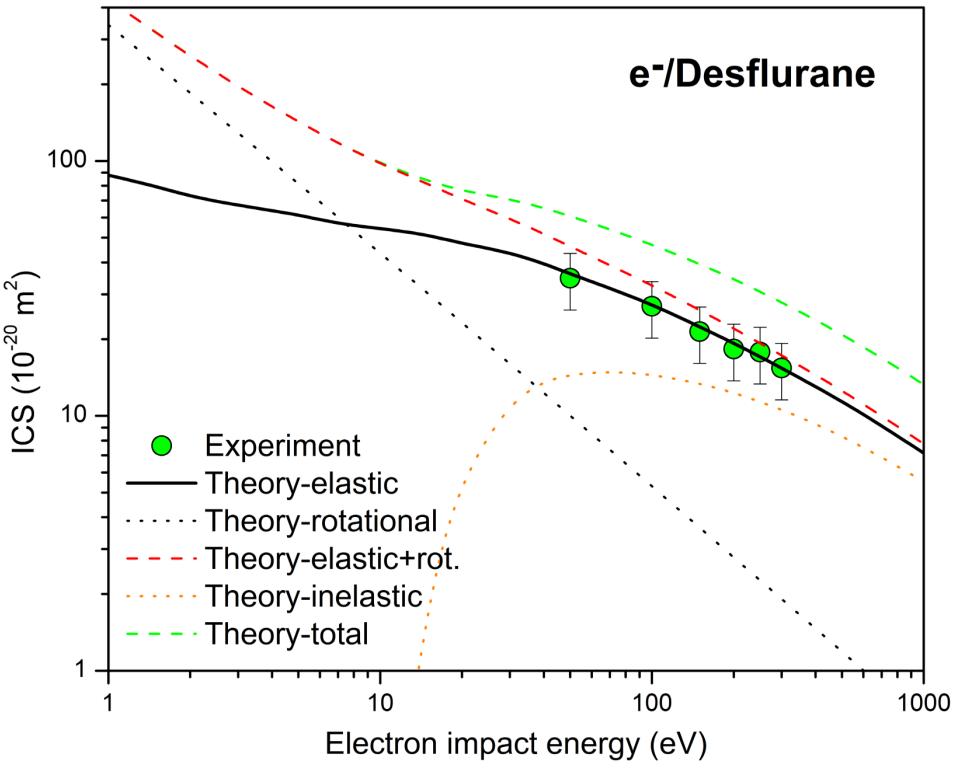

Figure 4.15: Integral cross sections (ICSs) for electron scattering from desflurane. The experimental results obtained in the present work are shown as orange circles, while theoretical predictions are given by the solid black line for elastic ICSs and the red dashed line for quasi-elastic ICSs. Additional theoretical curves for total, rotational, excitation, and ionization cross sections are also included.

The energy dependence of the integral cross section (ICS) for electron scattering from desflurane is shown in Fig. 4.15. The experimental data (green circles), obtained at incident electron energies in the range from 50 to 300 eV, exhibit a smooth decrease with increasing energy, which is typical for electron scattering from polyatomic molecules.

The experimental ICS values were obtained by integrating the measured differential cross sections over the full angular range. Since the measurements were limited to scattering angles

between 25° and 125°, the angular distributions were extrapolated toward the forward (0°) and backward (180°) directions using theoretical angular behavior, as described in Section 3.3.3. To ensure consistency, the calculated DCSs were normalized to the experimental absolute values prior to integration. As a result, the derived ICS values listed in Table 4.8 retain some dependence on the extrapolation procedure and carry an estimated uncertainty of approximately 25%.

A comparison between experiment and theory shows excellent agreement with the calculated purely elastic ICS (solid black line), which reproduces both magnitude and energy dependence. The inclusion of rotational excitation channels (red dashed line) leads to a systematic increase of the predicted cross sections, particularly at lower energies where dipole-induced rotational transitions are more significant due to the polar character of desflurane. The rotational contribution is shown separately by the dotted black curve. Among all investigated molecules—sevoflurane, isoflurane, halothane, and desflurane—this agreement is the best, both in terms of the overall shape of the energy dependence and the absolute values of the cross sections.

The calculated inelastic contribution (orange dotted line) becomes noticeable above approximately 10 eV. When all contributions are combined, the resulting total cross section (green dashed line) lies above the experimental elastic ICS values, as expected.

The energy dependence of the momentum-transfer cross section (MTCS) for electron scattering from desflurane is presented in Fig. 4.16. The experimental values (green circles) were obtained using the same extrapolated angular distributions as for the ICS analysis.

Overall, the experimental MTCS values show very good agreement with the theoretical predictions. The theoretical curves reproduce both magnitude and energy dependence across the investigated range. The experimental MTCS values, listed in Table 4.8, carry an estimated uncertainty of approximately 25%.

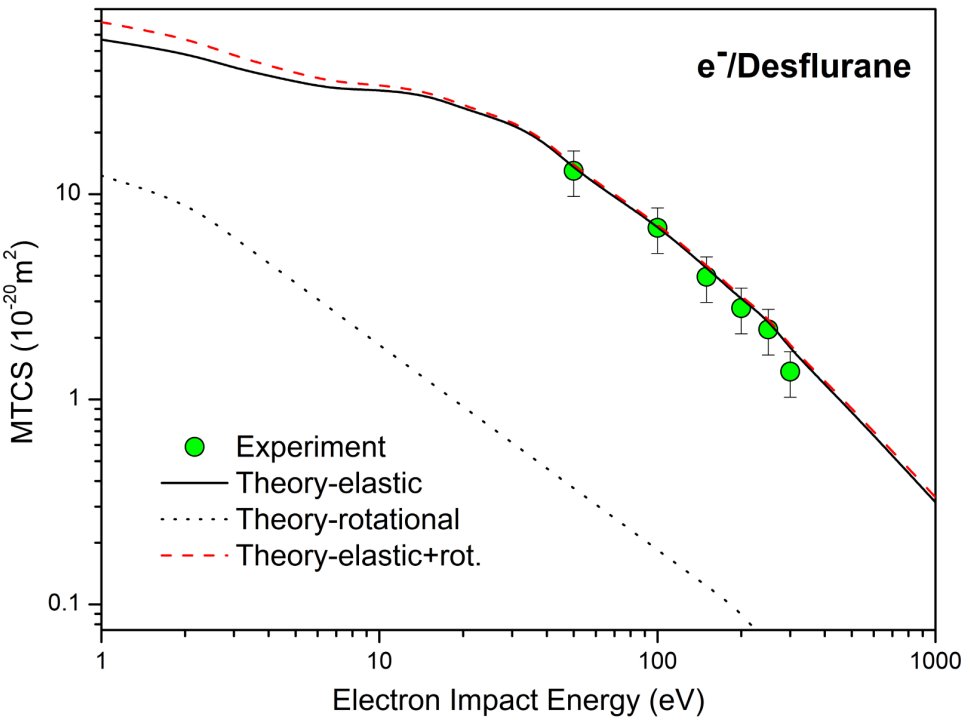

Figure 4.16: Momentum-transfer cross sections for electron scattering from desflurane. The present experimental data are shown as orange circles and compared with theoretical results, including the elastic contribution (solid black line) and the quasi-elastic cross section (red dashed line).

A noticeable deviation is observed at the highest energy of 300 eV, where the experimental MTCS is somewhat lower than the calculated one. This is consistent with the systematic reduction of the measured DCS values at large scattering angles discussed above.

These new measurements fill a significant gap in the currently available experimental and theoretical data for desflurane, providing, to the best of our knowledge, the first set of absolute differential, integral, and momentum-transfer cross sections in the intermediate-to-high incident electron energy range of 50–300 eV.

Table 4.8: Experimental results for absolute differential cross-sections (DCSs), integral and momentum transfer cross-sections (ICSs and MTCSs, respectively), latter two in units of $10^{-20}\,\mathrm{m}^2$, for elastic electron scattering from desflurane. In parentheses are given absolute uncertainties of the last two digits.

	DCS ($10^{-20}\,\mathrm{m}^2\mathrm{sr}^{-1}$)					
$\theta\,(^\circ)$	50 (eV)	100 (eV)	150 (eV)	200 (eV)	250 (eV)	300 (eV)
25	4.3(1.3)	4.4(1.4)	3.9(1.1)	3.31(95)	3.8(1.1)	2.13(60)
30	3.4(1.0)	3.6(1.1)	2.52(72)	1.79(51)	1.96(55)	1.24(35)
35	2.57(77)	2.39(74)	1.35(39)	1.10(32)	1.39(39)	0.99(28)
40	2.13(64)	1.52(47)	0.80(17)	0.80(23)	1.07(30)	0.65(19)
45	1.58(35)	0.88(21)	0.66(14)	0.70(14)	0.61(12)	0.351(72)
50	1.29(29)	0.65(15)	0.53(11)	0.48(10)	0.422(86)	0.235(48)
55	0.97(22)	0.52(12)	0.441(91)	0.331(69)	0.278(57)	0.157(33)
60	0.76(17)	0.46(11)	0.339(70)	0.215(45)	0.209(43)	0.137(29)
65	0.62(14)	0.44(10)	0.262(55)	0.168(35)	0.192(40)	0.128(27)
70	0.54(12)	0.382(90)	0.208(43)	0.158(33)	0.170(35)	0.121(26)
75	0.46(10)	0.333(78)	0.176(37)	0.143(30)	0.155(32)	0.091(19)
80	0.399(90)	0.273(65)	0.159(33)	0.139(30)	0.130(27)	0.082(18)
85	0.400(90)	0.234(55)	0.154(32)	0.135(29)	0.129(27)	0.064(14)
90	0.411(93)	0.222(53)	0.147(31)	0.116(25)	0.109(23)	0.060(13)
95	0.409(92)	0.212(50)	0.161(34)	0.124(26)	0.109(23)	0.058(13)
100	0.383(86)	0.224(53)	0.159(33)	0.117(25)	0.094(20)	0.059(13)
105	0.430(97)	0.212(50)	0.154(32)	0.115(25)	0.090(19)	0.054(12)
110	0.49(11)	0.237(56)	0.163(34)	0.134(28)	0.089(19)	0.059(13)
115	0.58(13)	0.286(68)	0.193(40)	0.138(29)	0.101(21)	0.059(13)
120	0.63(14)	0.325(77)	0.223(46)	0.139(29)	0.113(24)	0.059(13)
125	0.76(17)	0.42(10)	0.250(52)	0.160(34)	0.133(28)	0.064(14)
ICS	34.7(8.7)	26.9(6.7)	21.4(5.3)	18.3(4.6)	17.8(4.4)	15.4(3.8)
MTCS	13.0(3.3)	6.9(1.7)	3.96(99)	2.79(70)	2.19(55)	1.37(34)

Chapter 5

Final Remarks and Future Research Directions

This chapter summarizes the main findings of the present work and outlines possible directions for future research. The key results obtained from both experimental measurements and theoretical calculations are briefly discussed, with emphasis on their consistency and physical significance. Finally, potential improvements and extensions of the current study are identified, providing a basis for further investigations in this area.

5.1 Conclusions

This dissertation has presented a systematic experimental investigation of elastic electron scattering from four volatile halogenated anesthetic molecules — halothane, isoflurane, sevoflurane, and desflurane — in the intermediate electron energy range. Differential cross sections (DCSs) were measured using the crossed electron–molecular beam technique, and the corresponding integral cross sections (ICSs) and momentum transfer cross sections (MTCSs) were derived from the experimental data. The obtained results provide new insight into electron–molecule interactions in complex polyatomic systems of both biomedical and environmental relevance.

The measured angular distributions exhibit the characteristic strong forward scattering behavior expected for highly polarizable halogenated molecules. In all investigated systems, the DCSs increase significantly at small scattering angles, reflecting the important contribution of long-range polarization interactions and, in some cases, permanent dipole effects. At larger scattering angles, the cross sections decrease smoothly, while the angular structures become increasingly sensitive to molecular geometry, atomic composition, and interference effects.

A systematic comparison between the investigated molecules reveals clear trends associated with molecular structure and degree of halogen substitution. Halothane, containing both chlorine and bromine atoms, exhibits comparatively enhanced scattering contributions related to its larger polarizability and the presence of heavier halogen centers. Isoflurane and sevoflurane, as fluorinated ethers, show scattering characteristics governed primarily by strong fluorination and molecular dipole effects. Desflurane, despite being fully fluorinated and lacking chlorine or bromine atoms, still demonstrates pronounced forward scattering due to its large molecular size and high fluorine content.

The comparison between experimental data and theoretical predictions based mainly on the IAM-SCAR+I approach demonstrates overall very good agreement across the investigated energy range. The theoretical models successfully reproduce the general angular dependence and energy behavior of the measured cross sections, confirming that the Independent Atom Model with screening-corrected additivity rules and interference effects provides a reliable framework for describing elastic electron scattering from large halogenated polyatomic molecules at inter-

mediate energies. Small discrepancies observed at lower energies and small scattering angles likely originate from limitations associated with long-range correlation, polarization, and rotational excitation effects, which become increasingly important in polar molecular systems.

One of the important outcomes of this dissertation is the extension of the available experimental database for electron scattering from biologically and environmentally relevant anesthetic molecules. In particular, the present work provides, for the first time, experimental elastic scattering cross sections for desflurane, thereby filling a significant gap in the existing literature. These results constitute valuable benchmark data for future theoretical calculations and modelling efforts.

The derived ICS and MTCS data further contribute to the understanding of electron transport processes in complex molecular media. Such quantities are of considerable importance in modelling low- and intermediate-energy electron propagation in atmospheric environments, plasmas, radiation chemistry, and biologically relevant systems. Since volatile anesthetics are also greenhouse gases with non-negligible atmospheric impact, improved knowledge of their electron interaction properties may contribute to a better understanding of their degradation pathways and electron-induced atmospheric processes.

Overall, the results obtained in this dissertation demonstrate that elastic electron scattering from volatile anesthetic molecules is strongly influenced by molecular size, fluorination, halogen substitution, and permanent dipole moments. The study confirms the importance of combining high-quality experimental measurements with reliable theoretical approaches in order to achieve a comprehensive description of electron interactions with complex molecular targets.

The present work therefore represents a meaningful contribution to the broader field of atomic and molecular collision physics, while simultaneously providing data of relevance for atmospheric physics, environmental chemistry, medical physics, and related interdisciplinary research areas.

5.2 Future Research Directions

The results presented in this dissertation open several possibilities for future experimental and theoretical investigations of electron interactions with biologically and environmentally relevant molecules.

One important direction of future work involves extending the present experimental studies to additional anesthetic agents and related molecular systems. In particular, measurements of differential cross sections (DCSs), integral cross sections (ICSs), and momentum transfer cross sections (MTCSs) are planned for nitrous oxide (N_2O), which remains one of the most widely used inhalation anesthetics in modern clinical practice. Due to its atmospheric relevance as a strong greenhouse gas and its comparatively simple molecular structure, N_2O represents an important benchmark system for electron–molecule scattering studies. Such measurements would also enable systematic comparisons between simple inorganic anesthetic molecules and the more complex halogenated anesthetics investigated in the present work.

Future investigations will also focus on dissociative electron attachment (DEA) processes in a broader range of anesthetic molecules. Particular attention will be devoted to the identification of fragmentation pathways, resonance structures, and transient negative ion formation induced by low-energy electron impact. These studies are expected to provide valuable insight into electron-driven molecular decomposition mechanisms, which are relevant for atmospheric degradation processes, plasma chemistry, and radiation-induced damage mechanisms.

In addition to experimental work, further theoretical developments are required for a more complete description of electron scattering from complex polyatomic systems. Improved theoretical treatments including more accurate polarization potentials, rotational excitation effects,

and correlation contributions would be particularly important at lower electron energies and small scattering angles, where deviations between experiment and theory become more pronounced. The availability of new experimental benchmark data will therefore remain essential for testing and refining future theoretical models.

Another promising direction involves extending the investigated energy range toward both lower and higher electron energies. Low-energy studies are especially important because resonance phenomena and electron attachment processes become dominant in this regime, while higher-energy measurements could provide additional information on the validity limits of existing scattering approximations and additivity-rule-based approaches.

Overall, future investigations of electron scattering and electron-induced fragmentation processes in anesthetic molecules are expected to contribute further to the understanding of collision dynamics in complex halogenated systems and to provide data of relevance for molecular physics, atmospheric chemistry, plasma applications, and environmental studies.

Bibliography

[1] E. Temple and M. Wiles, "Inhalational anaesthetic agents," *Anaesth. Intensive Care Med.*, vol. 20, no. 2, pp. 109–117, 2019.

[2] R. Jones, "A history of inhaled anesthetics," in *The Wondrous Story of Anesthesia* (E. I. Eger, L. J. Saidman, and R. N. Westhorpe, eds.), pp. 609–628, Springer, 2014.

[3] F. X. Whalen, D. R. Bacon, and H. M. Smith, "Inhaled anesthetics: an historical overview," *Best Pract. Res. Clin. Anaesthesiol.*, vol. 19, no. 3, pp. 323–330, 2005.

[4] C. W. Suckling, "Some chemical and physical factors in the development of fluothane," *Br J Anaesth.*, vol. 29, no. 10, pp. 466–472, 1957.

[5] I. Smith, M. Nathanson, and P. F. White, "Sevoflurane-a long-awaited volatile anaesthetic," *Br J Anaesth.*, vol. 76, no. 3, pp. 435–445, 1996.

[6] Y. Ishizawa, "Special article: General anesthetic gases and the global environment," *Anesth. Analg.*, vol. 112, no. 1, pp. 213–217, 2011. Review on the environmental impact of anesthetic gases.

[7] K. S. Khan, I. Hayes, and D. J. Buggy, "Pharmacology of anaesthetic agents ii: inhalation agents," *Continuing Education in Anaesthesia, Critical Care & Pain*, vol. 14, no. 3, pp. 106–111, 2014.

[8] J. Vukalović, B. P. Marinković, J. Rosado, F. Blanco, G. García, and J. B. Maljković, "Investigating theoretical and experimental cross sections for elastic electron scattering from isoflurane," *Phys. Chem. Chem. Phys.*, vol. 26, pp. 985–991, 2024.

[9] S. M. Ryan and C. J. Nielsen, "Global warming potential of inhaled anesthetics application to clinical use .," *Anesth. Analg.*, vol. 111, no. 1, pp. 92–98, 2010.

[10] T. Langbein, H. Sonntag, D. Trapp, A. Hoffmann, W. Malms, E. P. Röth, V. Mörs, and R. Zellner, "Volatile anaesthetics and the atmosphere: atmospheric lifetimes and atmospheric effects of halothane, enflurane, isoflurane, desflurane and sevoflurane.," *Br. J. Anaesth.*, vol. 82, no. 1, p. 66–73, 1999.

[11] M. P. Sulbaek Andersen, S. P. Sander, O. J. Nielsen, D. S. Wagner, T. J. Sanford, Jr, and T. J. Wallington, "Inhalation anaesthetics and climate change.," *Br J Anaesth.*, vol. 105, no. 6, pp. 760–766, 2010.

[12] A. C. Brown, C. E. Canosa-Mas, A. D. Parr, J. M. T. Pierce, and R. P. Wayne, "Tropospheric lifetimes of halogenated anaesthetics.," *Nature*, vol. 341, p. 635–637, 1989.

[13] J. Vukalović, J. B. Maljković, F. Blanco, G. García, B. Predojević, and B. P. Marinković, "Absolute differential cross-sections for elastic electron scattering from sevoflurane molecule in the energy range from 50–300 ev," *Int. J. Mol. Sci.*, vol. 23, no. 1, 2022.

[14] B. Boudaïffa, P. Cloutier, D. Hunting, M. A. Huels, and L. Sanche, "Resonant formation of dna strand breaks by low-energy electrons," *Science*, vol. 287, pp. 1658–1660, 2000.

[15] L. Campbell and M. Brunger, "Electron collisions in atmospheres," *Int. Rev. Phys. Chem.*, vol. 35, no. 2, pp. 297–351, 2016.

[16] L. Campbell and M. J. Brunger, "Modelling of energy-dependent electron interactions in the earthrsquo;s mesosphere," *Atmosphere*, vol. 14, no. 4, pp. 1–17, 2023.

[17] F. F. da Silva, D. Duflot, S. V. Hoffmann, N. C. Jones, F. N. Rodrigues, A. M. Ferreira-Rodrigues, G. G. B. de Souza, N. J. Mason, S. Eden, and P. Limão-Vieira, "Electronic state spectroscopy of halothane as studied by ab initio calculations, vacuum ultraviolet synchrotron radiation, and electron scattering methods," *J. Phys. Chem. A*, vol. 119, no. 31, pp. 8503–8511, 2015.

[18] A. I. Lozano, L. S. Maioli, B. Pamplona, J. Romero, M. Mendes, F. Ferreira da Silva, F. Kossoski, M. Probst, D. Süβ, M. H. F. Bettega, G. García, and P. Limão-Vieira, "Selective bond breaking of halothane induced by electron transfer in potassium collisions," *Phys. Chem. Chem. Phys.*, vol. 22, pp. 23837–23846, 2020.

[19] E. Marotta, E. Bosa, G. Scorrano, and C. Paradisi, "Positive and negative ion chemistry of the anesthetic halothane (1-bromo-1-chloro-2,2,2-trifluoroethane) in air plasma at atmospheric pressure.," *Rapid Commun. Mass Spectrom.*, vol. 19, no. 3, p. 391–396, 2005.

[20] D. Scharf and K. Laasonen, "Structure, effective pair potential and properties of halothane," *Chem. Phys. Lett.*, vol. 258, no. 1, pp. 276–282, 1996.

[21] P. Tang, I. Zubryzcki, and Y. Xu, "Ab initio calculation of structures and properties of halogenated general anesthetics: halothane and sevoflurane," *J. Comput. Chem.*, vol. 22, no. 4, pp. 436–444, 2001.

[22] B. Czarnik-Matusewicz, D. Michalska, C. Sandorfy, and T. Zeegers-Huyskens, "Experimental and theoretical study of the vibrational spectra of halothane," *Chem. Phys.*, vol. 322, no. 3, pp. 331–342, 2006.

[23] A. Yokoyama, K. Yokoyama, and T. Takayanagi, "Photodissociation dynamics of 1-bromo-1-chloro-2,2,2-trifluoroethane at 157 nm," *J. Phys. Chem. A*, vol. 101, no. 36, pp. 6647–6652, 1997.

[24] A. Saha, M. N. Kawade, H. P. Upadhyaya, A. Kumar, and P. D. Naik, "Photoexcitation of 2-bromo-2-chloro-1,1,1-trifluoroethane (halothane) to repulsive surface nσ^*(C–Br) at 234 nm: Dynamics of C–Br and C–Cl bond rupture," *Chem. Phys.*, vol. 416, pp. 1–10, 2013.

[25] L. S. Maioli, M. H. F. Bettega, F. Blanco, G. García, E. Lange, P. Limão-Vieira, and F. Ferreira da Silva, "Theoretical and experimental cross sections for electron scattering from halothane.," *A Eur. Phys. J. D*, vol. 73, no. 181, 2019.

[26] A. Hermann, H.-G. Mack, and H. Oberhammer, "Conformations and structures of desflurane and isoflurane," *J. Fluor. Chem.*, vol. 101, no. 2, pp. 223–231, 2000.

[27] C. Matias, A. Mauracher, S. Huber, S. Denifl, P. Limão-Vieira, P. Scheier, T. Märk, R. González-Méndez, and C. Mayhew, "Dissociative electron attachment to the volatile anaesthetics enflurane and isoflurane and the chlorinated ethanes pentachloroethane and hexachloroethane," *Int. J. Mass Spectrom.*, vol. 379, pp. 179–186, 2015.

[28] R. González-Méndez, P. Watts, D. C. Howse, I. Procino, H. McIntyre, and C. A. Mayhew, "Ion mobility studies on the negative ion-molecule chemistry of isoflurane and enflurane," *J. Am. Soc. Mass Spectrom.*, vol. 28, no. 5, pp. 939–946, 2017. PMID: 28224395.

[29] E. Lange, F. Ferreira da Silva, N. Jones, S. Hoffmann, D. Duflot, and P. Limão-Vieira, "The lowest-lying electronic states of isoflurane and sevoflurane in the 5.0–10.8 ev energy range investigated by experimental and theoretical methods," *Chem. Phys. Lett.*, vol. 716, pp. 42–48, 2019.

[30] J. Kopyra, B. P. Marinković, and J. B. Maljković, "Investigation of the anaesthetic isoflurane fragmentation induced by electron impact," *Eur. Phys. J. D.*, vol. 79, no. 97, 2025. Published: 08 August 2025.

[31] E. Lange, *Characterization of Electronic States of Volatile Anaesthetics by Electron Energy Loss Spectroscopy and Synchrotron Radiation.* Doctoral dissertation, Faculty of Sciences and Technology, NOVA University Lisbon, 2019.

[32] A. Lozano, F. F. da Silva, F. Blanco, P. Limão-Vieira, and G. García, "Total electron scattering cross section from sevoflurane by 1–300 ev energy electron impact," *Chemical Physics Letters*, vol. 706, pp. 533–537, 2018.

[33] A. Lesarri, E. J. Cocinero, J. C. López, and J. L. Alonso, "The conformational landscape of the volatile anesthetic sevoflurane," *Phys. Chem. Chem. Phys.*, vol. 12, no. 46, pp. 15483–15488, 2010.

[34] S. Kaur, A. K. Arora, K. L. Baluja, and A. Bharadvaja, "Electron scattering from sevoflurane," *Atoms*, vol. 13, no. 4, 2025.

[35] J. J. J. Dom, B. J. van der Veken, B. Michielsen, S. Jacobs, Z. Xue, S. Hesse, H.-M. Loritz, M. A. Suhm, and W. A. Herrebout, "On the weakly c–h hydrogen bonded complexes of sevoflurane and benzene," *Phys. Chem. Chem. Phys.*, vol. 13, pp. 14142–14152, 2011.

[36] D. Sutradhar, T. Zeegers-Huyskens, and A. K. Chandra, "A theoretical investigation on the conformation and the interaction of $CHF_2OCF_2CHF_2$ (desflurane ii) with one water molecule," *J. Mol. Model.*, vol. 19, no. 11, pp. 5045–5052, 2013.

[37] W. Zierkiewicz, "Reaction of volatile anaesthetic desflurane with chlorine atom. theoretical investigation," *Chem. Phys. Lett.*, vol. 555, pp. 72–78, 2013.

[38] S. Melikova, K. Rutkowski, B. Czarnik-Matusewicz, and M. Rospenk, "Vibrational spectra and conformational analysis of desflurane. a cryosolution and ab initio study," *Chem. Phys. Lett.*, vol. 637, pp. 77–82, 2015.

[39] P. L. Polavarapu, C. Zhao, A. L. Cholli, and G. G. Vernice, "Vibrational circular dichroism, absolute configuration, and predominant conformations of volatile anesthetics: desflurane," *The Journal of Physical Chemistry B*, vol. 103, no. 29, pp. 6127–6132, 1999.

[40] M. Allan, "Electron scattering from molecules: Experiment and theory," *J. Electron Spectrosc. Relat. Phenom.*, vol. 48, pp. 219–351, 1989.

[41] S. P. Khare, *Introduction to the Theory of Collisions of Electrons with Atoms and Molecules.* New York: Springer Science+Business Media New York, 2001.

[42] R. Brusa, M. Brunger, S. J. Buckman, M. Elfrod, G. G. Karwasz, and A. Zecca, *Electron Collisions with Molecules: Scattering and Excitation.* Berlin: Springer, 2017.

[43] B. H. Bransden and C. J. Joachain, *Physics of Atoms and Molecules*. Harlow, UK: Prentice Hall / Pearson Education, 2nd ed., 2003.

[44] C. J. Joachain, *Quantum Collision Theory*. Amsterdam, Netherlands: North-Holland Publishing Company, 1975.

[45] N. F. Lane, "The theory of electron-molecule collisions," *Rev. Mod. Phys.*, vol. 52, pp. 29–119, Jan 1980.

[46] M. A. Morrison, "Near-threshold electron-molecule scattering," vol. 24 of *Adv. At., Mol., Opt. Phys.*, pp. 51–156, Academic Press, 1988.

[47] S. Trajmar, D. Register, and A. Chutjian, "Electron scattering by molecules ii. experimental methods and data," *Phys. Rep.*, vol. 97, no. 5, pp. 219–356, 1983.

[48] D. Rapp and P. Englander-Golden, "Total cross sections for ionization and attachment in gases by electron impact. i. positive ionization," *J. Chem. Phys.*, vol. 43, no. 5, pp. 1464–1479, 1965.

[49] Y.-K. Kim and M. E. Rudd, "Binary-encounter-dipole model for electron-impact ionization," *Phys. Rev. A*, vol. 50, pp. 3954–3967, Nov 1994.

[50] G. J. Schulz, "Resonances in electron impact on atoms," *Rev. Mod. Phys.*, vol. 45, pp. 378–422, Jul 1973.

[51] L. G. Christophorou, *Electron-Molecule Interactions and Their Applications*. New York: Academic Press, 1984.

[52] B. H. Bransden, *Atomic Collision Theory*. Lecture Notes and Supplements in Physics, Reading, Massachusetts: Benjamin–Cummings Publishing Company, 2nd ed., 1983.

[53] M. Kurepa, *Interakcije niskoenergijskih elektrona*. Elektron - sto godina od otkrića No. sv. 4, Beograd: SANU, Zavod za udžbenike i nastavna sredstva, 1997.

[54] E. Feenberg, "The scattering of slow electrons by neutral atoms," *Physical Review*, vol. 40, p. 40, 1932.

[55] Y. Jiang, J. Sun, and L. Wan, "Total cross sections for electron scattering by polyatomic molecules at 10–1000 ev," *Phys. Rev. A*, vol. 52, pp. 398–403, 1995.

[56] Y. Jiang, J. Sun, and L. Wan, "Simple model for the calculation of total cross sections for electron scattering from polyatomic molecules," *J. Phys. B: At. Mol. Opt. Phys.*, vol. 30, no. 21, p. 5025, 1997.

[57] S. P. Khare, D. Raj, and P. Sinha, "Absorption effects in the elastic scattering of electrons by the CF_4 molecule at intermediate energies," *J. Phys. B: At. Mol. Opt. Phys.*, vol. 27, no. 12, p. 2569, 1994.

[58] D. Raj, "A note on the use of the additivity rule for electron-molecule elastic scattering," *Phys. Lett. A*, vol. 160, no. 6, pp. 571–574, 1991.

[59] F. Blanco and G. García, "Screening corrections for calculation of electron scattering differential cross sections from polyatomic molecules," *Phys. Lett. A*, vol. 330, no. 3, pp. 230–237, 2004.

[60] F. Blanco and G. García, "Screening corrections for calculation of electron scattering from polyatomic molecules," *Phys. Lett. A*, vol. 317, no. 5, pp. 458–462, 2003.

[61] F. Blanco, J. Rosado, A. Illana, and G. García, "Comparison of two screening corrections to the additivity rule for the calculation of electron scattering from polyatomic molecules," *Phys. Lett. A*, vol. 374, no. 43, pp. 4420–4424, 2010.

[62] F. Blanco and G. García, "Interference effects in the electron and positron scattering from molecules at intermediate and high energies," *Chem. Phys. Lett.*, vol. 635, pp. 321–327, 2015.

[63] F. Blanco, L. Ellis-Gibbings, and G. García, "Screening corrections for the interference contributions to the electron and positron scattering cross sections from polyatomic molecules," *Chem. Phys. Lett.*, vol. 645, pp. 71–75, 2016.

[64] R. D. Cowan, *The Theory of Atomic Structure and Spectra.* CA, USA: University of California Press: Berkeley, 1981.

[65] M. E. Riley and D. G. Truhlar, "Approximations for the exchange potential in electron scattering," *J. Chem. Phys.*, vol. 63, no. 5, pp. 2182–2191, 1975.

[66] X. Zhang, J. Sun, and Y. Liu, "A new approach to the correlation polarization potential-low-energy electron elastic scattering by he atoms," *J. Phys. B: Atom. Mol. Phys.*, vol. 25, p. 1893, apr 1992.

[67] N. Mott and H. Massey, *The Theory of Atomic Collisions. Nucl. Phys.* Oxford University Press, 1966.

[68] Y. Jiang, J. Sun, and L. Wan, "Electron scattering by SF_4 molecules at intermediate energies," *Phys. Lett. A*, vol. 231, no. 3, pp. 231–234, 1997.

[69] F. Blanco, A. Muñoz, D. Almeida, F. Ferreira da Silva, P. Limão-Vieira, M. C. Fuss, A. G. Sanz, and G. García, "Modelling low energy electron and positron tracks in biologically relevant materials," *Eur. Phys. J. D*, vol. 67, no. 199, pp. 1–10, 2013.

[70] J. B. Maljković, F. Blanco, G. García, B. P. Marinković, and A. R. Milosavljević, "Absolute cross sections for elastic electron scattering from methylformamide," *Phys. Rev. A*, vol. 85, p. 042723, 2012.

[71] A. Zecca, L. Chiari, G. García, F. Blanco, E. Trainotti, and M. J. Brunger, "Total cross sections for positron and electron scattering from pyrimidine," *J. Phys. B: Atom. Mol. Phys.*, vol. 43, no. 21, p. 215204, 2010.

[72] A. Zecca, R. Melissa, R. S. Brusa, and G. P. Karwasz, "Additivity rule for electron-molecule cross section calculation: A geometrical approach," *Phys. Lett. A*, vol. 257, no. 1, pp. 75–82, 1999.

[73] S. Hayashi and K. Kuchitsu, "Elastic scattering of electrons by molecules at intermediate energies. calculation of double scattering effects in n2 and p4," *Chem. Phys. Lett.*, vol. 41, no. 3, pp. 575–579, 1976.

[74] D. Raj and S. Tomar, "Electron scattering by triatomics: SO_2, CS_2 and ocs at intermediate energies," *J. Phys. B: Atom. Mol. Phys.*, vol. 30, no. 8, p. 1989, 1997.

[75] A. G. Sanz, M. C. Fuss, F. Blanco, F. Sebastianelli, F. A. Gianturco, and G. García, "Electron scattering cross sections from HCN over a broad energy range (0.1–10 000 ev): Influence of the permanent dipole moment on the scattering process," *J. Chem. Phys.*, vol. 137, no. 12, p. 124103, 2012.

[76] P. Możejko and L. Sanche, "Cross section calculations for electron scattering from dna and rna bases," *Radiat. Environ. Biophys.*, vol. 42, no. 3, pp. 201–211, 2003.

[77] P. Możejko and L. Sanche, "Cross sections for electron scattering from selected components of DNK and RNK," *Radiat. Phys. Chem.*, vol. 73, no. 2, pp. 77–84, 2005.

[78] R. Raizada and K. L. Baluja, "Total cross sections of positron scattering from various molecules using the rule of additivity," *Phys. Rev. A*, vol. 55, pp. 1533–1536, 1997.

[79] K. Joshipura and P. Patel, "Total electron scattering cross sections for NO, CO, NO_2, N_2O, CO_2 and NH_2 ($E_i = 50\,eV$)," *J.Phys.B : Atom.Mol.Phys., vol.* 29, *no.* 17, 1996.

[80] Y. Jiang, J. Sun, and L. Wan, "Additivity rule for the calculation of electron scattering from polyatomic molecules," *Phys. Rev. A*, vol. 62, p. 062712, 2000.

[81] F. Blanco and G. García, "Improvements on the quasifree absorption model for electron scattering," *Phys. Rev. A*, vol. 67, p. 022701, 2003.

[82] A. Jain, "Theoretical study of the total (elastic+inelastic) cross sections for electron -H_2O (NH_3) scattering at 10-3000 eV," *J. Phys. B: Atom. Mol. Phys.*, vol. 21, no. 5, p. 905, 1988.

[83] A. S. Dickinson, "Differential cross sections for electron scattering by strongly polar molecules," *J. Phys. B: Atom. Mol. Phys.*, vol. 10, no. 5, p. 967, 1977.

[84] A. Kuppermann, J. K. Rice, and S. Trajmar, "Low-energy, high-angle electron-impact spectrometry," *J. Phys. Chem.*, vol. 72, no. 11, pp. 3894–3903, 1968.

[85] G. C. King, J. W. McConkey, and F. H. Read, "Negative-ion resonances associated with inner-shell-excited states of N_2 and CO," *J. Phys. B: Atom. Mol. Phys.*, vol. 10, no. 14, p. L541, 1977.

[86] D. Vichon, F. Gresteau, A. Huetz, and J. Mazeau, "Resonant excitation of a new valence state in N_2 by electron impact," *J. Molec. Spect.*, vol. 73, no. 3, pp. 405–414, 1978.

[87] L. Vuskovic, S. K. Srivastava, and S. Trajmar, "Electron scattering by highly polar molecules. II. LiF," *J. Phys. B: Atom. Mol. Phys.*, vol. 11, no. 9, p. 1643, 1978.

[88] D. G. Wilden, P. J. Hicks, and J. Comer, "High resolution studies of dipole-forbidden states of N_2 using low-energy electron energy-loss spectroscopy," *J. Phys. B: Atom. Mol. Phys.*, vol. 12, no. 9, p. 1579, 1979.

[89] D. Spence, "Studies of the O_2 $^3\Pi_g$(V) valence states and $^3\Pi_g$(R) Rydberg state in the schumann–runge continuum from ejected and scattered electron spectra," *J. Chem. Phys.*, vol. 74, no. 7, pp. 3898–3904, 1981.

[90] J. P. Doering and R. McDiarmid, "Electron impact study of the energy levels of trans-1,3-butadiene: II. Detailed analysis of valence and Rydberg transitions," *J. Chem. Phys.*, vol. 73, no. 8, pp. 3617–3624, 1980.

[91] C. B. Lucas, *Atomic and Molecular Beams: Production and Collimation*. Boca Raton, FL: CRC Press, 2013.

[92] A. R. Milosavljević, "Kritičke tačke u elastičnom rasejanju elektrona na atomu argona," Magistarski rad, Univerzitet u Beogradu, Beograd, 2004.

[93] J. F. Williams and B. A. Willis, "The scattering of electrons from inert gases. i. absolute differential elastic cross sections for argon atoms," *J. Phys. B: Atom. Mol. Phys.*, vol. 8, no. 10, p. 1670, 1975.

[94] A. Milosavljević, S. Telega, D. Šević, J. Sienkiewicz, and B. Marinković, "Elastic electron scattering by argon in the vicinity of the high-energy critical minimum," *Radiat. Phys. Chem.*, vol. 70, no. 6, pp. 669–676, 2004.

[95] R. Panajotovic, D. Filipovic, B. Marinkovic, V. Pejcev, M. Kurepa, and L. Vuskovic, "Critical minima in elastic electron scattering by argon," *J. Phys. B: Atom. Mol. Phys.*, vol. 30, p. 5877, dec 1997.

[96] M. L. Ranković, J. B. Maljković, K. Tökési, and B. P. Marinković, "Elastic electron differential cross sections for argon atom in the intermediate energy range from 40 ev to 300 ev," *Eur. Phys. J. D*, vol. 72, no. 30, pp. 1–12, 2018.

[97] A. R. Milosavljević, *Interakcija elektrona sa molekulima analognim deoksiribozi u DNK lancu*. Phd thesis, University of Belgrade, Faculty of Physics, Belgrade, Institute of Physics, 2006.

[98] S. Madžunkov, "Disocijativna jonizacija," magistarski rad, University of Belgrade, Faculty of Physics, Belgrade, Institute of Physics, 1998.

[99] J. B. Maljković, *Absolute Cross Sections for Electron Scattering from Organic Molecules Relevant to the Structure of Biological Macromolecules*. Phd thesis, University of Belgrade, Faculty of Physics, Belgrade, 2013.

[100] S. K. Srivastava, A. Chutjian, and S. Trajmar, "Absolute elastic differential electron scattering cross sections in the intermediate energy region. i. h2 ," *J. Chem. Phys.*, vol. 63, no. 6, pp. 2659–2665, 1975.

[101] J. C. Nickel, C. Mott, I. Kanik, and D. C. McCollum, "Absolute elastic differential electron scattering cross sections for carbon monoxide and molecular nitrogen in the intermediate energy region," *J. Phys. B*, vol. 21, no. 10, p. 1867, 1988.

[102] J. C. Nickel, P. W. Zetner, G. Shen, and S. Trajmar, "Principles and procedures for determining absolute differential electron-molecule (atom) scattering cross sections," *J. Phys. E*, vol. 22, no. 9, p. 730, 1989.

[103] M. A. Khakoo and S. Trajmar, "Elastic electron scattering cross sections for molecular hydrogen," *Phys. Rev. A*, vol. 34, pp. 138–145, 1986.

[104] R. T. Brinkmann and S. Trajmar, "Effective path length corrections in beam-beam scattering experiments," *J. Phys. E: Sci. Instr.*, vol. 14, no. 2, p. 245, 1981.

[105] D. R. Olander and V. Kruger, "Molecular beam sources fabricated from multichannel arrays. III. The exit density problem," *J. Appl. Phys.*, vol. 41, no. 7, p. 2769, 1970.

[106] M. G. P. Homem, I. Iga, R. T. Sugohara, I. P. Sanches, and M. T. Lee, "Role of adsorption effects on absolute electron-molecule cross-section calibration using the relative flow technique," *Rev. Sci. Instrum.*, vol. 82, no. 1, p. 013109, 2011.

[107] J. B. Maljković, J. Vukalović, Z. D. Pešić, F. Blanco, G. García, and B. P. Marinković, "Experimental and theoretical study on elastic electron interaction with halothane molecule in the intermediate energy range," *Eur. Phys. J. Plus*, vol. 138, p. 349, 2023.

[108] NOAA Office of Response and Restoration, "Halothane." CAMEO Chemicals, National Oceanic and Atmospheric Administration, 1992. Accessed: 2025-09-18.

[109] D. H. Robinson and A. H. Toledo, "Historical development of modern anesthesia.," *J. Invest. Surg.*, vol. 25, no. 3, pp. 141–9, 2012.

[110] D. F. Lewis, M. G. Bird, and D. V. Parke, "Molecular modelling of CYP2E1 enzymes from rat, mouse and man: an explanation for species differences in butadiene metabolism and potential carcinogenicity, and rationalization of CYP2E substrate specificity.," *Toxicology*, vol. 118, no. 2-3, p. 93–113, 1997.

[111] D. H. Robinson and A. H. Toledo, "Historical development of modern anesthesia.," *J. Invest. Surg.*, vol. 25, no. 3, pp. 141–9, 2012.

[112] "Pubchem database [online]," Accessed on 20. July 2023. Available: `https://pubchem.ncbi.nlm.nih.gov/`.

[113] M. J. Arcario, C. G. Mayne, and E. Tajkhorshid, "Atomistic models of general anesthetics for use in in silico biological studies," *The Journal of Physical Chemistry B*, vol. 118, no. 42, pp. 12075–12086, 2014. PMID: 25303275.

[114] J. B. Maljković, J. Vuković, K. Tökési, B. Predojević, and B. P. Marinković, "Elastic electron scattering cross sections for triethyl phosphate molecule at intermediate electron energies from 50 eV to 250 eV," *Eur. Phys. J. D*, vol. 73, p. 27, 2019.

[115] J. Vukalović, J. B. Maljković, K. Tökési, B. Predojević, and B. P. Marinković, "Elastic electron scattering from methane molecule in the energy range from 50–300 eV," *Int. J. Mol. Sci.*, vol. 22, no. 2, 2021.

[116] M. E. Hosain, M. A. R. Patoary, M. M. Haque, A. K. F. Haque, M. I. Hossain, M. A. Uddin, A. K. Basak, M. Maaza, and B. C. Saha, "Elastic scattering of e by na atoms," *Mol. Phys.*, vol. 116, no. 5-6, pp. 631–648, 2018.

[117] Y.-F. Wang and S. X. Tian, "Low-energy electron collisions with formamide using the r-matrix method," *Phys. Rev. A*, vol. 85, p. 012706, Jan 2012.

[118] Y. Itikawa, "Momentum-transfer cross sections for electron collisions with atoms and molecules," *At. Data Nucl. Data Tables*, vol. 14, no. 1, pp. 1–10, 1974.

[119] M. Gaya da Costa, A. F. Kalmar, and M. M. R. F. Struys, "Inhaled anesthetics: Environmental role, occupational risk, and clinical use," *J. Clin. Med.*, vol. 10, no. 6, 2021.

[120] H. Tanaka, M. J. Brunger, L. Campbell, H. Kato, M. Hoshino, and A. R. P. Rau, "Scaled plane-wave born cross sections for atoms and molecules," *Rev. Mod. Phys.*, vol. 88, p. 025004, May 2016.

[121] "Desflurane (pubchem compound CID 42113)." https://pubchem.ncbi.nlm.nih.gov/compound/42113. National Center for Biotechnology Information. PubChem Database. Retrieved December 22, 2025.

[122] M. J. Arcario, C. G. Mayne, and E. Tajkhorshid, "Atomistic models of general anesthetics for use in in silico biological studies," *J. Phys. Chem. B*, vol. 118, no. 42, pp. 12075–12086, 2014.

[123] L. Minkovich and W. C. K. Ng, *Metabolism and Toxicity of Inhalational General Anesthetics (IGA)*, pp. 1–19. John Wiley Sons, Ltd, 2017.

Author Biography

Jelena Vukalović was born on May 21, 1991, in Sarajevo, Bosnia and Herzegovina. She completed her undergraduate studies in Physics in 2015 at the Faculty of Natural Sciences and Mathematics, University of Banja Luka, with an average grade of 9.56. She completed her master's academic studies in 2018 at the Faculty of Physics, University of Belgrade, defending her master's thesis entitled "Absolute Differential Cross Sections for Elastic Electron Scattering from Triethyl Phosphate Molecule", with an average grade of 9.67.

She is currently pursuing doctoral studies at the Faculty of Physics, University of Belgrade, in the field of Atomic and Molecular Physics under the supervision of Dr. Jelena Maljković. Her doctoral research is focused on elastic electron scattering from molecules, particularly anesthetic molecules.

Since October 2016, she has been employed at the Faculty of Natural Sciences and Mathematics, University of Banja Luka. She worked as a teaching assistant until March 2020, when she was elected to the position of senior teaching assistant. She has participated in teaching several courses, including Measurement Data Processing, Measurement Methods, Fundamentals of Matter Structure, Fundamentals of Atomic Physics, Atomic and Molecular Physics, Mechanics, Quantum Field Theory, Optics, Experimental Physics Laboratory 2, Laser Physics, and Physics for Biology students.

Her scientific research is focused on elastic electron scattering from molecules, especially anesthetic molecules. This dissertation is a result of her original scientific research.

Selected Publications

1. J. B. Maljković, J. Vuković, K. Tökési, B. Predojević, B. P. Marinković, "Elastic electron scattering cross sections for triethyl phosphate molecule at intermediate electron energies from 50 eV to 250 eV", *The European Physical Journal D*, 73(27), 2019.

2. J. Vukalović, J. B. Maljković, K. Tökési, B. Predojević, B. P. Marinković, "Elastic electron scattering from methane molecule in the energy range from 50–300 eV", *International Journal of Molecular Sciences*, 22(2), 2021.

3. J. Vukalović, J. B. Maljković, F. Blanco, G. García, B. Predojević, B. P. Marinković, "Absolute differential cross-sections for elastic electron scattering from sevoflurane molecule in the energy range from 50–300 eV", *International Journal of Molecular Sciences*, 23(1), 2021.

4. J. B. Maljković, J. Vukalović, Z. D. Pešić, F. Blanco, G. García, B. P. Marinković, "Experimental and theoretical study on elastic electron interaction with halothane molecule in the intermediate energy range", *The European Physical Journal Plus*, 138(4), 2023.

5. J. Vukalović, B. P. Marinković, J. Rosado, F. Blanco, G. Garcia, J. B. Maljković, "Investigating theoretical and experimental cross sections for elastic electron scattering from isoflurane", *Physical Chemistry Chemical Physics*, 26(985), 2023.

Изјава о ауторству

Име и презиме аутора: Јелена Вукаловић

Број индекса: 2018/8028

Изјављујем

да је докторска дисертација под насловом

Elastic Electron Scattering from Anesthetic Molecules — Sevoflurane, Isoflurane, Desflurane and Halothane — in the Intermediate Energy Range
(Еластично расејање електрона средњих енергија на молекулима анестетика — севофлурану, изофлурану, десфлурану и халотану)

- резултат сопственог истраживачког рада;
- да дисертација у целини ни у деловима није била предложена за стицање друге дипломе према студијским програмима других високошколских установа;
- да су резултати коректно наведени; и
- да нисам кршио/ла ауторска права и користио/ла интелектуалну својину других лица.

У Београду, _____

_____
Потпис аутора

Изјава о истоветности штампане и електронске верзије докторског рада

Име и презиме аутора: Јелена Вукаловић

Број индекса: 2018/8028

Студијски програм: Физика атома и молекула

Наслов рада: Elastic Electron Scattering from Anesthetic Molecules - Sevoflurane, Isoflurane, Desflurane and Halothane - in the Intermediate Energy Range
(Еластично расејање електрона средњих енергија на молекулима анестетика - севофлурану, изофлурану, десфлурану и халотану)

Ментор: др Јелена Маљковић

Изјављујем да је штампана верзија мог докторског рада истоветна електронској верзији коју сам предао/ла ради похрањивања у **Дигиталном репозиторијуму Универзитета у Београду**.

Дозвољавам да се објаве моји лични подаци везани за добијање академског назива доктора наука, као што су име и презиме, година и место рођења и датум одбране рада.

Ови лични подаци могу се објавити на мрежним страницама дигиталне библиотеке, у електронском каталогу и у публикацијама Универзитета у Београду.

У Београду, _____

_____
Потпис аутора

Изјава о коришћењу

Овлашћујем Универзитетску библиотеку „Светозар Марковић“ да у Дигитални репозиторијум Универзитета у Београду унесе моју докторску дисертацију под насловом:

Elastic Electron Scattering from Anesthetic Molecules - Sevoflurane, Isoflurane, Desflurane and Halothane - in the Intermediate Energy Range

(Еластично расејање електрона средњих енергија на молекулима анестетика - севофлурану, изофлурану, десфлурану и халотану)

која је моје ауторско дело.

Дисертацију са свим прилозима предао/ла сам у електронском формату погодном за трајно архивирање.

Моју докторску дисертацију похрањену у Дигиталном репозиторијуму Универзитета у Београду и доступну у отвореном приступу могу да користе сви који поштују одредбе садржане у одабраном типу лиценце Креативне заједнице (Creative Commons) за коју сам се одлучио/ла.

1. Ауторство (CC BY)
2. Ауторство -- некомерцијално (CC BY-NC)
3. Ауторство -- некомерцијално -- без прерада (CC BY-NC-ND)
4. Ауторство -- некомерцијално -- делити под истим условима (CC BY-NC-SA)
5. Ауторство -- без прерада (CC BY-ND)
6. Ауторство -- делити под истим условима (CC BY-SA)

(Молимо да заокружите само једну од шест понуђених лиценци. Кратак опис лиценци је саставни део ове изјаве.)

У Београду, _____

_____

Потпис аутора

1. **Ауторство**
   Дозвољавате умножавање, дистрибуцију и јавно саопштавање дела, и прераде, ако се наведе име аутора на начин одређен од стране аутора или даваоца лиценце, чак и у комерцијалне сврхе. Ово је најслободнија од свих лиценци.

2. **Ауторство - некомерцијално**
   Дозвољавате умножавање, дистрибуцију и јавно саопштавање дела, и прераде, ако се наведе име аутора на начин одређен од стране аутора или даваоца лиценце. Ова лиценца не дозвољава комерцијалну употребу дела.

3. **Ауторство - некомерцијално - без прерада**
   Дозвољавате умножавање, дистрибуцију и јавно саопштавање дела, без промена, преобликовања или употребе дела у свом делу, ако се наведе име аутора на начин одређен од стране аутора или даваоца лиценце. Ова лиценца не дозвољава комерцијалну употребу дела. У односу на све остале лиценце, овом лиценцом се ограничава највећи обим права коришћења дела.

4. **Ауторство - некомерцијално - делити под истим условима**
   Дозвољавате умножавање, дистрибуцију и јавно саопштавање дела, и прераде, ако се наведе име аутора на начин одређен од стране аутора или даваоца лиценце и ако се прерада дистрибуира под истом или сличном лиценцом. Ова лиценца не дозвољава комерцијалну употребу дела и прерада.

5. **Ауторство - без прерада**
   Дозвољавате умножавање, дистрибуцију и јавно саопштавање дела, без промена, преобликовања или употребе дела у свом делу, ако се наведе име аутора на начин одређен од стране аутора или даваоца лиценце. Ова лиценца дозвољава комерцијалну употребу дела.

6. **Ауторство - делити под истим условима**
   Дозвољавате умножавање, дистрибуцију и јавно саопштавање дела, и прераде, ако се наведе име аутора на начин одређен од стране аутора или даваоца лиценце и ако се прерада дистрибуира под истом или сличном лиценцом. Ова лиценца дозвољава комерцијалну употребу дела и прерада. Слична је софтверским лиценцама, односно лиценцама отвореног кода.